UNIVERSITY OF BIRMINGHAM

Development of a Remote Optically Actuated and Interrogated Passive Sensor with Micro Corner Cube Reflector Structure

By

Tianshi Luan

A thesis submitted to

The University of Birmingham

for the degree of

Doctor of Philosophy

School of Mechanical Engineering

University of Birmingham

September 2016

Abstract

There is an increasing demand for sensors in extreme environments, i.e. high temperature and radiation environments, where conventional sensors lose their functionality and reliability because of the environmental impact. The dependence on electricity makes conventional sensor susceptible to extreme accident situation and demanding frequent maintenance which could be even more costly in those extreme environments.

To overcome this problem, this thesis reports the development of a remote optically actuated and interrogated resonant sensor with a micro corner cube retroreflector (CCR) structure. The proposed sensor takes the advantage of MEMS scaling to enable optical actuation and can be remotely interrogated. It does not rely on any local electrical power or electric elements therefore it is more resistant to high temperature and radiation impact. Also, a micro corner cube structure is employed to enhance the working distance and simplify the detection system. A perspective application scenario is the temperature monitoring in nuclear waste repository.

In this thesis, a micro paddle resonant sensor is theoretically shown to be able to get actuated without using electrical power or electric element. The remote actuation with optical method was analytically modelled and simulated. It is shown to be capable to produce a tilting angle up to 1.5 mrad in the paddle

resonant structure which is large enough for remote optical detection. A simple and impact optical interrogation system is designed by combining the micro paddle resonator with a micro CCR structure which allows interrogating light source and detecting photodiode to be placed in the same place utilising the retroreflection of the CCR. Finally, the fabrication methods of the paddle mirror and micro CCR sidewalls were developed and demonstrated respectively. The fabrication results have shown reasonable mechanical resonance behaviour and surface smoothness. Although the fabrication of a completed sensor is not achieved in this thesis due to the limitation of accessible facilities in the given time, a completed fabrication plan is provided.

This thesis is dedicated to my parents

for their unconditional love and endless support

Acknowledgements

I would like to thank my supervisor Dr. Carl Anthony, who patiently supported me with utmost guidance and continuous encouragement in the duration of my PhD research.

I would like to thank Aydin Sabouri, Adam Sheward and Becky Charles for their assistance in the lab work. I would also like to thank all my colleagues, especially Siyang Cao, Cun Li, Guanxiong Wang and Nasim Mahmoodi for their kind help and useful discussion in the progress of my research.

Last but not least, my special thanks go to Miss Sijia Tao for her constant companionship, encouragement and support in my life. It means a lot to me.

Contents

List of Abbreviations

AFM	Atomic Force Microscopy
CCR	Corner Cube Retroreflector
DRIE	Deep Reactive Ion Etching
F-P	Fabry-Perot
FDM	Finite Difference Method
FEM	Finite Element Method
HF	Hydrofluoric Acid
IPA	Isopropyl Alcohol
LDV	Laser Doppler Vibrometer
LIGA	Lithography, Electroplating, and Moulding
MEMS	Microelectromechanical Systems
PDMS	Polydimethylsiloxane
PEB	Post-exposure Bake
PSD	Position Sensitive Detector
Q	Quality Factor
RF	Radio Frequency
RMS	Root-Mean-Square
SAW	Surface Acoustic Wave
SEM	Scanning Electron Microscope
SOI	Silicon-on-Insulator
UV	Ultraviolet

List of Figures

List of Tables

Chapter 1: Introduction

1.1 The need of remote actuated and interrogated sensors

In harsh environments, i.e. high-temperature environment, radiation environment, battlefield, and other situations where humans do not have easy access to, there is a large demand for wireless sensors that can provide environmental and industrial status monitoring with low establishment and maintenance cost (Bogue 2012, Yang 2013, Hong et al. 2015). However, lots of conventional wireless sensors with electronic circuits are not suitable in these environments due to the intense environmental impact (Werner & Fahrner 2001, Wang et al. 2009). In most extreme scenarios, like the Fukushima Daiichi nuclear disaster that happened in 2011, being dependent on electricity can also lead to a sensor's failure. Therefore, a new type of sensor which can perform precise measurement in those extreme environments without the requirement of any local power supply and can be monitored remotely is needed to be developed.

In this thesis, a remote optically actuated and interrogated passive micro sensor system with the potential to operate in extreme environments is proposed as a solution. The sensor node can be excited by an optical stimulation from a distance away. Once installed, the sensor node can stay onsite for a long time without the need for any battery replacement. Also, the sensor can be interrogated remotely, which leaves the interrogation system in a relatively safe

environment as long as a line-of-sight is available in-between. The sensing process is deemed to be passive since the sensor itself does not require a localised power source to actively determine the measurand and the transmission of data back to the instrument is by use of a passive corner cube retro reflector transmitter rather than an active laser source (Kahn et al., 1999). Hence the sensor node requires extracting no power actively and only produces signal when it is interrogated.

The proposed system has many benefits such as being unnoticeable due to small size, resistant to electromagnetic interference and having highly secured signal transmission compared with other wireless sensors using radio frequency (RF). Also, it has a low power consumption rate as it only produces a signal when being actuated and interrogated intentionally.

1.2 Aim and Objectives

The aim of this project is to develop a new type of micro sensor which allows remotely optical actuation and interrogation. The objectives of this work are listed below.

i) First, a stress-sensitive sensor structure which allows remotely optical actuation needs to be designed. It includes analytical calculation and simulation verification in finite element analysis software.

ii) Second, the technique of optical interrogation from a relatively long distance needs to be investigated and adopted into the system.

iii) Third, a feasible method for the sensor fabrication needs to be developed. The fabrication process should be as simple and economic as possible.

1.3 Sensor system specifications and potential applications

The sensor system being developed in this work is proposed to have the specifications as follow. The sensor node will be free of any electric element, which prevents the sensor from having electric failure due to harsh environmental impacts. The sensing element should be able to get actuated remotely and produce a difference in the structure which is large enough to be detected over a distance, set to be 3m in the development stage. The interrogation system is aimed to be easily accessible and compact in size. The sensor structure will be built using normal materials for prototyping. Extremely high temperature and radiation resistant materials are not included in the development stage because of the difficulty in fabrication processes and the limitation of facilities accessible.

Parameters which can cause stress changing in the sensing element, such as temperature, tensile force and pressure, are aimed to be measured. In order to discriminate the effect of temperature during measuring other parameters, an unloaded sensor with the same structure can be positioned next to the actual sensor as a reference.

The developed sensor system will be capable to be adopted in some applications where electric circuit and frequent maintenance are not desired. An example application scenario for this system is nuclear waste monitoring. In the nuclear waste repository, reliable sensors are needed to monitor the status of nuclear waste but human participation is desired to be as little as possible. The temperature of the spent fuel is one of the most concerned parameters that need to be monitored in order to assure safe storage (Borgermans et al. 2007). By applying the proposed sensor system, it can obtain the benefit that no maintenance is required by the sensor, no human is needed to get close to the sensor after installation and the environmental impact affecting sensor performance will be minimised due to the absence of an electric circuit.

A potential limitation of this system is that the sensor can be affected by a dirty window when being applied in some dusty environments. When the package window of the sensor is covered with dust or dirt, the optical transmission will deteriorate. Power lost will largely increase so that the functionality of the sensor can be disabled. Therefore, this sensor system should be applied in a relatively clean area, otherwise the lifetime of the sensor nodes will be reduced. Self-cleaning surfaces are now being developed (Guan 2005, He et al. 2011) so in the future this limitation may be reduced through careful design and use of materials in the packaging.

1.4 Originalities

The main originalities of the thesis are listed as follows. First, the principle theory of the photothermal actuation of a tilting paddle resonator is proposed and developed. This is new to the literature and can be applied to similar tilting motion actuations. Second, a micro CCR is combined with the resonator sensor in the design for the first time. This allows optically interrogation over a relatively long operating distance. Third, several novel fabrication processes of micro CCR are proposed and tested to simplify the micro CCR fabrication without compromising its optical properties.

1.5 Outline of the thesis

The remainder of the thesis is organized as follows. In Chapter 2, a literature review will be given. It will firstly introduce the fundamental of microelectromechanical systems and the micro resonant sensor. Then extreme environments and the sensing techniques in the extreme environment will be reviewed, followed by introducing the micro corner cube retroreflector and its applications. Last but not the least, summaries on the literature review will be given and the knowledge gaps in the literature will be summarized.

Chapter 3 will present the design and analytical modelling of the optically actuated paddle resonator. The paddle design specification and material selection will be given. Then the analytical calculation and software simulation will be processed to model the performance of the actuated paddle. Design parameters will be optimized based on the modelling result.

In Chapter 4, an optical interrogation system will be designed. The principles of sensor interrogation with a corner cube retroreflector will be introduced. Then the design specifications and their effect on optical behaviours are going to be discussed. The design setup and parameters of the sensor system will be presented.

Chapter 5 will present the possible microfabrication process and their results of fabricating the sensor node. The paddle resonator will be fabricated using silicon microfabrication and nickel micro electroforming. The sidewalls of the micro corner cube will be fabricated via laser machining, silicon microfabrication, SU-8 photolithography and PDMS (Polydimethylsiloxane) moulding. The feasibilities and potential problems of these fabrication approaches will be analysed. In the end, a possible fabrication plan of the completed sensor node will be designed.

In Chapter 6, conclusions will be drawn from the research. Findings and achievements in each chapter will be summarized. Finally, the future work that can be carried out based on this study will be stated.

Chapter 2: Literature Review

2.1 Introduction

In this chapter, the background of MEMS is introduced and literature of current extreme environment sensing techniques is reviewed. Then the micro corner cube retroreflector structure used in MEMS is introduced, followed by a conclusion of the knowledge gaps in the literature and the originalities of this research.

2.2 Review on Micro Resonant Sensors

2.2.1 Basis of MEMS

MEMS, Microelectromechanical Systems, is a rapidly developing technology in the last few decades (Langdon 1985, Bao 2005). It can be found in a variety of applications including ink jet printer heads, air-bag trigger sensor in most of the vehicles and gyroscopes in today's mobile phones (Gad-el-Hak 2010). These microsystems benefit from downsizing devices into the sub-millimeter scale to achieve diverse functionality. First, MEMS is noninvasive to be added to existing structures and its power consumption is very low, due to its small size and mass. Second, microstructures can utilise physical phenomenon that is much more apparent on the microscale. For example, the Casimir force, a quantum electromagnetic field force interacting between macroscopic bodies (Klimchitskaya et al. 2009), is insignificant over macroscale separations. But it

can be used as a coupling force between micro resonators when they are designed to be kept within a microscopic distance (Carter et al. 2009). Also, small form factor improves MEMS's sensitivity since miniaturized sensing elements can recognise the tiny difference of physical variables. For example, the amplitude of a microcantilever vibration, generated by low power laser heating impulse, can respond to changes of atomic force (Labuda et al. 2014). Moreover, MEMS allows batch fabrication, which makes its production economical and effective (Madou 1997).

2.2.2 MEMS Fabrication

MEMS fabrication is mainly based on well-developed silicon technology (Petersen 1982). It creates structures on substrates, typically thin silicon wafers. Silicon wafers are commercially available with different thickness, doping and buried or coated layers. Some of the MEMS fabrication processes need to add layers onto a wafer, for example, growing an oxide layer (Zhou et al. 2003), PVD (physical vapour deposition) (Rahul Agarwal et al. 2007), CVD (chemical vapour deposition) (Kroetz et al. 1999), spin cast (Wei et al. 2008), wafer bonding (Miyahira et al. 2003) and electroplating (MacGeough et al. 2001). Some of the processes need to create designed patterns on the wafer using photolithography (Young-Min et al. 2010). And some of the processes need micromachining, which includes wet etch (Williams et al. 2003), dry etch (Jansen et al. 1995) and laser machining (Jolic et al. 2004).

2.2.3 Micro Resonant sensor

Microsensor can be classified by the principle of sensing, for instance, resistive sensing, capacitive sensing, piezoelectric sensing, thermoelectric sensing, magnetic sensing and resonant sensing (Elwenspoek & Wiegerink 2001), etc. In all these sensing principles, one or more physical quantities can be detected to be changing with the parameter that is being measured (Adams & Layton 2010).

A micro resonant sensor works with the principle that it relates some characteristic of a resonating system to an external parameter (measurand) affecting the system (Venkatesh 1988). It could be the phase angle between responses, the decay time of an impulse stimulation, quality factor or resonant frequencies that respond to the change of stress or effective mass caused by the measurands. One of the first micro resonant sensors was developed by Greenwood (Greenwood 1984), shown in Figure 2.2-1.

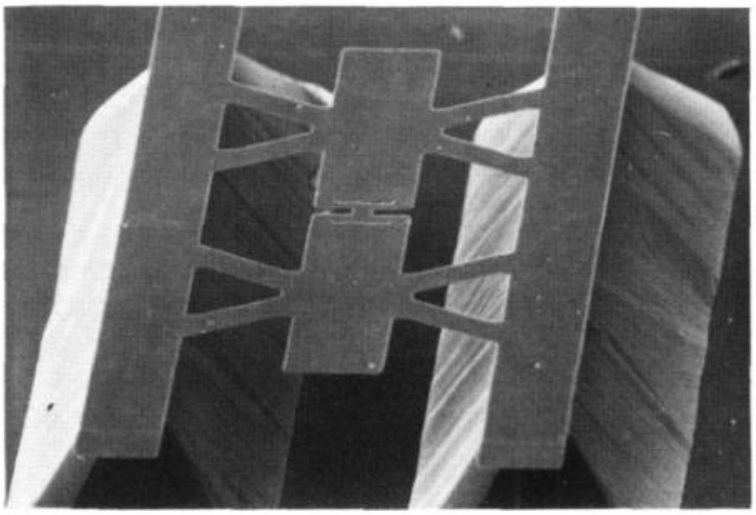

Figure 2.2-1 SEM view of the resonator developed by (Greenwood 1984)

For a spring-mass system driven by a periodic force $F=F_0 \sin(\omega t)$, the equation of motion is

$$m\ddot{x} + kx + c\dot{x} = F_0 \sin \omega t \qquad \textbf{(2.2-1)}$$

where m is the mass, k is the spring constant, c is the coefficient of damping. The oscillation amplitude B and phase lag φ are solved to be (Bao 2005)

$$B = \frac{{F_0}/{m}}{\sqrt{({\omega_0}^2 - \omega^2)^2 + 4n^2\omega^2}} \qquad \textbf{(2.2-2)}$$

$$\varphi = \tan^{-1} \frac{2n\omega}{{\omega_0}^2 - \omega^2} \qquad \textbf{(2.2-3)}$$

where n=c/2m, ω_0 is the natural frequency.

Resonance happens when a system is driven at its natural frequencies ($\omega_0 = \omega$), when the damping is light. Output amplitude is magnified and phase angle is π/2. Peaks will appear in the frequency response graph at these frequencies as shown in Figure 2.2-2.

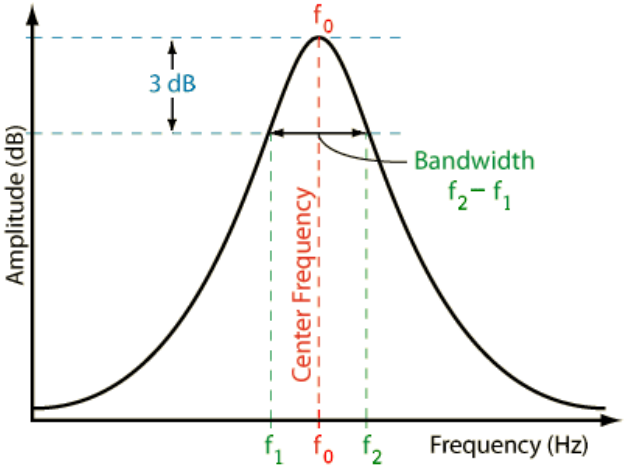

Figure 2.2-2 Frequency response graph

Quality factor Q is used to describe the quality of the resonance. It is defined as the number of the cycle that the resonant system can oscillate before its total energy gets dissipated; alternatively, it is the ratio of the stored energy to the energy dissipated per cycle; and can be determined from the resonance peak as the resonance frequency divide by the peak width at the 3 dB points, as shown in Figure 2.2-2. The greater the Q is, the sharper the resonant peak in the frequency response graph is, and hence the more accurate the readout could be. Air damping affects the quality factor as it results in higher energy loss, hence most of the resonators are operating in low pressure or vacuum to reduce this air damping in order to get larger Q value.

Micro resonant sensor can be actuated by different methods, such as capacitive actuation (Carter et al. 2009), piezoelectric actuation (Lee & Park 2010), thermoelectric actuation (Carstens et al. 2012), magnetic actuation (Vasquez & Judy 2007) and optical actuation (Hahtela & Tittonen 2005).

Micro resonant sensors have several advantages over other types of mechanical micro sensor (Elwenspoek & Wiegerink 2001): (1) Since resonant sensors have frequency output, the digital output can be directly sent to processing electronics without the need of analogue to digital conversion. (2) The frequency output can be transported over long distances with less loss of accuracy. Measuring the frequency rather than the amplitude of vibration makes resonant sensors less susceptible to the noise introduced from external sources. (3) When operating

with a high Q factor, the power consumption of resonant sensors can be very low because only the energy to maintain the vibration is required.

2.3 Extreme Environment Sensing

2.3.1 Extreme Environments

In many industries and applications, processes in extreme environments are involved. But sensing is crucial to monitoring and controlling these processes. Extreme environments, or harsh environments, for MEMS normally includes: (1) environments with very high temperature. Gas turbine and power generation need sensors operating at 600°C; the new generation nuclear power plant operates at a higher temperature - above 1000°C (Bogue 2012). (2) High radiation environments. Aerospace and nuclear industries have gamma exposure up to several 10^{10} rad and neutron flux up to several 10^{18}n/cm^2 (Bogue 2012). (3) Environments like a battlefield that needs latent sensors for situational awareness with minimum maintenance. Parameters of seismic, infrared, electric field, radiofrequency, magnetic and chemical-biological threats need to be monitored and transmitted to base station safely (Eicke 1999).

2.3.2 Conventional MEMS sensor in extreme environments

There are several reasons that conventional MEMS sensors are not suitable for extreme environments:

1. Rely on electricity. Most of the sensors are not durable for a long time or cannot function at all when the power supply is cut off. In the extreme situation such as Fukushima earthquake Japan 2011, the power supply might not be available for a period of time while the mission of monitoring is still crucially in need. This also means an expensive cable network needs to be established or frequent manual maintenance carried out, which could be even more costly in those extreme environments.

2. Sensor or signal is not secure. Conventional electrical sensors are liable to suffer electromagnetic interference. For example, on a battlefield, RF signal are more likely to be detected or disturbed.

3. Sensor performance susceptible to extreme environments. First, the mechanical properties of sensor structures can be affected. Young's modulus decrease for most of the materials in high temperature, for instance, silicon begins to deform plastically at around 600°C. Electric contacts get damaged in high temperature and radiation. Second, the electrical properties of the sensor element can be affected. Piezoelectric materials get depolarized when the temperature goes above its Curie temperature (Bogue 2012). In semiconductors, carriers are generated at high temperature and radiation affecting electrical conductivity. Radiation charges the dielectric which affects MEMS structure movement (Shea 2011). In some cases, neutron radiation can cause a cascade

of defects in the material lattice, or even react with certain nuclei, which lead to unwanted changes in both mechanical and electrical properties (Makowski 2006).

2.4 Existing Techniques for Extreme Environments Sensors

To be capable of operating in those extreme environments, a MEMS sensor with passive actuation and secure remote interrogation is required, along with the use of high temperature and radiation tolerant materials. Existing technologies for these aspects are reviewed as follow.

2.4.1 Passive actuation

Since the extreme environments limit the possibility of having batteries or active energy harvesting systems as power sources, using a passively actuated sensor is ideal as a passive sensor generally uses external energy sources to perform the measurement. Also, a passive sensor is more robust when operating in extreme environments since it can avoid having electric elements and eliminate the risk for them to be damaged. Several passive actuation techniques for extreme environments are reported in the literature.

2.4.1.1 Acoustic actuation

Acoustic wave can be used as a power source for sensor actuation. One of the methods is to directly vibrate the moving part by transferring the vibration from its surrounding air. Knobloch et al. proposed a resonant sensor with remote readout

but without local electronics (Knobloch et al. 2013). They demonstrate an acoustic drive application where an ultrasonic transducer is facing towards the sensor from a distance of about 20 cm away, actuating the resonator acoustically. Although the drive and readout are suitable for a handheld and portable design, the working distance is limited by its principle of operation and high acoustic power consumption.

Another method of employing acoustic actuation is by using surface acoustic wave (SAW). SAW detects the change in phase velocity of the surface acoustic wave caused by measurands (Wang et al. 2008). It is basically a piezoelectric acoustic wave sensor with a pair of interdigitated transducers, creating a mechanical wave which propagates through the substrate material and then converts back into an electric field for measurement. Wireless SAW sensors are reported to be involved in harsh environment applications (Cunha & Lad 2011, Wang et al. 2014). Wang et al.(2014) reported a wireless and temperature-compensated SAW vibration sensor (Figure 2.4-1) which has a decent readout distance of 1.5m. However, since the signal is transmitted as an electromagnetic wave, it is susceptible to interference. Furthermore, the behavior of the piezoelectric substrate will be another limitation at a temperature higher than the Curie temperature of its material.

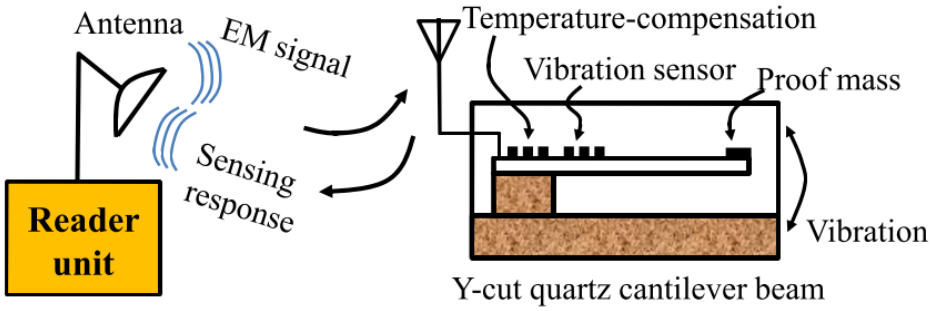

Figure 2.4-1 Schematic of the wireless SAW sensor (Wang et al. 2014)

2.4.1.2 LC circuit coupling

An LC circuit stands for an inductor-capacitor circuit which can act as an electrical resonator. A passive LC circuit normally consists of a measurand-sensitive capacitor and an inductor. The readout unit performs a sweep in a frequency range to detect the resonant frequency of the sensor circuit in order to get the measurement. Although no local battery is needed for exciting the passive LC circuit, an electric circuit is generally considered to be not tolerant to extreme environments unless special material (Qin et al. 2015, Wang et al. 2008) or insulation structure is employed.

Hong et al. (2015) proposed a high temperature wireless passive pressure sensor based on inductively coupled LC circuit (Figure 2.4-2). The sensor is fabricated with high-temperature co-fired ceramics (HTCC) whilst a heat insulation unit is used to keep the reader antenna in a safe temperature. Although it detects frequency signals in temperatures up to 500°C, the coupled distance is 2.5 cm, which is very short.

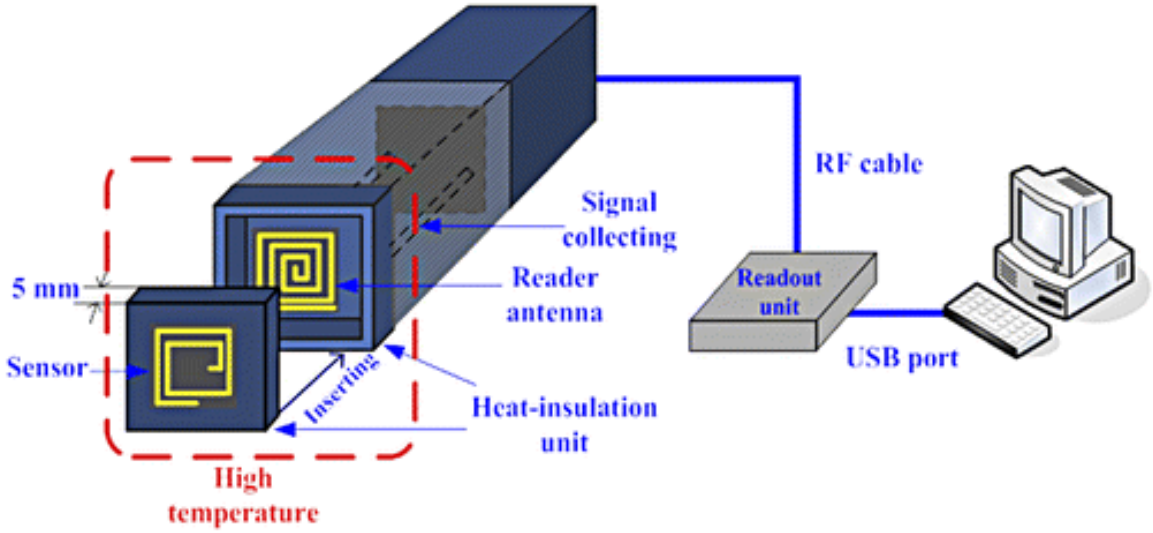

Figure 2.4-2 Hong's measurement system for a high-temperature environment

2.4.1.3 Optical actuation

Optical actuation on MEMS has been developing during the past three decades. The principle of optical actuation, also called photothermal excitation, is to use the thermal effect caused by incident light to form a bending or deflection, in order to produce the actuation. When the frequency of the modulated optical power is the same as the natural frequency of the microstructure which is small enough, resonance of the structure may occur. Fatah (Fatah 1992) explained the theory of optically actuating a doubly clamped beam with one-dimensional thermal model. The relationship between deflection amplitude A and incident laser intensity I_{abs} at resonance is given as

$$A = \left(\frac{3L\Omega Q I_{abs}}{16\omega_0}\right)^{1/2} \quad \textbf{(2.4-1)}$$

where L is the length of the doubly clamped beam, Ω is a characteristic of it material property, Q is the quality factor of resonance and ω_0 is the resonant frequency of the beam, which is also the value of the frequency of the modulated laser.

As Venkatesh (Venkatesh 1988) reviewed, Dieulesaint et al. reported optical activation of a silicon microresonator first in 1981. The resonance frequency was low and so was the Q factor. In 1985 Venkatesh et al. improved the experiment by fabricating smaller silicon dioxide strips which can be optically driven into resonance at the frequency of hundreds of kilohertz. The quality factor Q is slightly improved, which was sufficient to observe resonant frequency shifting with temperature changing. Strathclyde University (Thornton et al. 1986), Surrey University (Andres et al. 1986) and Imperial College London (Venkatesh & Novak 1987) also made further research on the sensor characterization and development.

Uttamchandani et al. (1987) from the University of Strathclyde developed a resonant diaphragm pressure sensor with optical actuation and interferometrical detection, shown in Figure 2.4-3. An aluminium coated silicon diaphragm is directly excited into vibration by an intensity-modulated laser beam, which has an average power of 1mW and a frequency up to 1MHz. The pressure in the capillary tube will stress the diaphragm and therefore change its resonant frequency. However, this type of vibrating membrane pressure sensor has a

common problem that the resonance frequency is not only dependent on the pressure but also the surrounding gas and its temperature (Elwenspoek & Wiegerink 2001). Therefore, directly optical actuation on a pressurized diaphragm is not an ideal solution.

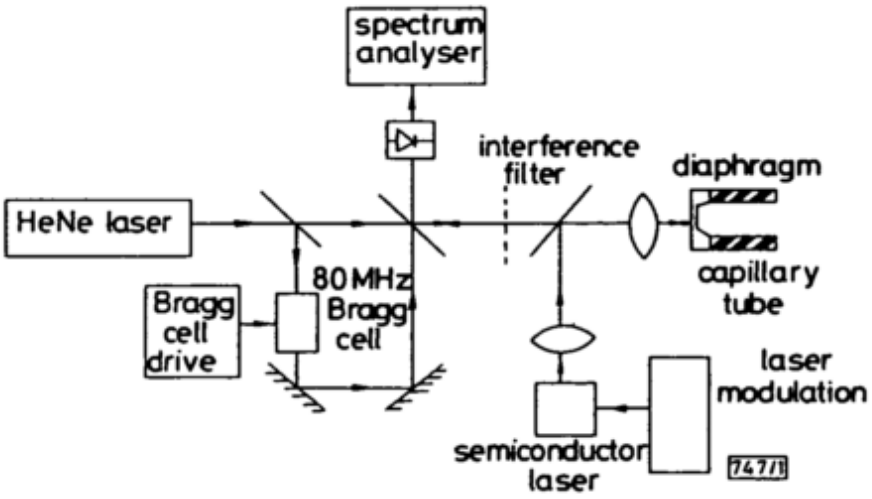

Figure 2.4-3 Experiment setup of the resonant diaphragm pressure sensor (Uttamchandani et al. 1987)

Hedley et al. (2004) from Newcastle University developed a method of using optical actuation for wafer level device characterization (see Figure 2.4-4). A nanosecond laser impulse is applied on the uncoated device to drive all modes into resonance. The actuation laser is unfocused in order to avoid any damage to the samples. The device size is 300 μm x300 μm x3 μm and the power of the laser impulse being used is from 2.5~8 uJ. Although the method is not intended to actuate any sensor element, its impulse optical actuation provides a novel and harmless way to produce all modes resonance.

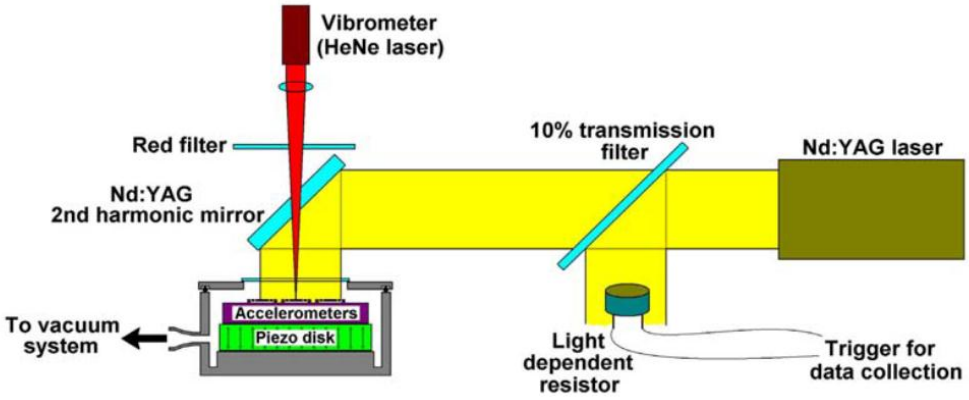

Figure 2.4-4 Setup of Hedley's testing system (Hedley et al. 2004)

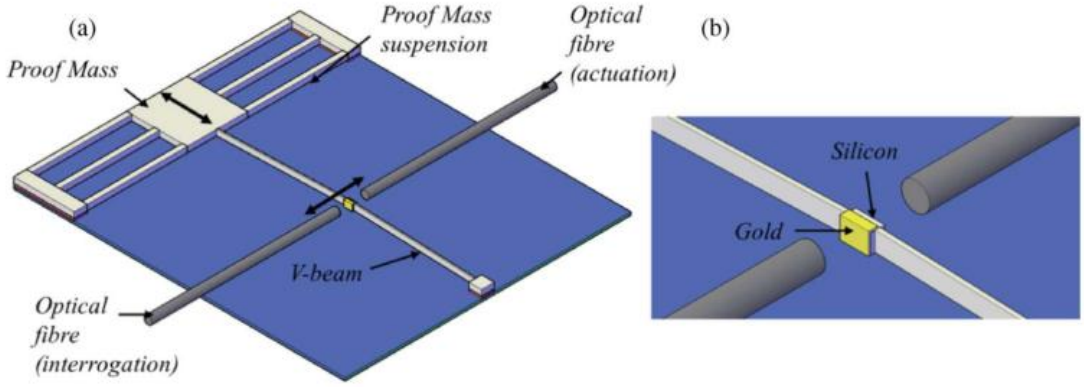

Figure 2.4-5 (a) Schematic of the accelerometer system. (b) Close-up view of the optics (Davies et al. 2014)

A paper from Imperial College London (Davies et al. 2014) reported a method of calibrating optical accelerometer using photothermal actuation. The setup of the calibration system is shown in Figure 2.4-5. The gold coated surface of the V-beam and the end surface of the cleaved optical fiber form a Fabry-Pérot (F-P) cavity which is used to perform interferometric interrogation. An F-P cavity consists of two parallel partially-transmissive plates with highly reflective inner surfaces. The light incident into the cavity will experience multiple reflections and

refractions, producing multi-beam interference. When the incident wavelengths match the optical resonance condition of the cavity, i.e. the reflected beams are out of phase so that the destructive interference between them cancels each other, the transmittance of those wavelengths will reach the maximum (Perez & Shkel 2005). For a broadband light source incidence, the optical resonance will produce transmittance peaks in the spectral output. An F-P cavity with a changing gap length can be used in displacement measurement as the variation of the cavity length changes the resonant wavelength, which is reflected as a shift of transmittance peaks in the output spectrum. Therefore, by monitoring the peak shift in the spectrum, the cavity length change can be detected. The system applied a photothermal actuation on one side of the beam to cause deflection in order to calibrate the accelerometer using the F-P cavity measurement on the other side of the beam. This research provides an example of static photothermal actuation.

Photothermal excitation is also employed to improve the performance of atomic force microscopy (AFM) tapping mode (Kiracofe et al. 2011, Labuda et al. 2014). Tapping mode is that the AFM cantilever is driven into resonance, commonly by piezoelectric excitation, and the oscillation is optically measured when the tip of the cantilever is interacting with the sample surface to detect its morphology. The AFM cantilever is normally mounted into a holder with a piezoelectric shaker that is clamped to the AFM frame. The problem is that the piezo drive does not provide a clean, stable and frequency independent actuation. Also, the drive

piezo relies on mechanical coupling to actuate the cantilever, but when connected to the AFM body, it becomes a part of a larger mechanical system with much more complex resonance spectrum. Therefore, the amplitude-frequency response of a piezoelectrically driven cantilever often displays a distortion of sharp peaks and valleys, which is a product of the intrinsic cantilever response and the piezo drive response. Labuda et al. reinvented the tapping mode using photothermal excitation. By focusing a modulated laser spot at the clamped end of the cantilever, photothermal excitation drives only the cantilever but no other system resonance compared with the piezoelectric method. Therefore, the former provides more stable and accurate frequency response.

As a summary, research that have been carried out to develop the technique of optical actuation is reviewed. Optical actuation has the advantage including undisturbed resonance spectra, suitable in fluid compared with those techniques with electronic elements, and allowing flexible resonator shape design (Bircher et al. 2013). There have been researchers studying lasers actuating pressurized diaphragm, MEMS device for characterizing, microbeams in order to achieve static or dynamic displacement. Laser power has been reported from several hundred microwatts (Venkatesh 1988) to 30 milliwatts (Davies et al. 2014). Even an unfocused laser spot can be used in the actuation (Hedley et al. 2004). Limited theoretical work has been reported to explain the process of optical actuation in complex conditions rather than using a one dimensional model for simple beam analysis. Although a few researchers have been working on optical

actuation within a short range, it has the potential to operate over a distance up to a few hundred meters, provided that the light source power is sufficiently large to produce a desired temperature rise on the actuator. The main factors limiting the actuation range to get larger are as follow. First, the difficulty of aligning the actuation light spot with the sensor will increase significantly over distance; Second, the beam dispersion will cause the power intensity landing on the sensor to decrease; Furthermore, the atmospheric impacts such as rain, fog, dust and heat will be significant for a greater range as they can attenuate the optical signal propagation (Malik & Singh 2015) and cause signal error (packets loss), which affects the accurate delivery of a high frequency modulated actuation light.

2.4.2 Wireless interrogation

Wireless interrogation is another key technique for extreme environment sensing. It saves the cost of the cable network establishment, lowers the requirement of maintenance and more importantly leaves the interrogation system in a relatively safe environment which is more suitable for human or electrics to work in than the extreme environments. Several wireless interrogation methods are reviewed and discussed as follow.

2.4.2.1 Inductive interrogation

Inductive interrogation utilizes electromagnetic induction to transfer a signal between coils wirelessly. The working principle is introduced in 2.4.1.2 as it is a part of the LC coupling. Some researchers have applied inductive interrogation in their sensor (Knobloch et al. 2013, Hong et al. 2015) to form systems for extreme environments. However, the magnetic field fall off rate is the reciprocal of cubic driving coil radius (Knobloch et al. 2013). Therefore the coupling distance of inductive interrogation is restricted by the size limitation of a micro sensor, usually several centimetres.

2.4.2.2 Interferometry interrogation

Interferometry is another method of wireless interrogation, which can optically detect precise changes in displacement of a sensor structure. Generally, Fabry-Pérot (F-P) cavity and Laser Doppler Vibrometer (LDV) are the two main approaches utilizing interferometry interrogation.

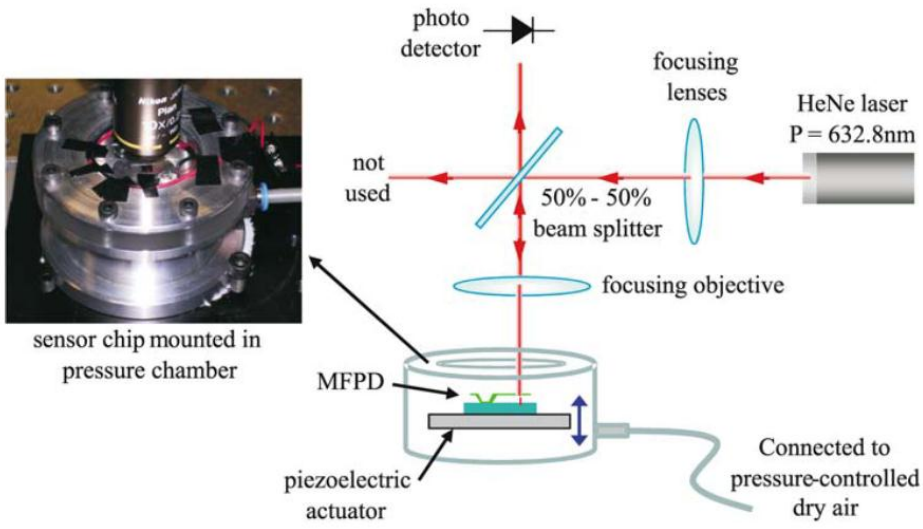

Figure 2.4-6 Setup of Nieva's pressure sensor

The F-P approach is based on detecting the height change of an F-P microcavity, which is defined by two optical surfaces. A laser beam that incidences into the F-P microcavity will have multiple reflections between the two inner mirror surfaces. The total reflected interferometric light depends on the distance between the two reflecting surface (Nieva et al. 2009). Making one of the surfaces a moving part that has varying frequency or displacement will turn the F-P microcavity into an interferometric sensor. Nieva (Nieva et al. 2009) in the University of Waterloo presented a pressure sensor system where a cantilever sits on a substrate (Figure 2.4-6). They formed an F-P cavity that can be read optically, sending the frequency signal of cantilever resonance which depends on the pressure in the pressure chamber. Similar measurement arrangements with F-P interferometry have been reported by Liu et al.(2002), Davies et al.(2014) and Poeggel et al. (2015). Complicated alignments are required in all these setups.

An LDV is a scientific instrument that also utilizes interferometry to perform wireless interrogation. It is widely used in the detection of vibration and deflection in MEMS research (Zhou et al. 2003, Hedley et al. 2004, Wang et al. 2009, Lee et al. 2015). An LDV emits a laser beam on an object surface and analyses its out-of-plane velocity by measuring the frequency (or phase) difference between an internal reference beam and the reflected beam. Since the measurement result is the average over the laser spot area, the beam from an LDV normally needs to be focused down in order to measure the motion of small features. And these will introduce limitation to the interrogation distance and more optical

alignments. Furthermore, an LDV itself is normally a high cost instrument that would be added into the sensor system.

2.4.2.3 Optical position sensitive interrogation

Position sensitive interrogation is to read the optical signal beam by its spot position. It is usually working cooperatively with a mirror surface from where the reflected beam is directed into the interrogation system. The optical signal carries information normally in the form of beam spot displacement and frequency.

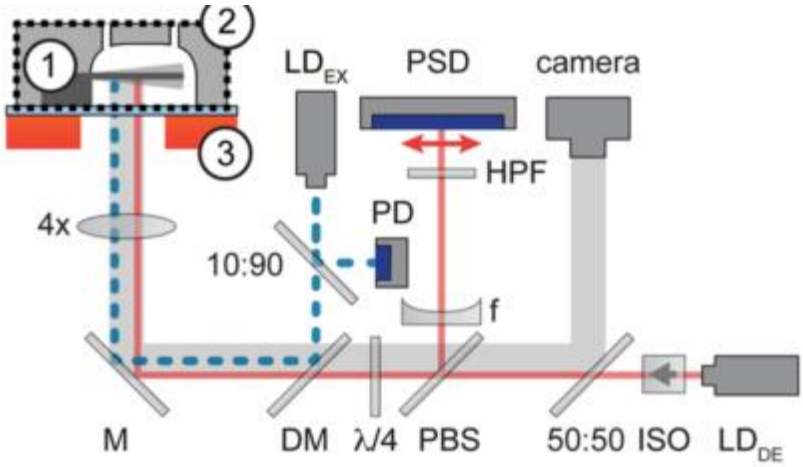

Figure 2.4-7 Optical viscosity and mass density sensor system

Bircher et al. (2013) reported a viscosity and mass density sensor which can work in microfluidics environment where piezoelectric excitation is unsuitable, shown in Figure 2.4-7. A microcantilever is excited and detected by two laser beams of different wavelengths (406nm for driving and 780nm for detecting), shown in Figure 2.4-7. A gold layer is deposited on it top surface in order to

separate the absorption rates of the two lasers. The reflected beam (in red line) is picked up using a position sensitive detector (PSD). It measures the time dependent displacement of the reflected beam spot, from which the vibration frequency of the microcantilever can be calculated. The frequency is then related to the fluid viscosity in the chamber where the microcantilever is located, through the eigenfrequency value and the width of the frequency peak.

Position sensitive interrogation is attractive as a remote interrogation method for extreme environment. However, the position of the reflection beam spot is not easy to capture if the working distance is long as slightly tilting the mirror surface will cause a huge angular movement of the reflected beam. Therefore, a retroreflective structure is needed to limit the reflected beam spot in a predictable area. Details of retroreflective structures will be introduced in section 2.5.

2.4.3 Enhanced materials

Enhanced materials can make structural or electronics elements in MEMS, that used to be susceptible in extreme environments, to become suitable by improving some mechanical or electrical properties. These special materials have also been developed to reduce the detrimental impact of extreme environments. For high-temperature environments, special piezoelectric materials can be used to provide higher Curie temperature. For instance, bismuth titanate has a higher operational limit of 650°C whilst lithium niobate can operate intermittently at up to 760°C (Bogue 2012). Silicon carbide is employed to

replace silicon in some situations since silicon begins to deform plastically at around 600°C. Silicon carbide has larger band gap and better maintenance of mechanical properties (Wijesundara 2011). Therefore, it can meet both structural and electrical requirement at a higher temperature. Work has been published on developing MEMS with silicon carbide for harsh environment applications (Cheung 2006, Jiang & Cheung 2009). Sapphire is also a material resistant to high temperature. A company named Oxsensis launched the Wave-Phire DPT950, a pressure/temperature sensor based on sapphire structure Fabry-Perot cavity techniques, which is the first sensor that can do all dynamic pressure, absolute pressure and temperature measurements at high temperature, even above 1000°C (Bogue 2012). The reason for using sapphire is that its Young's modulus remains sufficiently high to allow the Fabry-Perot to function up to 1400°C. For radiation environments, higher temperature piezoelectric materials are generally resistant to the effect of radiation, like Endevco 2273 A series can work at 6.2×10^{10} rad gamma exposure and $3.7 \times 10^{18} n/cm^2$ neutron flux (Bogue 2012).

Enhanced materials can be integrated with above techniques to form a comprehensive sensor design. These materials provide guidelines to the material selection in this research.

2.4.4 Summary of existing extreme environment sensor techniques

In section 2.4, a range of existing sensors techniques that can be adopted in extreme environments has been reviewed. Although there are a few commercially available sensors which can work in very high temperature or radiation with the support of enhanced materials, most of them are wired sensors and costly in the materials they reliy on. Among the passive actuation and wireless interrogation techniques, optical actuation and optical position sensitive interrogation have shown good feasibility as they are the best in the potential operating distance and in signal security. As long as a line of sight is available, these techniques can be employed with minimum maintenance required. However, no research has been done on developing a sensor working in extreme environments with both optical actuation and interrogation over a relatively long distance.

2.5 Review on Micro Corner Cube Retroreflector (CCR)

2.5.1 Retroreflectors

Retroreflectors are devices that can reflect incident light back to its source. The angle of incidence at a retroreflector can be greater than zero while a planar mirror can only get the retroreflection if the incident light is perpendicular to the mirror surface, i.e. at a zero angle of incidence. For this reason, a retroreflector is considered to be introduced into the research to build up a more flexible system without the need of delicate optical alignments and to make a more remote interrogation possible. Spherical retroreflector and CCR are the two main types

of retroreflectors. A spherical retroreflector consists of a refractive optical element and a reflective surface that is located on its focal surface whilst a CCR is formed by three mutually perpendicular mirrors, as shown in Figure 2.5-1. They can be normally found both in space and on the ground, functioning in the tail lamp of vehicles, road signs, satellites, laser ranging, locating and optical communication systems (Kunimori et al. 2012).

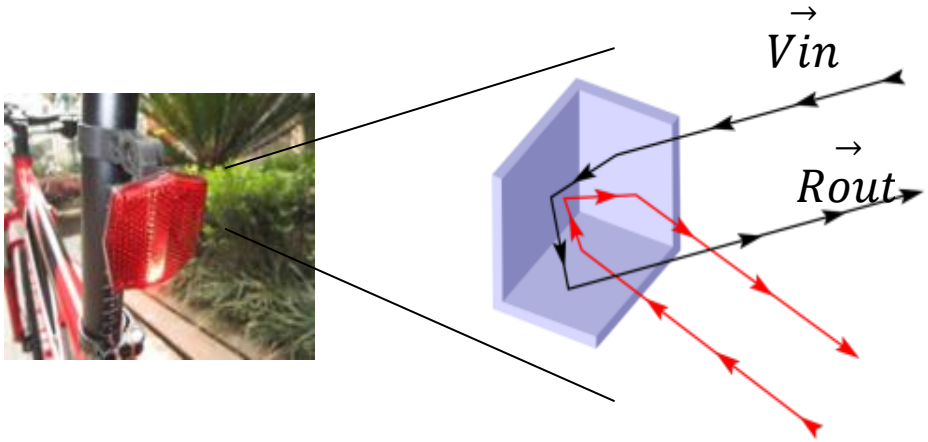

Figure 2.5-1 CCR application on bike tail lamp and a schematic of retroreflection in a CCR structure

2.5.2 Current research on MEMS with micro CCR

As mentioned above, retroreflection only occurs when all the three mirrors of a CCR are in the exact mutually perpendicular position. Ray tracing through a CCR is derived as follow. For reflection on a mirror, the reflected light direction is given by (Vasquez & Judy 2007)

$$\vec{R} = \vec{V} - 2\vec{N}\left(\vec{V} \cdot \vec{N}\right) \qquad \textbf{(2.5-1)}$$

where $\vec{R}$ is the reflected light, $\vec{V}$ is the incident light and $\vec{N}$ is the normal vector of the mirror. For the retroreflection shown in Figure 2.5-1, $\vec{Vin} = \left(-\vec{X}, -\vec{Y}, -\vec{Z}\right)$ is applied three times with the respective mirror normal vectors using equation(4.2-1). $\vec{Rout} = \left(\vec{X}, \vec{Y}, \vec{Z}\right)$ is obtained when three mirrors are mutually perpendicular.

A micromachined CCR is suitable to work as a part of a MEMS device since the direction of its reflected light can be modulated by tilting one of the three mirrors at a controlled frequency, which forms an optical communication, or by tilting at an unknown frequency which is to be measured, i.e. remote sensing. Because the size of a micro CCR is relatively small, the tilting mirror can be very thin and light. It facilitates low power consumption actuation and makes the mirror sensitive to slight changes of measurands.

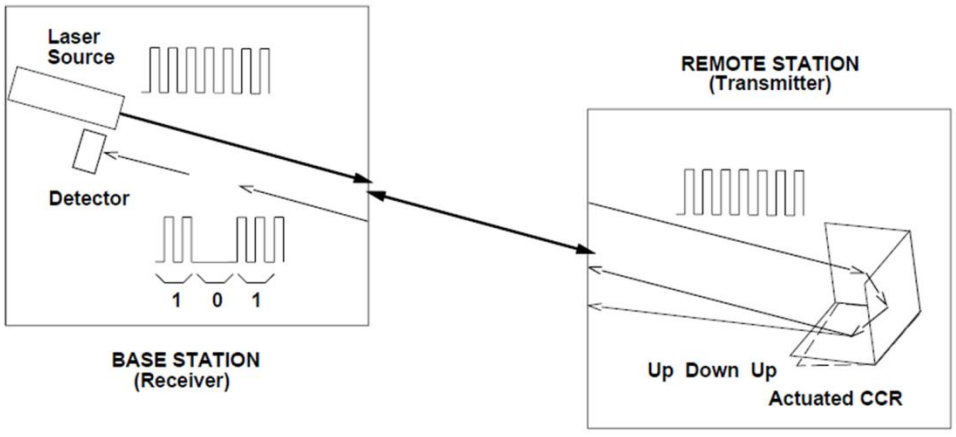

Figure 2.5-2 Optical communication using micromachined CCR (Chu et al. 1997)

Micro CCR has been proved working in remote optical communication. The Berkeley's "Smart Dust" project, which started late last century, developed an integrated cubic millimeter sensor node consisting of a sensor, power supply, analog circuitry, a programmable microprocessor and optical communication system (Warneke et al. 2001). It was proposed that a large amount of the smart dust sensor nodes can be widely spread onto the earth in order to form a sensor network, which monitors different measurands and communicates with the base station. Micro CCR is used on those smart dust nodes to enable passive optical transmission, which needs no optical power supply from the sensor node (Kahn et al. 1999). They proved that these sensor nodes can transmit a signal over the range of 180m (Zhou et al. 2002) or even longer. Figure 2.5-2 shows a schematic of optical communication using micro CCR (Chu et al. 1997). Misaligning one of the mirrors will disturb the retroreflection, consequently coding the return signal picked up by the detector. A similar CCR communication system is also reported by Lee and Park (2010).

CCRs have also been used as a part of sensor structures. A zero-power magnetic field sensor was developed (Vasquez & Judy 2007). Making one of the mirrors of a CCR tilting with the intensity of the magnetic field applied, as shown in Figure 2.5-3, its intensity can be obtained by detecting the angular displacement of the mirror optically. As discussed in the paper, reflected light from a misaligned CCR will be divided into two beams pointing two directions, the angle between which is relevant to the tilting angle of the mirror and the incident

laser orientation. The latter can be solved by having a calibration CCR with a known misalignment located next to the sensor.

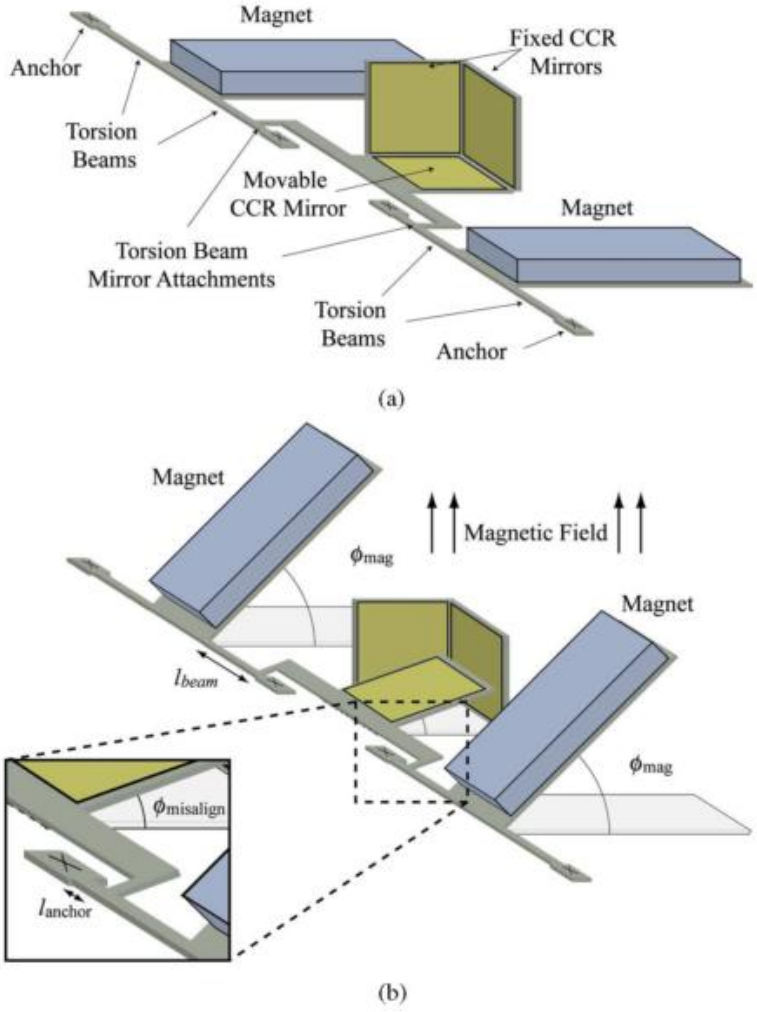

Figure 2.5-3 Schematic of the zero power magnetic field without (a) and with (b) an external magnetic field applied

2.5.3 Micro CCR fabrication

Micro CCRs are fabricated with silicon and well-developed silicon fabrication processes. The horizontal mirror, which is able to be actuated, is normally

fabricated using surface micromachining technology while the other two mirrors are fabricated separately and subsequently assembled into the vertical position. For example, some researchers introduce the method that all the three mirrors are fabricated on the same wafer surface and then folded out-of-plane to form a CCR with the help of supporting structures such as micromachined hinges and limiters, shown in Figure 2.5-4 (Hong et al. 2005, Vasquez & Judy 2007).

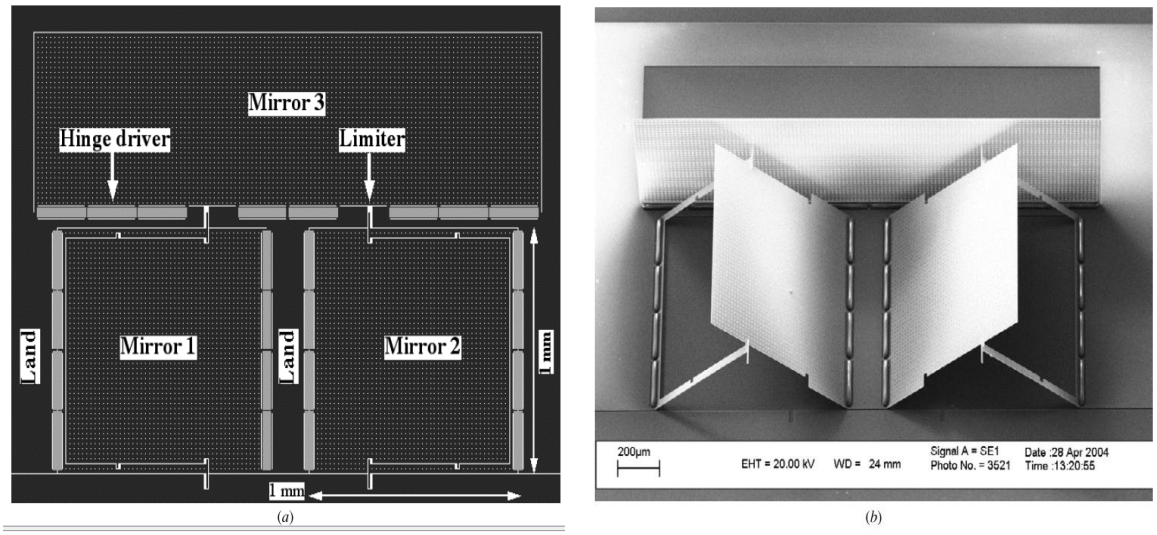

Figure 2.5-4 Micro mirrors before (a) and after (b) assembly by Hong et al.

In addition, Lee & Park (2010) developed an optical CCR communicator with one of the mirrors actuated by piezoelectric transducers, shown in Figure 2.5-5. The horizontal mirror is fabricated using multiple layer silicon process whilst the two orthogonal vertical mirrors are fabricated from a double-SOI (silicon-on-insulator) wafer, after which the CCR is formed by manually aligning and inserting the vertical mirrors into the preset SU-8 holder.

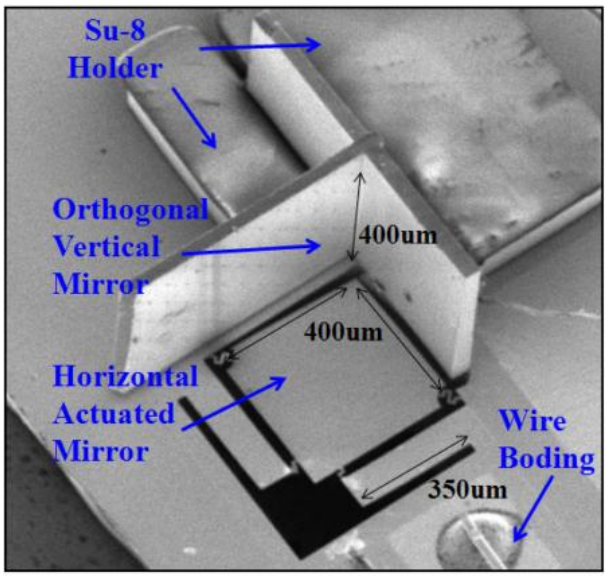

Figure 2.5-5 CCR communicator fabricated by Lee and Park

Most of the micro CCRs mentioned in the literature are difficult and expensive to fabricate, mainly because micro CCRs are generally fabricated using multi-user MEMS process which involve lots of layers of processes. Also, the two orthogonal vertical mirrors and the third mirror are fabricated separately. This will induce the need of assembly afterwards, which is either self-assembly or manual assembly. Either of the methods increases the cost and difficulty of the fabrication whilst potentially decreasing the accuracy and robustness of the system.

2.6 Conclusions on the Literature and Knowledge Gaps

In this chapter, the technologies relevant to developing a passive and remote sensor that is suitable for operation in extreme environments are reviewed. MEMS and the reason for MEMS sensors having limited applications in extreme

environments are introduced. Existing extreme environments sensing technologies have been reviewed. Also, the potential that a micro CCR structure can facilitate remote interrogation is illustrated. There have been papers reporting research and techniques on sensing in extreme environments, but they are either wired sensors or wireless sensing within short range due to the limitation of working principles. Optically actuating and interrogating a resonant sensor has shown advantages in good sensor accuracy and potentially long operation distance, as long as a line of sight is available. Micro CCR structure has been adopted in several sensor and communicator designs, enabling long distance remote analog or digital signal transference.

However, there have been a few knowledge gaps in the literature. First, there haven’t been sensors with both passive actuation and remote interrogation over a relatively long distance, which is an important factor for zero-power and low maintenance extreme environments sensing. Second, a CCR is a key structure for long distance optical interrogation, but it has not been reported to be working with any resonant tilting mirror structure that can be optically actuated. Furthermore, micro CCR fabrication technologies reviewed in the literature are very complicated and costly for the purpose of this application.

Therefore, the proposed system is going to be achieved with the following originalities. First, the principle of photothermal actuation of a paddle (tilting mirror) resonator will be developed. Second, the fabrication process of CCR is

going to be simplified without compromising its optical properties. Third, a CCR will be combined with the optically actuated resonator sensor in order to be optically interrogated over a relatively long operating distance.

Chapter 3: Design, Analysis and Modelling of an Optically Actuated Paddle Resonator

3.1 Introduction

In this chapter, a micro paddle resonator, shown in Figure 3.1-1, actuated by photothermal effect is designed and analytically modelled. Optically introduced thermal stress is used to actuate a fixed-fixed beam periodically, whose vibration tilts the paddle attached to it into resonance due to the unsymmetrical supporting position. A change in the axial stress of the fixed-fixed beam will affect the resonant frequency, which can turn the paddle resonator into a pressure/temperature sensor element. The design specifications and material selection are discussed first. Then the principle of photothermally actuated paddle resonator is explained, followed by analytical modelling and finite element analysis simulation to verify the actuation parameters and prepare for the prototype fabrication.

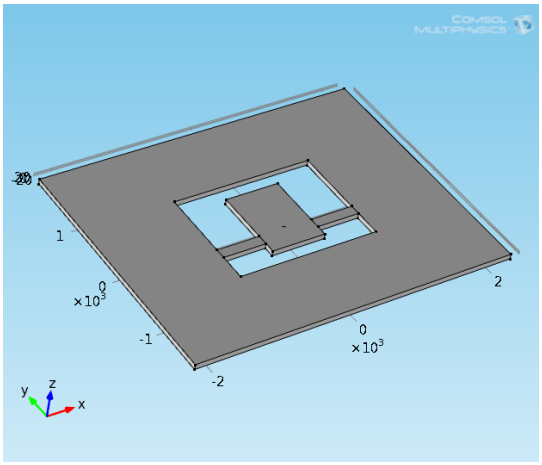

Figure 3.1-1 Schematic diagram of a paddle resonator

3.2 Paddle specifications

Specifications of the design are set as follow. First, a paddle structure is designed to be able to stand the working condition such as high temperature and radiation in extreme environments. Second, the resonance of the paddle needs to be sensitive to the axial stress in order to become a sensor element. Third, the paddle structure can be driven optically. This limits its size within the micron to nanometer scale due to the requirement of a small thermal time constant which will be discussed later in this chapter. Also, the structure needs to be able to vibrate in and out its horizontal position which allows it to be optically interrogated. Furthermore, the paddle needs a tilting angle that is large enough when being actuated so that a difference can be seen by a detector over a distance away, set to be 3m at the development stage. Assuming the diameter of a detecting aperture is 1cm, the oscillating paddle needs to have a tilting angle of 0.1° (about 1.7mrad) in order to allow the reflected spot passing the area of detection. All these specifications are constraining the design parameters which will be discussed in the following sections.

3.3 Material selection

As discussed earlier, the resonant sensor in this research is aimed to be applied in extreme environments such as high temperature and radiation. Enhanced materials have been developed and adopted in many extreme environment

applications. Although in this research, the principle of optical actuation and interrogation has eliminated the concern of materials loosing electric properties, the structural material must be capable of retaining sufficient mechanical properties in the harsh working conditions.

Silicon carbide and sapphire are good candidate materials for high-temperature applications as they can provide stable mechanical properties like Young's modulus in the temperature above 600°C to 1000°C. For radiation environment, zirconium alloy is used as nuclear fuel cladding and structural components in nuclear reactors because of its hexagonal close packed crystallographic structure and low neutron capture cross section. Also, silicon carbide has been shown to be stable in high irradiation and has comparable neutron capture rate to that of zircaloys (Barrett et al. 2012).

Materials listed above can be selected as the structural materials of the paddle structure. However, some of the materials are not easy to fabricate, for example, the fabrication of micro zirconium structure is an issue as it is extremely flammable when the specific surface area is large.

On the other hand, silicon is a material widely used to fabricate MEMS resonators. In spite of its electrical properties getting significantly affected above the temperature of 150°C (Bogue 2012), silicon can be a good material for building a resonator up to the temperature at which it begins to creep, typically

between 350°C to 500°C (Knobloch et al. 2013). Also, it is believed that the mechanical properties do not change when irradiated at a relatively low dose (Knudson et al. 1996). Therefore, silicon is still a good choice for prototyping fabrication and testing for this paddle design.

Also, nickel is another easily available hard metal material that has a melting point of 1455°C. It has a different combination of thermal properties to that of silicon. Moreover, it is suitable for micro electroforming. Hence nickel is another material for prototyping and comparative test in this study.

3.4 Resonant frequency shift with stress

The first two modes of resonance for the paddle structure are torsional mode and translational mode, as shown in Figure 3.4-1. The colour distribution in the plots indicates the amplitude of structure displacement in each resonance mode. In the torsional mode, the tilting motion of the paddle dominates while the supporting beams barely move. But in the translational mode, the bending motion of supporting beams dominates while the paddle is forced to tilt into the opposite direction due to its own inertia. Frequency shift with the axial stress of both modes is discussed in this section. Paddle dimensions used in the following discussion are labelled in Figure 3.4-2.

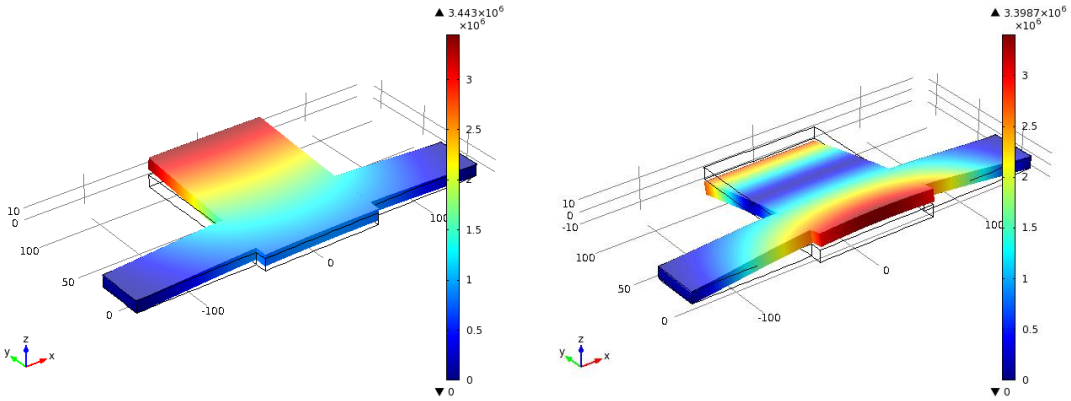

Figure 3.4-1 The first two resonance modes shape: torsional (left) and translational (right)

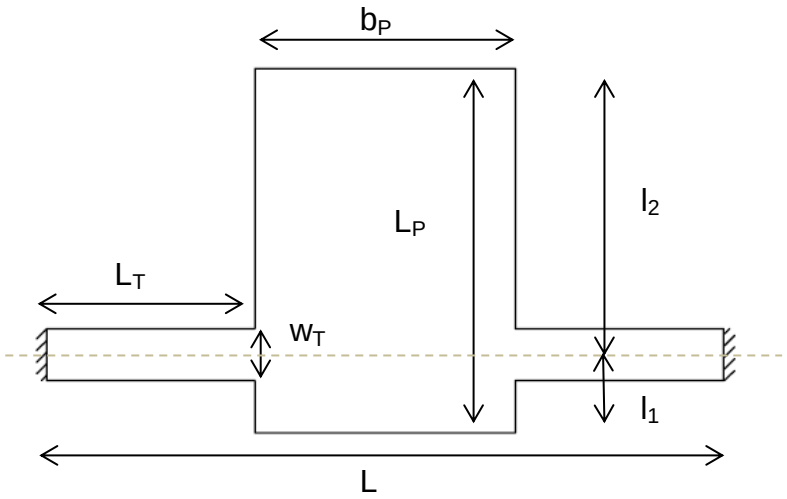

Figure 3.4-2 Paddle dimensions

When the paddle is vibrating in torsional mode, the torsional spring constant (K_T) of a supporting beam with axial stress S is (Lee et al. 2015)

$$K_T = \frac{\kappa G}{L_T}\left[1 + \frac{1}{4}\left(\frac{h}{w_T}\right)^2 \frac{S}{G}\right] \quad \textbf{(3.4-1)}$$

where

$$\kappa = h w_T^3 \left[\frac{1}{3} - 0.21\frac{w_T}{h}\left(1 - \frac{w_T^4}{12h^4}\right)\right] \quad \textbf{(3.4-2)}$$

L_T is the length of one supporting beam, h is the paddle thickness, w_T is the width of supporting beam, and shear modulus

$$G = \frac{E}{2(\gamma + 1)} \quad \textbf{(3.4-3)}$$

where E is Young's modulus of the material and γ is its Poisson's ratio.

Torsional mode natural frequency is calculated as

$$f_{torsion} = \frac{1}{2\pi}\sqrt{\frac{2K_T}{J_p}} \quad \textbf{(3.4-4)}$$

where the mass moment of inertia J_P is given by

$$J_p = \rho b_p \int_{-l_1}^{l_2} \int_{-\frac{h_p}{2}}^{\frac{h_p}{2}} (x^2 + y^2)\,\mathrm{dx}\,\mathrm{dy} \quad \textbf{(3.4-5)}$$

b_p is the width of the paddle, h_p is the paddle thickness, l_1 and l_2 are the distance between paddle edge and the axis of rotation (l_1+l_2=L_P, the full length of the paddle), and ρ is the density of material.

For a paddle structure in translational mode, the translational spring constant is,

$$K_B = \frac{2Ew_T h^3}{L_T^3} \quad \textbf{(3.4-6)}$$

where E is Young's Modulus. So the translational natural frequency is,

$$f_{trans} = \frac{1}{2\pi}\sqrt{\frac{K_B}{M}} \quad \textbf{(3.4-7)}$$

where M is the paddle mass. When axial force N is applied, the first order translational resonant frequency is modified due to stress S and becomes (Bao 2005)

$$f_1(N) = f_{trans}\left(1 + \frac{0.2949}{2}\frac{NL^2}{12EI}\right) \quad \textbf{(3.4-8)}$$

where L is the full length of the fixed-fixed beam, I is second moment of area of the supporting beams.

Hence the frequency shift Δf is

$$\frac{\Delta f}{f_{trans}} = 0.1475\frac{S}{E}\left(\frac{L}{h}\right)^2 \quad \textbf{(3.4-9)}$$

Nonlinear vibration happens when the restoring force does not linearly change with the deformation. Translational vibration has the potential to display nonlinear behaviour as the deflection may cause stiffness change in the supporting beams due to geometric nonlinearities. Since the deflection is very small compared to structure thickness in this application, the nonlinearity of the paddle vibration is very small so that it is ignored in the derivation.

With the same material properties and axial stress, frequency shift of the torsional mode benefits from maximizing aspect ratio $\frac{h}{w_T}$, while the frequency shift of the translational mode benefits from maximizing $\frac{L}{h}$.

Setting $h = h_P = 73\mu m$, $w_T = 150\mu m$, L_T is 600μm, b_P is 750μm, L_P is 1050μm, l_2/l_1=11:3, L is the total length 1950μm, the resonant frequency for torsional mode is 32kHz while that for translational mode is 76kHz. Calculating with the material properties in Table 3.5-1, frequency change with axial stress of a nickel structure is shown in Figure 3.4-3.

It has been shown in Figure 3.4-3 that the frequency of both resonance modes varies with axial stress. However, for a paddle with the provided dimensions, resonance in the translational mode is seen to have a frequency shift 3 orders of magnitude larger than for the torsional mode. Therefore, for structures with similar shapes, a frequency near translational mode is more suitable for the use of sensor actuation and interrogation.

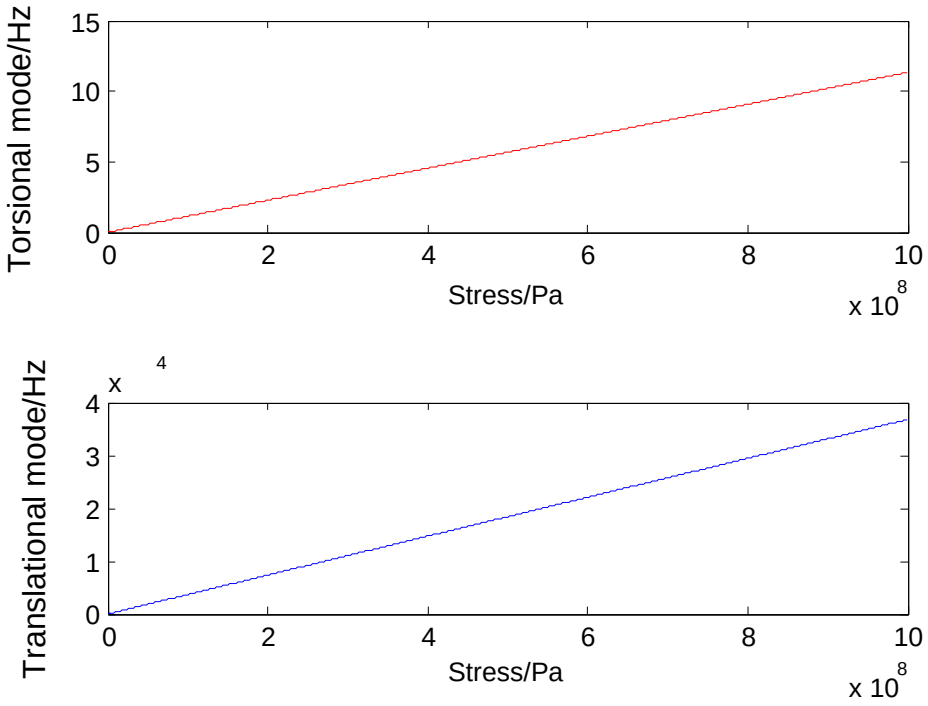

Figure 3.4-3 Paddle structure frequency change with axial stress in both modes

3.5 Photothermal effect on structure

When a light beam is applied to a surface, the optical penetration depth can be calculated from the incident wavelength and the imaginary part of the material's index of refraction, which is also called the absorption index. For a visible light applied to metal materials, the optical penetration depth is usually a small fraction of the incident light wavelength (<10%) (Fatah 1992). Since our structure thickness is in the micron range, it is optically thick. Therefore, a fraction of the power turns into heat energy whilst the rest is reflected. The proportion is related to the absorption rate, which varies with incident light wavelength. For a gold surface, the absorption is about 67% at the excitation wavelength of 406nm. It changes to less than 3% at an excitation wavelength of 780nm (Bircher et al. 2013).

Applying periodical optical power on the top of the structure, the thermal diffusion length μ is (Marín 2010)

$$\mu = \sqrt{\frac{2K}{\rho\omega C_p}} \qquad \textbf{(3.5-1)}$$

where K is the thermal conductivity, C_p is the specific heat capacity, ρ is the density and ω is the modulation frequency of the activating laser beam. Thermal diffusion length μ gives the distance within which an appreciable energy transfer takes place.

Table 3.5-1 Material properties of Silicon and Nickel

Parameters	Si	Ni
Young's modulus [Pa]	131e9	219e9
Density [kg/m^3]	2330	8900
Coefficient of thermal expansion [1/K]	4.15e-6	13.4e-6
Thermal conductivity [W/(m*K)]	163	90.7
Specific heat capacity [J/(kg*K)]	703	445
Poisson's ratio	0.27	0.31

With the material properties in Table 3.5-1, the thermal diffusion length μ at a driving frequency of 100 kHz is 17.8μm for silicon and 8.5μm for nickel. At a driving frequency of 10 kHz, μ is 57μm for silicon and 27μm for nickel.

When the thickness of the structure is larger than μ, once optical power is applied to its top surface, there will be an obvious temperature gradient from top to bottom surface. The expansion of the material due to the temperature increase is given by

$$\frac{\Delta L}{L_0} = \alpha \Delta T \qquad \textbf{(3.5-2)}$$

where ΔL is the linear expansion, L_0 is the original length, α is the coefficient of linear thermal expansion and ΔT is the change in temperature. Assuming that the beam consists of a finite number of layers with one dimension heat transfer, the axial expansion will decrease from the top layer to the bottom as ΔT reduces with

depth. This will generate a bending moment periodically which drives the structure into vibration. A thermally thick device has the advantage that (1) the good frequency response will present with the axial stress changing when it is in torsional mode; (2) the device is robust and easy to fabricate.

When the thickness of a structure is smaller than μ, the structure is thermally thin and the temperature across its thickness is taken to be uniform. Vibration is generated by periodical stress in the axial direction. It has the advantage that (1) since the paddle is eventually used as a mirror, a thin structure with uniform temperature has the advantage that it will avoid thermal bending and keep the paddle surface flat during vibration; (2) the frequency shift of the translational mode will be more appreciable, benefiting from the thinness. However, it makes the microstructure more brittle.

Since vibration in either situation is caused by axial stress or thermal bowing of the supporting beams, the translational mode has more potential to be activated. Therefore a thermally thin structure is more desired as it enhances the response of the translational mode.

3.6 Thermal time constant

Photothermal actuation essentially relies on the periodical changing thermal stress to drive the paddle structure. Thermal actuation is usually known to be a

slow process due to the nature of heat transfer. It is more commonly used for low-frequency applications unless the structure is very small.

Thermal time constant indicates how fast the heat is dissipated to 1/e of the initial value, as shown in Figure 3.6-1. In order to drive the structure into full deflection vibration, the heat causing the bending moment must be able to escape the system much faster than the mechanical recovery of the bending. Therefore the excitation needs to be slow enough for the dynamic temperature across the structure to follow. This in another word means that the period of actuation (i.e. mechanical time constant, $\frac{1}{f}$) must be longer than the thermal time constant τ of the actuated structure, usually 10 times (5τ to raise, 5τ to recover) to allow a temperature change of 99.3% (Sehr et al. 2002). The highest operational frequency f_0 is given by

$$f_0 \leq \frac{1}{10\tau} \qquad \textbf{(3.6-1)}$$

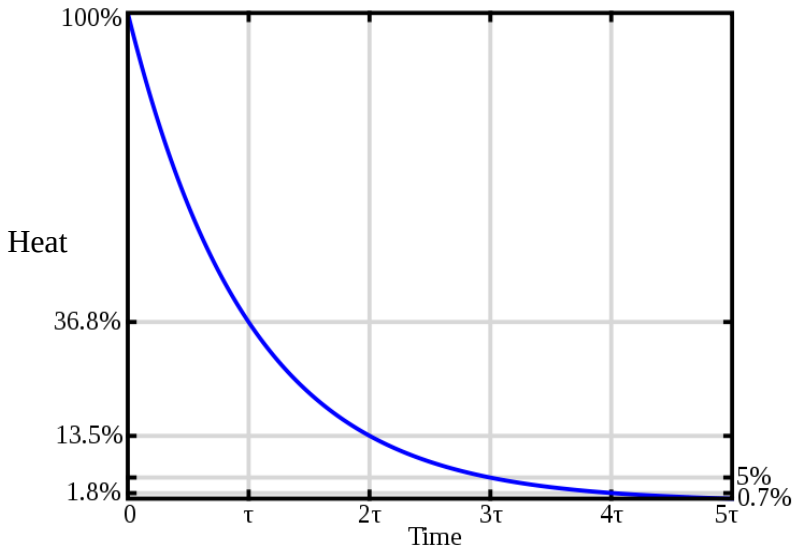

Figure 3.6-1 Time response of heat dissipation

The heat dissipation phenomena can be modelled as a low-pass electrical RC circuit (Brand et al. 2015).

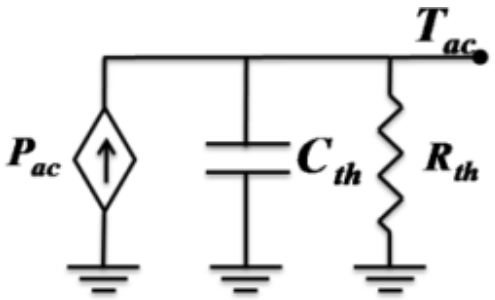

Figure 3.6-2 Equivalent RC circuit of a thermal model

The thermal time constant τ of the paddle structure resulting from heat transfer through the supporting beams to the substrate is given by

$$\tau = R_{th}C_{th} = \frac{L_T}{2KA} \times \rho V C_p \qquad \textbf{(3.6-2)}$$

where R_{th} is thermal resistance of the beams, C_{th} is the thermal capacity of the paddle, L_T and A are the length and cross-sectional area of the supporting beam, K is the heat conductivity of the material, ρ is the density of material, C_p is the specific heat capacity of the material, V is total volume of the paddle structure.

There is also a small amount of heat transfer Q between the resonator and ambient air,

$$Q = -\rho C_p V \frac{\mathrm{d}T}{\mathrm{dt}} = hA_s\left(T_{(t)} - T_a\right) \qquad \textbf{(3.6-3)}$$

where h is heat transfer coefficient of fluid, taken to be 100 W/(m^{2}K) for air, A_s is the area of surface where heat flux goes through, $T_{(t)}$ is body temperature, T_a is ambient temperature. This will help to make the total thermal time constant shorter.

When the structure is downscaled by a factor of X, thermal time constant will reduce by a factor of X^2 while the mechanical time constant decreases by a factor of X, i.e. thermal time constant shrinks faster than the mechanical time constant, according to equation (3.4-7) and (3.6-2). Therefore, by reducing the dimension to a certain level, thermal time constant will be eventually smaller than the mechanical one. For example, when using the nickel paddle parameters in section 3.3 and Table 3.5-1, its mechanical time constant of the translational mode is calculated to be 1.3×10^{-5}s while the thermal time constant is 0.0688s. Therefore, the downscaling factor X is at least 5000 to achieve the full deflection and recovery.

However, making the structure too small is not ideal for remote optical operations, as the surface area for reflection will not be sufficiently large. Most of the micro mirrors reported in the literature have the size of about 100 to 500 μm in width and length but only several microns in thickness (Hedley et al. 2004, Vasquez & Judy 2007, Lee & Park 2010, Bircher et al. 2013). Therefore, attempts have been made to calculate the time constants of several mirrors in the similar range of

size in order to find the structure dimensions that make the thermal time constant smaller than the mechanical one. The results are shown in Table 3.6-1.

It can be seen from Table 3.6-1 that the thermal constants of thin mirrors are still at least one order of magnitude larger than their mechanical time constant, which makes the full deflection vibration very difficult. Actually, structures can be thermally driven into much higher frequency than the operational frequency limited by its thermal time constant, providing the resonator does not have to cool off to the bulk temperature (Sehr et al. 2002, Rahafrooz et al. 2010). The high-frequency vibration is built on top of a static elevated temperature, as shown in Figure 3.6-3, although the temperature variation is smaller than that of a full-deflection resonance. Therefore thermal time constant 10x faster than mechanical time constant is not taken as the absolute critical criterion of this design. However, the slower the thermal cycling time is, the smaller the temperature fluctuation will be, leading to a smaller deflection in the structure. The limit of the thermal time constant depends on the resolution of the sensor detecting the paddle movement. Normally, it needs to be kept within 2~3 orders of magnitude with the mechanical time constant to allow an appreciable actuated deflection, which is the case for all the paddles in Table 3.6-1.

Table 3.6-1 Mechanical and thermal time constant calculation of several micro mirror paddles

Paddle Number	1	2	3	4	5	6
Mirror size (μm x μm)	500x500	100x100	100x100	100x100	100x100	100x100
Mirror thickness (μm)	5	5	1	1	1	1
Supporting beam length (μm)	100	100	100	50	50	50
Supporting beam width (μm)	20	20	20	20	40	40
Material	silicon	Silicon	silicon	silicon	silicon	nickel
Translational Mechanical time constant (s)	1.3e-5	2.6e-6	1.3e-5	4.7e-6	3.3e-6	5.0e-6
Thermal time constant (s)	6.3e-3	2.5e-4	2.5e-4	1.3e-4	6.2e-5	2.7e-4

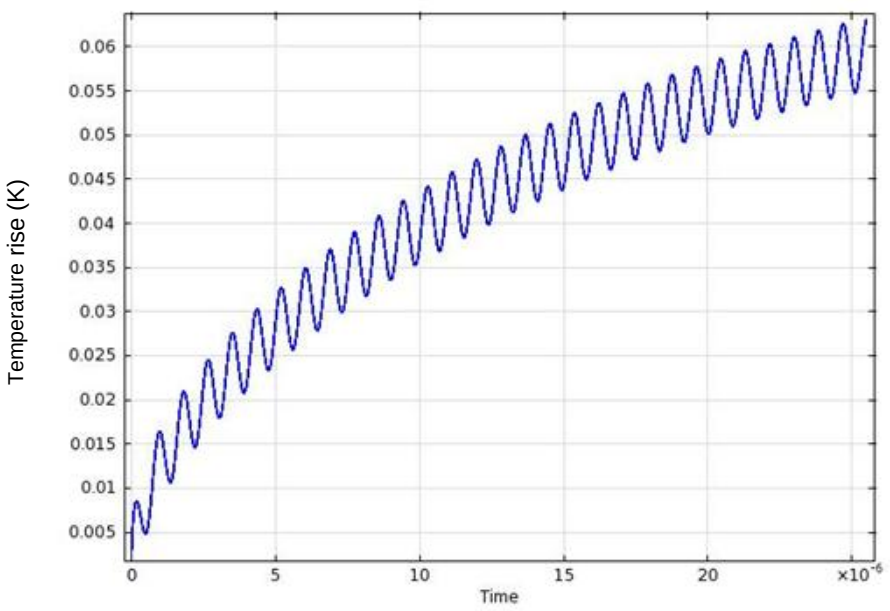

Figure 3.6-3 Time response of the temperature of a beam being thermally actuated at a higher frequency than the operational frequency

In the next section, temperature rise, equivalent force and deflection amplitude introduced by photothermal effect will be calculated in order to be applied to the system dynamic model in the later section.

3.7 Thermal analysis

To calculate the temperature rise and thermal expansion caused by the photothermal effect in the paddle structure, three modelling methods with different complexity are used, which are discussed in the first three subsections. Then the thermal stress induced amplitude and equivalent force are calculated and compared. Radiation heat loss is neglected in the discussion for simplification.

3.7.1 Heat escaping from a lumped thermal mass model

Assuming an optical power is applied on the paddle which is considered as a lumped thermal mass, heat dissipates through two supporting beams. The lumped parameter heat balance equation is

$$Q = C_{th}\,\frac{d\Delta T}{\mathrm{dt}} + G_{th}\Delta T \qquad \textbf{(3.7-1)}$$

where Q is the absorbed optical power, C_{th} is thermal capacity, ΔT is the paddle temperature relative to ambient, G_{th} is thermal conductance of the supporting beams. It is assumed that the light spot is covering the paddle top surface only so that heat input is only through the paddle.

The temperature rise of the paddle is solved to be

$$\Delta T = \frac{Q}{G_{th}}\left(1 - e^{\frac{-t}{\tau}}\right) \qquad \textbf{(3.7-2)}$$

where τ is the thermal time constant defined by C_{th}/G_{th}.

If the incident optical power is modulated to have an amplitude of Q_0 with an angular frequency of ω, the solution to equation (3.7-1) is (Kruse & Skatrud 1997)

$$\Delta T_{\omega} = \frac{Q_0}{G_{th}(1 + \omega^2\tau^2)^{1/2}} \qquad \textbf{(3.7-3)}$$

The temperature of the supporting beam is assumed to be decreasing linearly and the temperature of both ends of the beams is the ambient temperature. The temperature distribution of a lumped thermal mass model is shown in Figure 3.7-1.

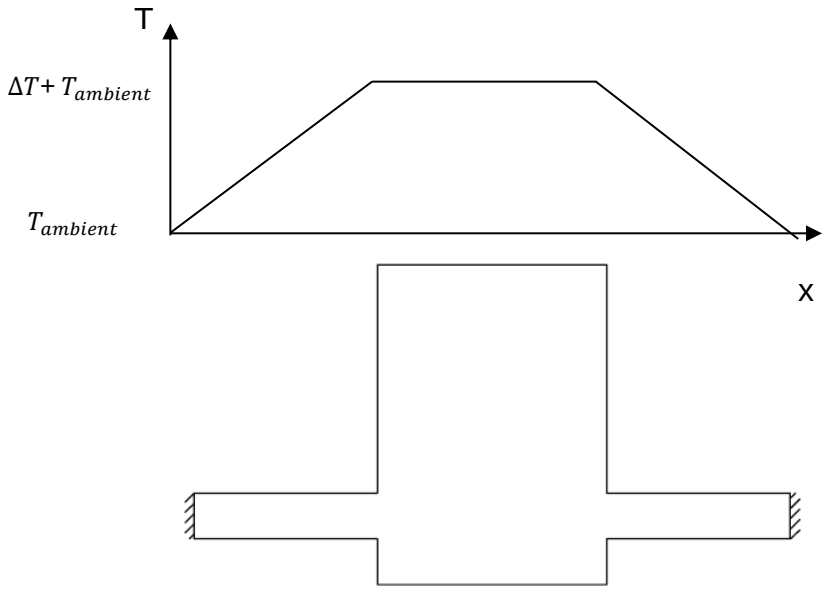

Figure 3.7-1 Schematic of the temperature distribution on a lumped thermal mass paddle model

Hence the thermal expansion along the beams is

$$\delta_{lump} = \alpha \Delta T_{\omega}(b_p + L_T) = \frac{\alpha Q_0 (b_p + L_T)}{G_{th}(1 + \omega^2 \tau^2)^{1/2}} \quad \text{(3.7-4)}$$

where b_p is the width of the paddle and L_T is the length of one supporting beam.

3.7.2 1-D model with heat transferring from top surface to the bottom

With optical power intensity of $\mathrm{I}_{in} = \mathrm{I}_0(1 + \cos(\omega t))/2$ applied on the top surface, one-dimension heat flow Φ in the thickness direction z is given as (Salazar 2006),

$$\frac{\partial^2 \phi}{\partial z^2} - \frac{\rho C_p}{K}\frac{\partial \phi}{\partial t} = \frac{I_{in}}{K} \quad \text{(3.7-5)}$$

Temperature relative to the ambient temperature as a function of depth and time is (Fatah 1992),

$$\Delta T(z,t) = \frac{\mu I_{abs}}{4K} exp\left(\frac{-z}{\mu}\right)\left[\cos\left(\omega t - \frac{z}{\mu}\right) + \sin\left(\omega t - \frac{z}{\mu}\right)\right] \quad \text{(3.7-6)}$$

where I_{abs} is the absorbed optical power intensity.

At the top surface where z=0, the temperature rise is

$$\Delta T(0,t) = \frac{\sqrt{2}\mu I_{abs}}{4K}\sin\left(\omega t + \frac{\pi}{4}\right) \quad \text{(3.7-7)}$$

For a thermally thin structure, temperature in the structure is uniformly equal to $T(0,t)$, therefore, axial expansion is

$$\delta(t) = \alpha \int_0^L \Delta T(0,t)\,\mathrm{dx} = \alpha L \frac{\sqrt{2}\mu I_{abs}}{4K} \sin\left(\omega t + \frac{\pi}{4}\right) \quad \text{(3.7-8)}$$

where δ is the total linear expansion in the axial direction at the time of t, α is the coefficient of linear expansion. The amplitude of thermal expansion is

$$\delta_0 = \alpha L \frac{\sqrt{2}\mu I_{abs}}{4K} \quad \text{(3.7-9)}$$

For a thermally thick structure, temperature varies across its thickness which causes a bending moment to be produced. The thermal expansion in its top thin layer is similar to that of the thermally thin structure. Considering a fixed-fixed beam affected by a modulated bending moment, when stress in the top surface is $E\delta_0/L$, the amplitude of the bending moment is simplified to be

$$M = \frac{2E\delta_0 I}{hL} = \frac{\sqrt{2}\mu I_{abs} EI\alpha}{2Kh} \quad \text{(3.7-10)}$$

3.7.3 Finite Difference Method (FDM)

In the previous discussions, we have assumed that heat is only transferring in one direction, either from the thermal mass to supporting beams (lumped mass model) or from the top surface to the bottom (1-D model). These are however not practically possible to occur in real structures. A more comprehensive 2-D model is used to analyse the temperature distribution for a thermally thin structure which

has a uniform temperature profile through its thickness. The finite difference method (FDM) is used to find the numerical solutions of the 2-D model.

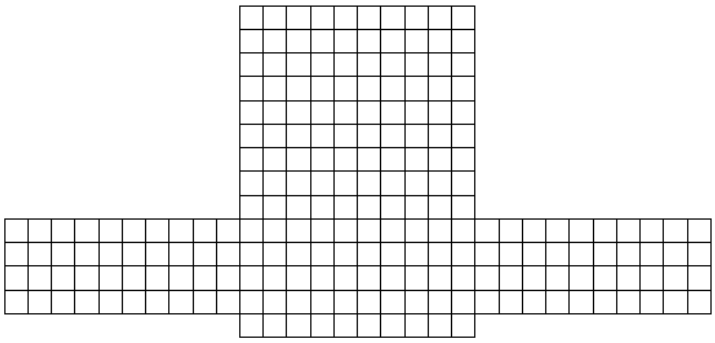

Figure 3.7-2 Schematic of the paddle being located on a grid for FDM. The grid distribution is the same as that used in the following calculation.

FDM is a primary approach for numerically solving partial differential equations. In FDM, the 2-D paddle structure is put on a grid (Figure 3.7-2) and the intersection points of grid lines are nodes, the temperature of which is solved iteratively. The intervals in X and Y directions are Δx and Δy respectively.

Thermal energy balance at one node (m,n), as shown in Figure 3.7-3, can be express as (Dawit 2010)

$$Q^{store} = Q^{heating} + Q^{cond} + Q^{conv} \qquad \textbf{(3.7-11)}$$

where Q^{store} is the net change of energy

$Q^{heating}$ is the absorbed laser heat at the node

Q^{cond} is the heat conduction between node m,n and its adjacent nodes

Q^{conv} is the heat flow due to convection

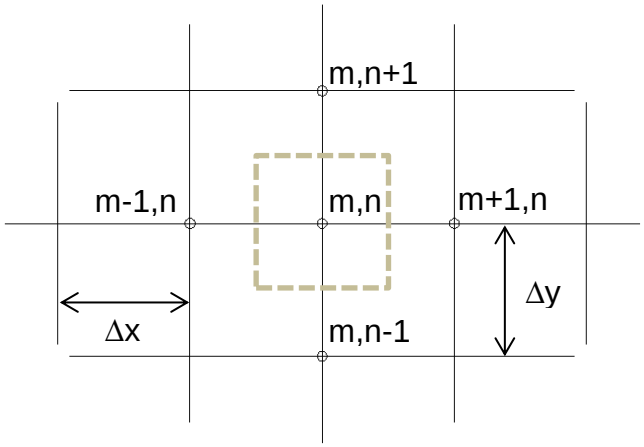

Figure 3.7-3 Node m,n and its adjacent nodes

In a more specific form, the energy balance equation can be written as

$$Q_{m,n}^{store} = \mathrm{Q}_{m,n}^{heating} + Q_{m-1,n}^{cond} + Q_{m+1,n}^{cond} + Q_{m,n+1}^{cond} + Q_{m,n-1}^{cond} + Q_{m,n}^{conv} \qquad \textbf{(3.7-12)}$$

According to Fourier's Law

$$\vec{q} = -K\frac{dT}{dx} \qquad \textbf{(3.7-13)}$$

where $\vec{q}$ is the local heat flux (W/m^2). Hence equation (3.7-12) becomes

$$\begin{aligned} &\rho c \Delta x \Delta y \Delta z \left(\frac{T_{m,n}^{i+1} - T_{m,n}^{i}}{\Delta t}\right) \\ &= q_{m,n}^{laser} \Delta x \Delta y \Delta z + K^{left} \Delta y \Delta z \left(\frac{T_{m-1,n}^{i} - T_{m,n}^{i}}{\Delta x}\right) \\ &+ K^{right} \Delta y \Delta z \left(\frac{T_{m+1,n}^{i} - T_{m,n}^{i}}{\Delta x}\right) + K^{up} \Delta x \Delta z \left(\frac{T_{m,n+1}^{i} - T_{m,n}^{i}}{\Delta y}\right) \\ &+ K^{down} \Delta x \Delta z \left(\frac{T_{m,n-1}^{i} - T_{m,n}^{i}}{\Delta y}\right) + h_{m,n}(T_{amb} - T_{m,n}^{i}) \Delta x \Delta y \end{aligned} \qquad \textbf{(3.7-14)}$$

where the superscripts of local temperature $T_{x,y}$ denote the time increment. $q_{m,n}^{laser}$ is the input heat source density. The superscripts of thermal conductivity K indicate the directions that the heat flux is from or towards. Δz is the node thickness. Δt is the time increment. $h_{m,n}$ is the heat transfer coefficient of air.

Therefore the temperature at t_{i+1} is derived as (Elbuken et al. 2008)

$$T_{m,n}^{i+1} = T_{m,n}^{i} + q_{m,n}^{laser}\frac{\Delta t}{\rho c} + \frac{K^{left}(T_{m-1,n}^{i} - T_{m,n}^{i})\Delta t}{\rho c(\Delta x)^2} + \frac{K^{right}(T_{m+1,n}^{i} - T_{m,n}^{i})\Delta t}{\rho c(\Delta x)^2} + \frac{K^{up}(T_{m,n+1}^{i} - T_{m,n}^{i})\Delta t}{\rho c(\Delta y)^2} + \frac{K^{down}(T_{m,n-1}^{i} - T_{m,n}^{i})\Delta t}{\rho c(\Delta y)^2} + \frac{h_{m,n}(T_{amb} - T_{m,n}^{i})\Delta t}{\rho c \Delta z} \quad \textbf{(3.7-15)}$$

The maximum time increment (Δt) for a stable solution is limited by the mesh Fourier number (Powell 2002)

$$Fo_M = \frac{K\Delta t}{\rho C_p(\Delta x)^2} \quad \textbf{(3.7-16)}$$

For 2-D modelling, the stability criterion is $Fo_M \leq \frac{1}{6}$. Using the material properties of silicon in Table 3.5-1, set Δx to be 10 μm, Δt is calculated to be 1.8e-7s.

Microsoft Excel has been used to perform the FDM iteration (Lobaugh 2014). Although it has the drawback that it greatly simplifies the system and it is only able to deal with rectangular shape domain, Excel can visually illustrate the basic concepts of FDM and provide a flexible way of solving it.

After matching different node equations with different boundary node types and ignoring the temperature dependence of K, the temperature distribution of the structure is solved in Excel with macro programming (see Appendix I). The paddle dimensions used in FDM has been revised according to the discussed results in section 3.4 to 3.7 in order to get a stress sensitive paddle mirror with a short thermal time constant and a large thermal expansion. Referring to the denotation in Figure 3.4-2, it is set that $h = h_P = 10\mu\text{m}$, $w_T = 40\mu\text{m}$, L_T is 100μm, b_P is 100μm, L_P is 140μm, l_2/l_1=11:3. Also $\Delta x = \Delta y = \Delta z = 10\mu\text{m}$ and the ambient temperature is 20°C. The result of FDM solution after 0.018s (100k time steps) is shown in Figure 3.7-4. It can be seen that the warmer the color is, the higher the node temperature is. The maximum temperature rise is about 0.0032K.

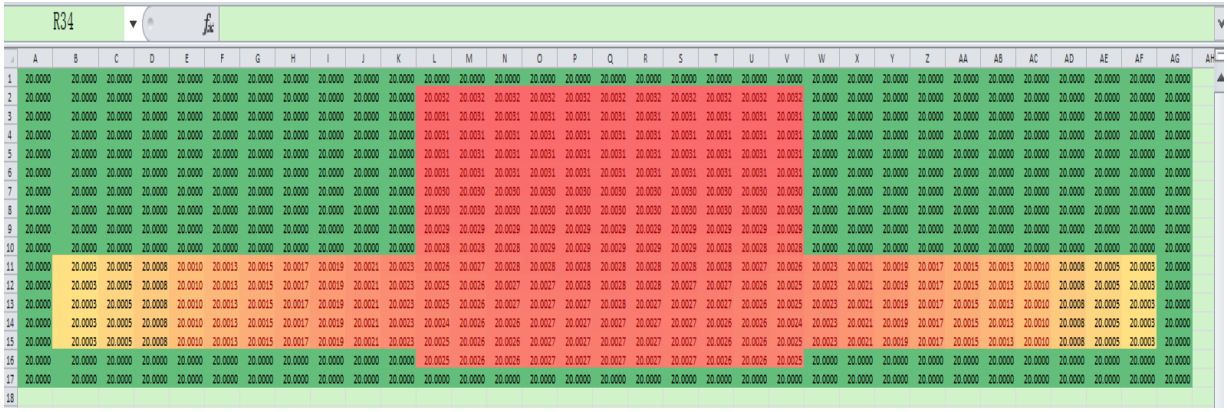

Figure 3.7-4 Result of FDM in Excel. The colour temperature shows the temperature difference in the structure

The thermal expansion is the integration of local expansion of each node along the axis. Hence the axial thermal expansion of this paddle δ_{lump} =2.3e-12m, given that the input is a 2mW laser spot with 2mm radius.

3.7.4 Thermal stress induced equivalent force and deflection amplitude

The amplitude (Fatah 1992) of the midspan deflection caused by a thermal expansion of a doubly clamped beam structure is given by,

$$A = \sqrt{\frac{3L\delta_0}{8}} \qquad \textbf{(3.7-17)}$$

where L is the total length of the structure. This is a simplified equation which gives a similar result as the deflection equation given by Usmani et al.(2001). The limitation of applying this to the paddle model is that the original equation is for beam structure analysis. The paddle structure is a variation of a doubly clamped beam but with a widened middle section. The paddle will introduce more stiffness to the structure therefore less deflection should be expected than the calculated result.

Equivalent bending force applied on the midspan to cause a deflection of A is (Fatah 1992)

$$F = 192\frac{A(EI)}{L^3} \qquad \textbf{(3.7-18)}$$

In the lumped thermal mass model, by substituting equation (3.7-4) into equation (3.7-17), amplitude of deflection is derived as

$$A_{lump} = \sqrt{\frac{3L\alpha Q_0\left(b_p + L_T\right)}{8G_{th}(1+\omega^2\tau^2)^{1/2}}} \qquad \textbf{(3.7-19)}$$

And the equivalent force to produce that deflection is

$$F_{lump} = 192\frac{(EI)}{L^3}\sqrt{\frac{3L\alpha Q_0\left(b_p + L_T\right)}{8G_{th}(1+\omega^2\tau^2)^{1/2}}} \qquad \textbf{(3.7-20)}$$

In the 1-D heat transfer model, for a thermally thin paddle, the amplitude of deflection is

$$A_{thin} = \sqrt{\frac{3\sqrt{2}\alpha L^2 \mu I_{abs}}{32K}} \qquad \textbf{(3.7-21)}$$

And the equivalent force to produce that deflection is

$$F_{thin} = \frac{48EI}{L^2}\sqrt{\frac{3\sqrt{2}\alpha\mu I_{abs}}{2K}} \qquad \textbf{(3.7-22)}$$

For a thermally thick structure, the deflection amplitude is calculated as the deflection of a simply supported beam with a single moment, as in equation (3.7-10), applied at the support end,

Hence $$A_{thick} = \frac{ML^2}{16EI} = \frac{\sqrt{2}\mu I_{abs}\alpha L^2}{32Kh} \qquad \textbf{(3.7-23)}$$

Similarly, according to equation (3.7-18)

$$F_{thick} = \frac{6\sqrt{2}EI\alpha\mu I_{abs}}{hKL} \qquad \textbf{(3.7-24)}$$

In the FDM model, the deflection caused by thermal expansion and its equivalent bending force can also be given by substituting the FDM result into equation (3.7-17) and (3.7-18).

3.7.5 Thermal modelling result and discussion

Assuming a 5mW laser with 2mm radius spot is applied on the paddle with the dimension used in FDM analysis, discussed in section 3.7.3, about 159W/m^2 of optical power is absorbed by the paddle top surface (an absorption rate of 40% is assumed for a gold coated surface). Since the power intensity entering the system is varying with actuation frequency, 100kHz is chosen to evaluate the deflection amplitude A and equivalent force F in order to get a closer value but stay away from resonance (the translational mode resonant frequency of the paddle is 928 kHz. It should be noted that the translational frequency of the paddle is different from the one mentioned in section 3.4 due to a change of the geometry to a smaller paddle for better performance). With 100 kHz optical actuation, thermal diffusion length μ of silicon structure is calculated to be 17.8μm, mentioned in equation (3.5-1).

With the parameters above, the results of the deflection amplitude and the equivalent force for different models are shown in Table 3.7-1.

Table 3.7-1 Result for thermal models

Model	Lumped thermal mass	1-D heat transfer		2-D FDM
		Thin	Thick	
Temperature rise (K)	2.4e-5	6.1e-6	_	3e-3 (max)
Total expansion (m)	2.0e-14	7.6e-15	_	2.3e-12
Deflection amplitude (m)	1.5e-9	9.3e-10	2.9e-14	1.6e-8
Equivalent force (N)	4.7e-6	2.9e-6	8.9e-11	5.0e-5

The table shows that two situations are calculated in the 1-D heat transfer model: 'thin' for the thermally thin structure and 'thick' for thermally thick structure. The thickness of 10 μm are used for both situation, just to characterize the difference between the two hypothesizes.

As illustrated in the table, the lumped thermal mass model and the 1-D model show results very different to that of the 2-D FDM model. The lumped thermal model provides a great simplification and it is calculating the temperature fluctuation responding to the ac portion of the oscillating power input (Sampathkumar et al. 2006). There is also an average temperature rise in the structure based on the dc portion of the input power. When the frequency of the input power is very low ($\omega\tau \ll 1$), $\Delta T = \frac{Q}{G_{th}} = 0.0027\mathrm{K}$, which is much closer to the maximum temperature rise in the FDM result. The 1-D model is more suitable for relatively thicker structure where the heat transfer in vertical direction is more significant, as the 1-D model is considering the heat transfer from top to the

bottom only but ignoring the transfer from paddle to the surrounding substrate. The FDM gives a more reasonable result for a stationary power input as it didn't take the oscillation of the laser power into account. But it is capable to calculate the oscillating power situation when the input power is set to be varying with time.

3.8 COMSOL Multiphysics simulation

As a further check of the analytical modelling, COMSOL Multiphysics, which is a commercial finite element method (FEM) simulation software, is used to test the deflection amplitude for the paddle design, as mentioned in Table 3.7-1. COMSOL is chosen here because it is particularly good at solving problems with multiple physical fields, which suits the case of this model that involves photothermal and solid mechanics problems. The model constraints are shown in Figure 3.8-1. With the dimensions and parameters mentioned in the last section, a sinusoidal light power is applied on the top surface of a silicon paddle to actuate it into off-resonance vibration meanwhile both end faces of the beam are set to be fixed and have a constant room temperature of 293.15K. Default tetrahedral mesh is used.

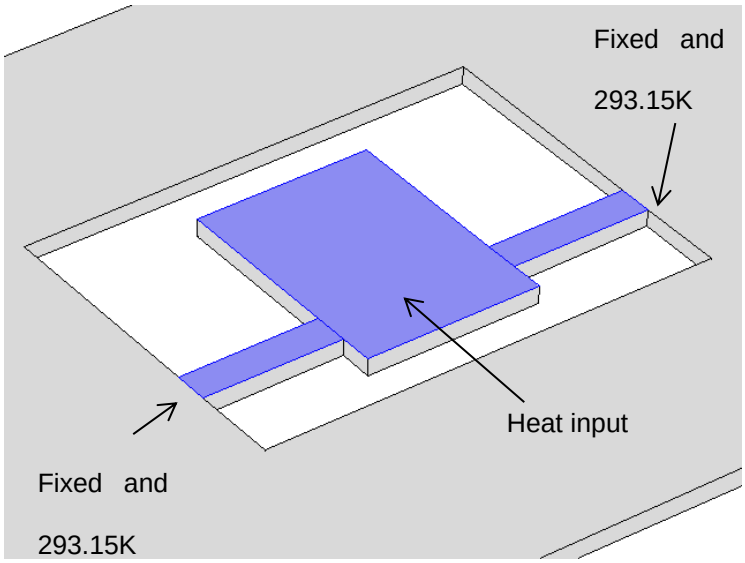

Figure 3.8-1 Model constraints

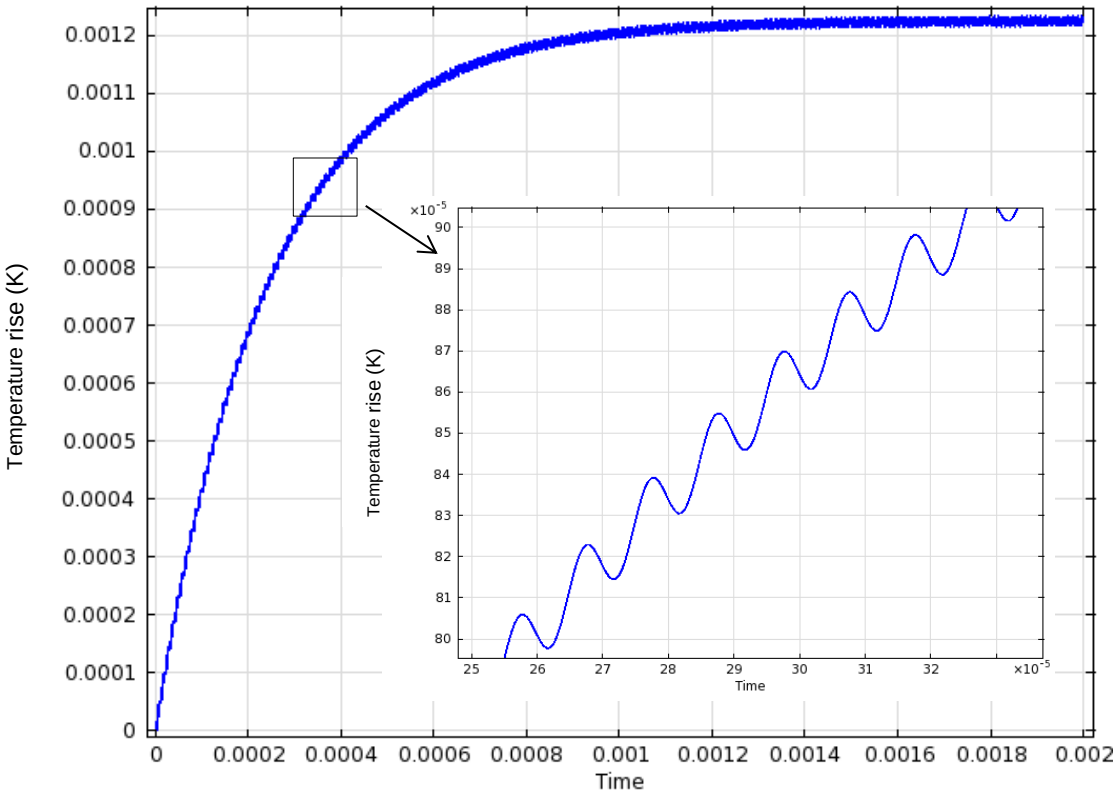

Figure 3.8-2 Temperature rise at the midspan of the structure. The inset shows a closer view of the temperature fluctuation, the amplitude of which is measured to be 1.6e-5 K.

For the 10μm thick structure, 159W/m^2 and 100 kHz optical power is applied. The temperature rise is shown in Figure 3.8-2. The average temperature rise is 0.00122K which is about half of that of the FDM model. This is coincident with the steady state temperature rise caused by the average value of input power. The temperature fluctuation is measured to be 1.6e-5K, which is comparable with the result of the lumped thermal mass model.

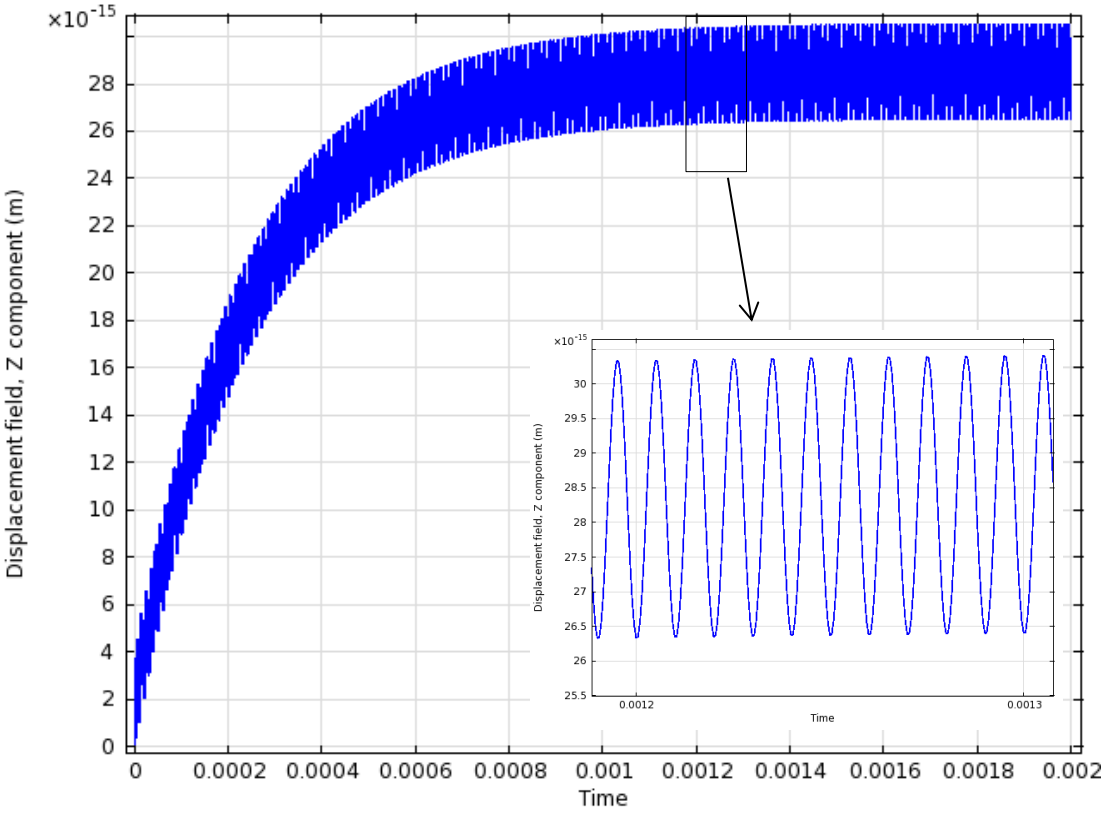

Figure 3.8-3 Time dependent midspan displacement of 10μm structure

The time dependent vertical displacement of the fixed-fixed beam is shown in Figure 3.8-3. The paddle does not produce any deflection because the displacement shown here is around 2.8e-14m which is much smaller than the

analytical result. The reason is that for a doubly fixed structure, COMSOL only calculates the vertical displacement produced by the volumetric thermal expansion while no buckling or bending caused by axial thermal expansion has been taken into account due to the perfect symmetry of the beam cross section and its fixed constraints (Figure 3.8-4). Once the fixed constraints are changed to one of the edges, deflection of the paddle occurs (shown in Figure 3.8-5).

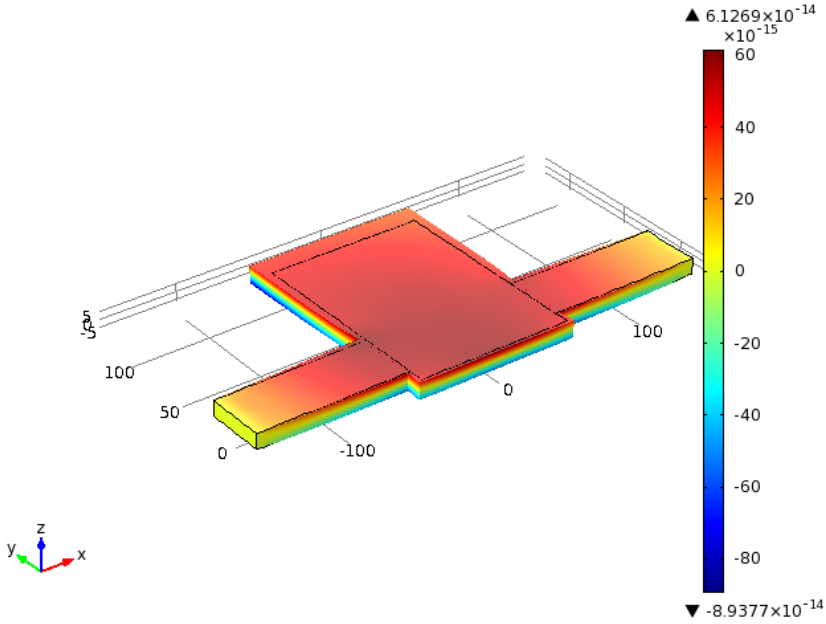

Figure 3.8-4 Stationary result of vertical displacement when both end faces are fixed. No deflection is shown. The color indicates the displacement caused by volumetric thermal expansion

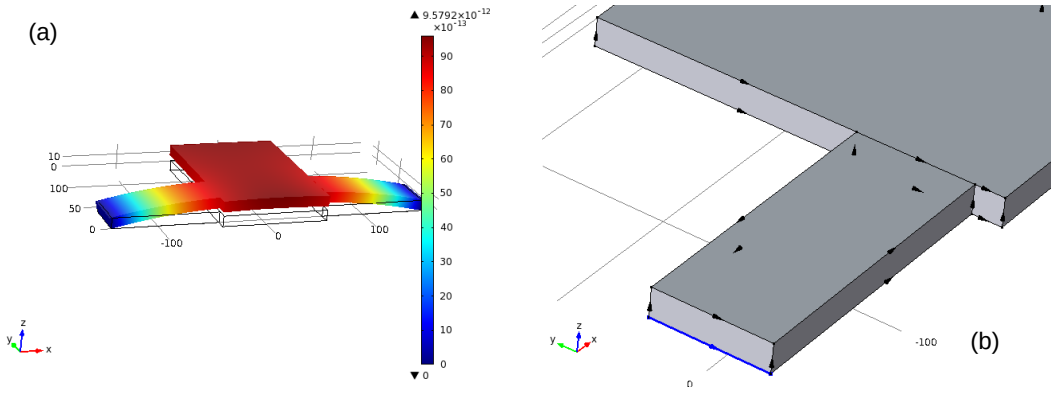

Figure 3.8-5 Stationary vertical deflection occurs (a) when only one edge of each end face is fixed (b).

Driving the edge fixed paddle with the same power at 100 kHz gives the result shown in Figure 3.8-6. It can be seen that the vertical displacement is much larger than that in Figure 3.8-3. Although the enlarged deflection is a result of breaking the symmetry of the COMSOL model which triggers the out-of-plane movement, using line constraint instead of area constraint can make the deflection greater. This should be considered when comparing the simulation results with the analytical ones.

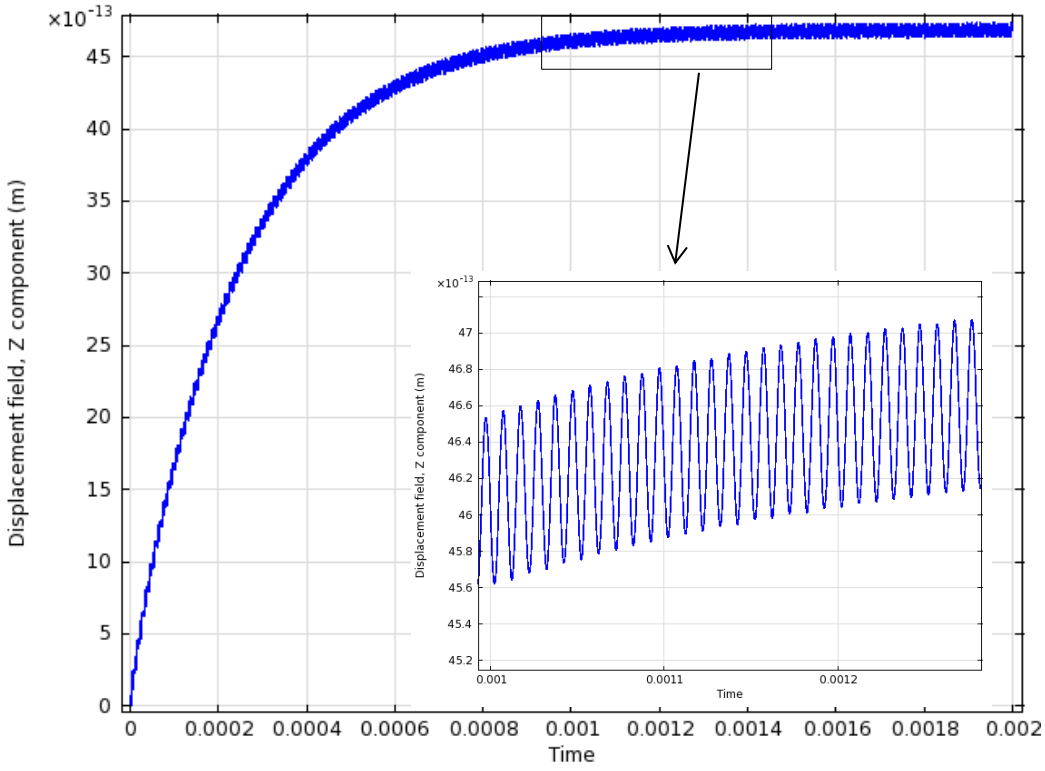

Figure 3.8-6 Midspan vertical deflection when the paddle is driven at 100 kHz

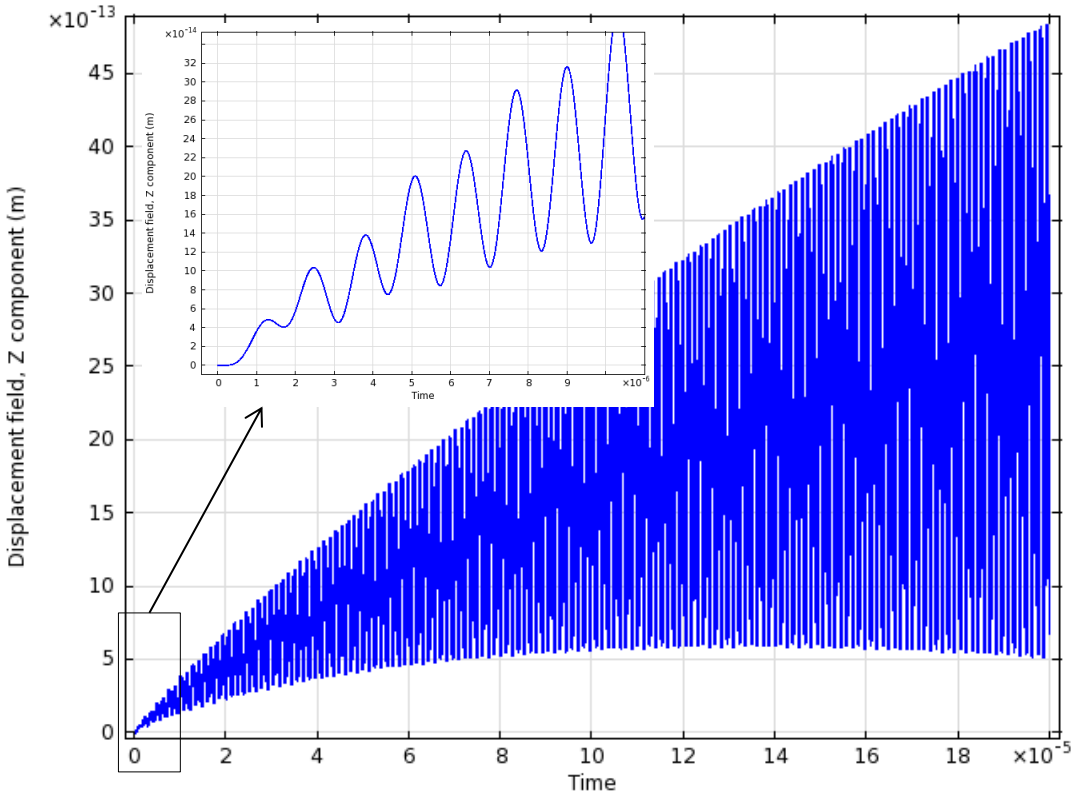

Figure 3.8-7 Midspan vertical deflection when the paddle is driven at translational resonant frequency

When increasing the driving frequency to the translational resonant frequency (767 kHz due to the change of constraints), the response of midspan vertical deflection is shown in Figure 3.8-7. It can be seen that the paddle resonance is achieved.

In the COMSOL simulation, a 3-D model is used to verify the analytical results. Temperature distribution and time dependent profile matches well with the FDM and lumped thermal mass model while the midspan deflection doesn't match with the analytical result at low-frequency driving. The reason has been explained that it is the perfectly symmetrical structure and strictly fixed constraints in COMSOL

preventing any out-of-plain motion caused by temperature rise. Once the fixed constraint is changed to one of the edges, larger deflection is produced. Although the stationary deflection shown in Figure 3.8-5a is still smaller than the analytical results in Table 3.7-1, since those results are derived from equation (3.7-17) which has been experimentally proved (Fatah 1992), the lumped thermal mass model and the FDM model are considered to be true. Furthermore, COMSOL shows that the paddle is optically actuated into resonance when driven at its translational resonant frequency.

3.9 Damping of micro resonators

For micro resonators, damping can be caused by air drag force, internal material energy lost or acoustic energy radiation. Normally, structure of micro size performing in the air has a quality factor about 100~1000 (Kiracofe et al. 2011,Mahmoodi & Anthony 2014). Hence an estimated Q-factor of 300 is used to calculate the coefficient of damping.

For a spring-damp system with small damping (Bao 2005)

$$Q = \frac{1}{2\zeta} \qquad \textbf{(3.9-1)}$$

Translational damping ratio is

$$\zeta_b = \frac{c}{2\sqrt{mk}} \qquad \textbf{(3.9-2)}$$

where c is the translational coefficient of damping force, k is the translational spring constant.

The torsional damping ratio is given by a similar equation but replacing the mass of the paddle with its moment of inertia and replacing the translational spring constant with the torsional one. The torsional damping ratio is

$$\zeta_t = \frac{c_t}{2\sqrt{J_p k_t}} \qquad \text{(3.9-3)}$$

where c_t is the torsional coefficient of damping force, k_t is the torsional spring constant and J_p is the moment of inertia of the paddle, given in equation (3.4-5).

By substituting the parameters of material in Table 3.5-1 and the dimensions of the paddle structure in section 3.7.3, the coefficients of damping force can be calculated, which are required in the dynamic modelling and given in Table 3.10-1 in the following section.

3.10 Dynamic modelling of system actuation

The paddle vibration can be modeled as an inverted pendulum on cart system, but taken into the horizontal position, as shown in Figure 3.10-1. The supporting beams can be treated as a cart with a mass of M, moving vertically and restrained by spring k and damping c. The paddle is treated as a pendulum sitting on the cart, with a mass of m, length of L, the distance between centers of the two mass of l, torsional spring of k_t and torsional damping of c_t.

All the parameters above are calculated based on the silicon structure dimension used in the FDM analysis in Section 3.7.3 and the parameter values are listed in Table 3.10-1. The translational spring constant k and torsional spring constant k_t are obtained from equation (3.4-6) and (3.4-1) respectively. As discussed in the last section, a Q factor of 300 is chosen as an estimated value. Therefore the translational and torsional damping coefficient c and c_t can be calculated from equation (3.9-2) and (3.9-3). A photo-thermally induced bending force $F(t) = 1/2\ (F_0 + F_0 \sin\omega t)$ is applied on the mass M, where F_0 is the equivalent force derived in equation(3.7-20), at the translational resonant frequency.

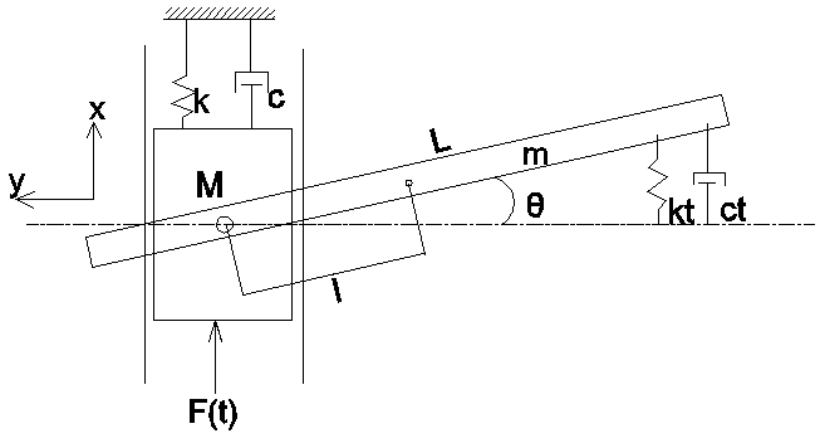

Figure 3.10-1 Schematic of a pendulum dynamic model

Table 3.10-1 Parameters used in dynamic modelling

Parameter		Parameter	
L	140 [μm]	k_t	1.16e-5 [N*m/rad]
l	40 [μm]	c_t	1.08e-14 [N*m*s/rad]
k	1.05e4 [N/m]	Q	300
c	2.33e-6 [N*s/m]	F_0	1.56e-6 [N]

To solve the dynamics problem of this system, Newton's mechanics is not convenient. Therefore, Lagrangian dynamics is employed to simplify the problem solving (Klinke et al. 2010). It is defined that Lagrangian $\mathcal{L}$ is

$$\mathcal{L} = T - V \qquad \textbf{(3.10-1)}$$

And it satisfies the equation of

$$\frac{\mathrm{d}}{\mathrm{dt}}\left(\frac{\partial \mathcal{L}}{\partial \dot{q}_i}\right) - \frac{\partial \mathcal{L}}{\partial q_i} = Q_i \qquad (i = 1,2 \ldots, n) \qquad \textbf{(3.10-2)}$$

where T and V are the kinetic energy and potential energy of the system respectively, q_i is the generalized coordinates, Q_i is the non-conservative generalized force, n is the number of degree of freedom.

Taking the paddle problem into the Lagrangian equations (3.10-1) (3.10-2), generalized coordinates are assigned as

$$q_1 = x \quad q_2 = \theta \qquad \textbf{(3.10-3)}$$

Non-conservative generalized forces are the forces causing mechanical energy of the system to increase or decrease, such as friction, damping and input force. Therefore, the non-conservative generalized forces are

$$Q_1 = F(t) - c\dot{x}, \qquad Q_{2=} - c_t\dot{\theta} \tag{3.10-4}$$

Dynamic vectors are as following,

For M $\quad \underline{r}_M = x, \quad \dot{\underline{r}}_M = \dot{x}, \quad \ddot{\underline{r}}_M = \ddot{x}$

For m $\quad \underline{r}_m = (x + lsin\theta, -l\cos\theta)$

$$\dot{\underline{r}}_m = (\dot{x} + l\dot{\theta}cos\theta, l\dot{\theta}sin\theta)$$

$$\ddot{\underline{r}}_m = (\ddot{x} + l\ddot{\theta}cos\theta - l\dot{\theta}^2sin\theta, l\ddot{\theta}sin\theta + l\dot{\theta}^2cos\theta)$$

For Lagrangian $\quad \mathcal{L} = T - V$

The kinetic energy of the system T is given by

$$T = T_M + T_m \tag{3.10-5}$$

where the kinetic energy of M is

$$T_M = \frac{1}{2}M\dot{\underline{r}}_M{}^2 = \frac{1}{2}M\dot{x}^2 \tag{3.10-6}$$

and the kinetic energy of m is

$$T_m = \frac{1}{2}m\dot{\underline{r}}_m{}^2 + \frac{1}{2}I\dot{\theta}^2 = \frac{1}{2}m\dot{x}^2 + m\dot{x}l\dot{\theta}\cos\theta + \frac{1}{2}(\mathrm{ml}^2 + I)\dot{\theta}^2 \tag{3.10-7}$$

where the paddle's moment of inertia I is given by

$$I = \frac{1}{12}mL^2 + ml^2 \tag{3.10-8}$$

The potential energy of the system V is given by

$$V = \frac{1}{2}kx^2 + \mathrm{mg}l\sin\theta + \frac{1}{2}k_t\theta^2 + (M+m)gx \qquad \textbf{(3.10-9)}$$

Therefore, the Lagrangian is rewritten as

$$\mathcal{L} = \frac{1}{2}M\dot{x}^2 + \frac{1}{2}m\dot{x}^2 + m\dot{x}l\dot{\theta}\cos\theta + \frac{1}{2}(ml^2 + I)\dot{\theta}^2 - \frac{1}{2}kx^2 - \mathrm{mg}l\sin\theta - \frac{1}{2}k_t\theta^2 - (M+m)gx \qquad \textbf{(3.10-10)}$$

By substituting $\mathcal{L}$ into equation (3.10-2), the equations of motion can be expressed as:

For coordinate x

$$\frac{\partial\mathcal{L}}{\partial x} = -kx - (M+m)g, \qquad \frac{\partial\mathcal{L}}{\partial\dot{x}} = (M+m)\dot{x},$$

$$\frac{\mathrm{d}}{\mathrm{dt}}\left(\frac{\partial\mathcal{L}}{\partial\dot{x}}\right) = (M+m)\ddot{x} + ml\ddot{\theta}cos\theta - ml\dot{\theta}^2sin\theta$$

so $$\frac{\mathrm{d}}{\mathrm{dt}}\left(\frac{\partial\mathcal{L}}{\partial\dot{x}}\right) - \frac{\partial\mathcal{L}}{\partial x} = (M+m)\ddot{x} + ml\ddot{\theta}cos\theta - ml\dot{\theta}^2sin\theta + kx + (M+m)g = Q_1 = F(t) - c\dot{x} \qquad \textbf{(3.10-11)}$$

For coordinate θ

$$\frac{\partial\mathcal{L}}{\partial\theta} = -ml\dot{x}\dot{\theta}sin\theta - mglcos\theta - k_t\theta, \qquad \frac{\partial\mathcal{L}}{\partial\dot{\theta}} = ml\dot{x}cos\theta + (ml^2 + I)\dot{\theta},$$

$$\frac{\mathrm{d}}{\mathrm{dt}}\left(\frac{\partial\mathcal{L}}{\partial\dot{\theta}}\right) = ml\ddot{x}cos\theta - ml\dot{x}\dot{\theta}sin\theta + (ml^2 + I)\ddot{\theta}$$

so $$\frac{\mathrm{d}}{\mathrm{dt}}\left(\frac{\partial\mathcal{L}}{\partial\dot{\theta}}\right) - \frac{\partial\mathcal{L}}{\partial\theta} = ml\ddot{x}cos\theta + (ml^2 + I)\ddot{\theta} + mglcos\theta + k_t\theta = Q_{2=} - c_t\dot{\theta} \qquad \textbf{(3.10-12)}$$

Using MatLab to solve the coupled differential equations (3.10-11) and (3.10-12) (MatLab code in Appendix II), the analytical result of paddle deflection

(x displacement of mass M) and tilt angle (angular displacement of mass m) can be obtained with the parameters listed in Table 3.10-1.

Figure 3.10-2 shows the time dependent system response of the paddle resonator being driven optically. It can be seen that the paddle starts from the horizontal initial position and develops into resonance. However, the tilt angle amplitude is very small (1.5e-6 rad) compared to the aimed (1.7mrad) design specification.

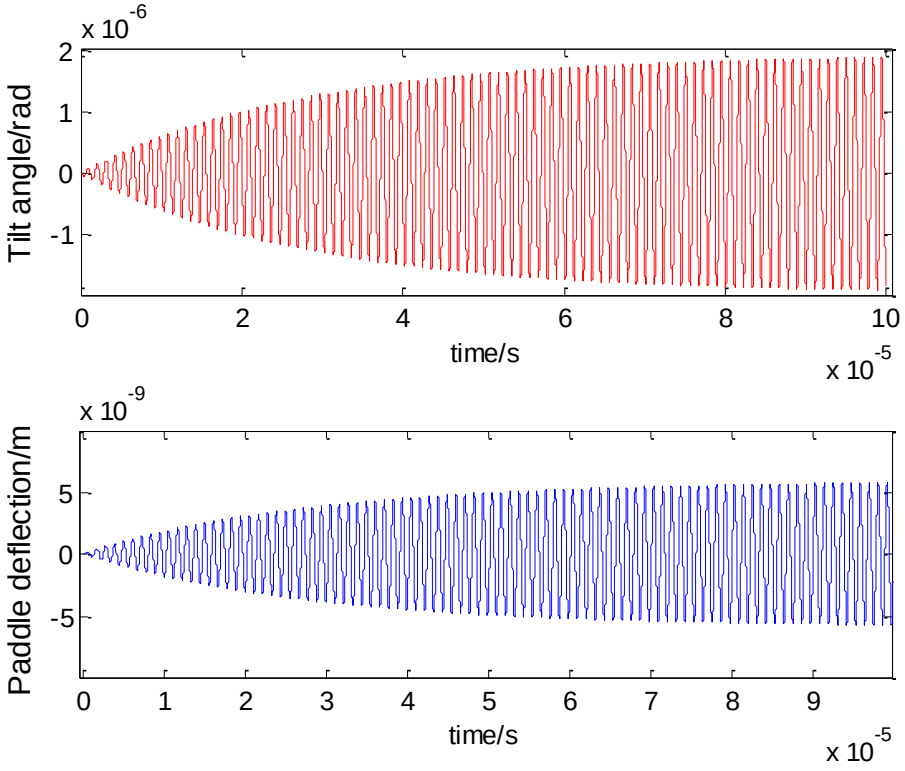

Figure 3.10-2 Time response of the tile angle and paddle deflection of the paddle

Therefore, attempts have been made to optimize the system by adjusting some of the parameters, which is required to decrease the stiffness in order to enlarge paddle deflection A and tilting angle θ ,whilst increase the equivalent driving force by increase the input power intensity. The trends of the results after changing some of the parameters are concluded in Table 3.10-2. '+' and '-' represents the increase and decrease of the results respectively. The result for amplitude A matches with the trend suggested in equation (3.7-19).

Table 3.10-2 Trends of system response with parameter changing

Parameters	θ	A
Reducing thickness	+	+
Increasing supporting beam length	+	+
Increasing paddle length	-	-
Increasing laser intensity	+	+

In order to get a satisfying tilt angle. The dimension and parameters are tuned, as shown in Table 3.10-3. The performance simulated in Matlab is shown in Figure 3.10-3. The paddle can achieve a maximum tilt angle of 1.5 mrad, which is close to the specification.

Table 3.10-3 Tuned parameter for an optically actuated paddle

Paddle length	140[μm]	Supporting beam width	40[μm]
Paddle width	100[μm]	Driving frequency	33.8[kHz] (new translational mode frequency)
Paddle thickness	3[μm]	Excitation laser power	50[mW]
Supporting beam length, one side	400[μm]	Absorption rate (assumed)	40%
Beam thickness	3[μm]	Spot diameter	1[mm]

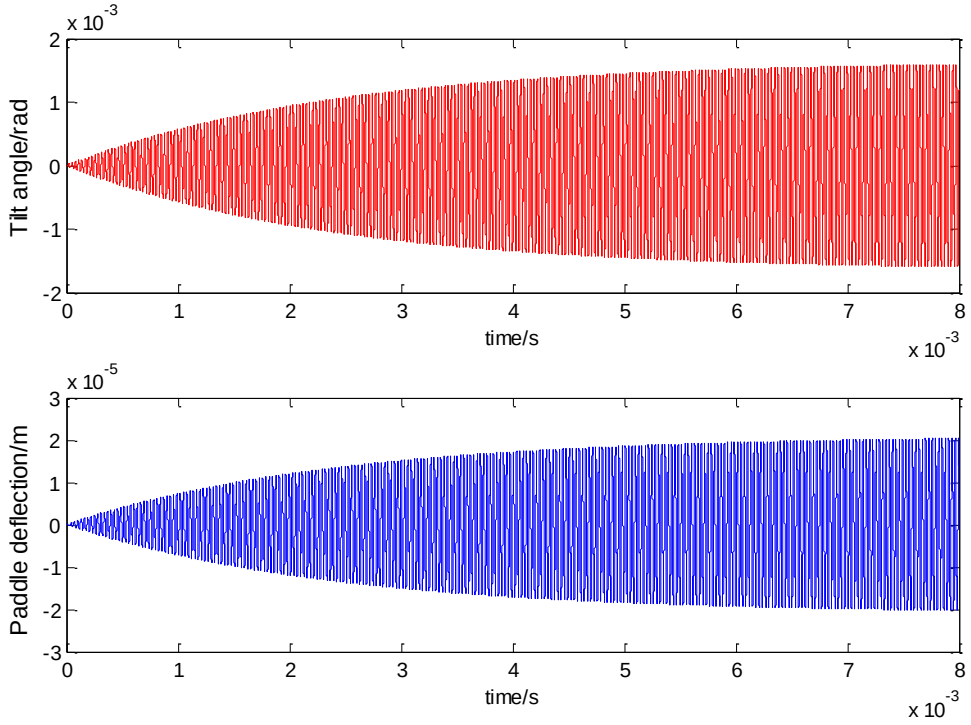

Figure 3.10-3 Time response of the tuned paddle tilt angle and midspan deflection

3.11 Conclusions

In this chapter, a micro paddle resonator actuated by photothermal effect is designed. Resonant frequency change with axial stress is calculated, providing the potential for it to act as a sensor element. The principle of photothermal actuation is explained. The actuation process is mathematically analysed and modeled in COMSOL and MatLab.

Results from analytical work and simulation have shown that a thermally thin paddle working near its translational resonant frequency can facilitate the optical actuation and enhance the axial stress sensitivity. A group of optimized design parameters has been provided in the system actuation modelling to achieve a tilting angle that is aimed in the design specification.

Chapter 4: Optical Interrogation with Micro Corner Cube Retroreflector (CCR) and Sensor System Design

4.1 Introduction

Once the paddle resonator discussed in Chapter 3 is successfully actuated, the sensor system is expected to be interrogated optically. Since the aimed working distance for this system is relatively long (3m), any small change in the orientation of incident light will make a great difference to the direction of the reflected signal. This makes the positioning of a signal receiver to be extremely difficult. Therefore, a micro CCR system is employed to control the direction of the return signal after reflection from the sensor. With its regulation, the return signal can be located easily and, more importantly, can be observed at the same location as the laser sources. It allows the interrogation system to be compact and easy for alignment.

In this chapter, firstly the working principle of an optical interrogation system with a micro CCR is introduced. Secondly, the specifications and optical behaviors of the micro CCR are discussed. Finally, the design setup of the sensor actuation and interrogation system is presented.

4.2 Principle of the interrogation system

There are mainly two methods of involving a micro CCR structure into the paddle resonator interrogation system. One is to detect the frequency of the periodical appearance of the retroreflection. The other one is to detect the change in the separation of the reflected beams. Details of the two methods are introduced as follow.

4.2.1 Via detecting the retroreflection

As mentioned in the previous chapters, the retroreflection of a micro CCR only occurs when the three mirrors are perfectly perpendicular to each other. As one of the mirrors is made as a tilting mirror, the appearance frequency of the retroreflection is the same as the frequency of the mirror oscillation. The former can be measured by detecting the light reflection at the same position as the interrogation laser source.

This method is widely used in free space communication. Zhou et al.(2002) demonstrated a micro CCR communicator working over a distance of 180m (Figure 4.2-1). The CCR is illuminated by an interrogator. When the angular displacement of one CCR mirror is electrically driven to be on and off states by a modulated signal (Figure 4.2-1(1)), the photocurrent detected at the interrogator changes accordingly but in the opposite state (Figure 4.2-1(2)). Lee & Park (2010)

used a silicon photodiode to detect the reflected signal of a He-Ne laser with the same working principle. A working distance of 50cm is achieved.

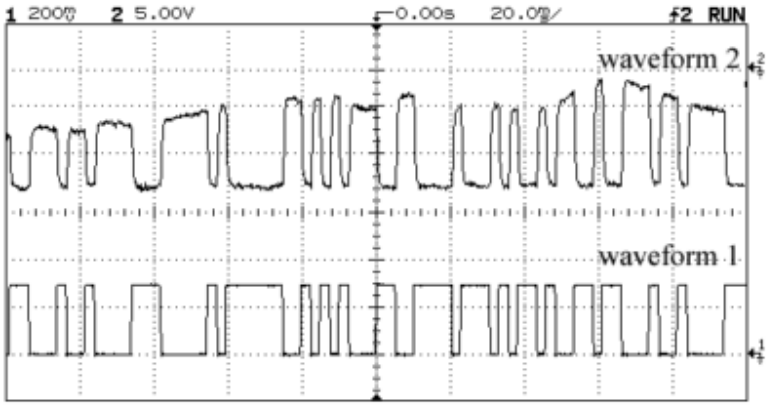

Figure 4.2-1 Free-space communication (Zhou et al. 2002)**. (1): CCR driving signal. (2): Detected photocurrent**

When interrogating the resonant sensor with this principle, the analog signal reflecting the vibration amplitude is not available as the photodetector only produced a digital signal showing the on and off states. Therefore, the phase difference is used to track the change of sensors resonant frequency. Once a resonance frequency is reached, the phase difference should be $-\pi/2$.

4.2.2 Via detecting the separation of split beams

The interrogation laser beam is not focused in the remote detector, which means the spot size is comparable or larger than the size of the micro CCR. Hence light incidences occur on three mirrors simultaneously. After being reflected successively on the three mirrors of a CCR, six reflection paths are formed

depending on the order of reflection mirrors (Vasquez & Judy 2007). If one of the CCR mirrors is misaligned, the reflected beams are split into two groups of three parallel beams, directing two separate orientations. The separation of the spots can be observed from a distance using a photodetector array in order to determine the misalignment angle of the mirror (Figure 4.2-2).

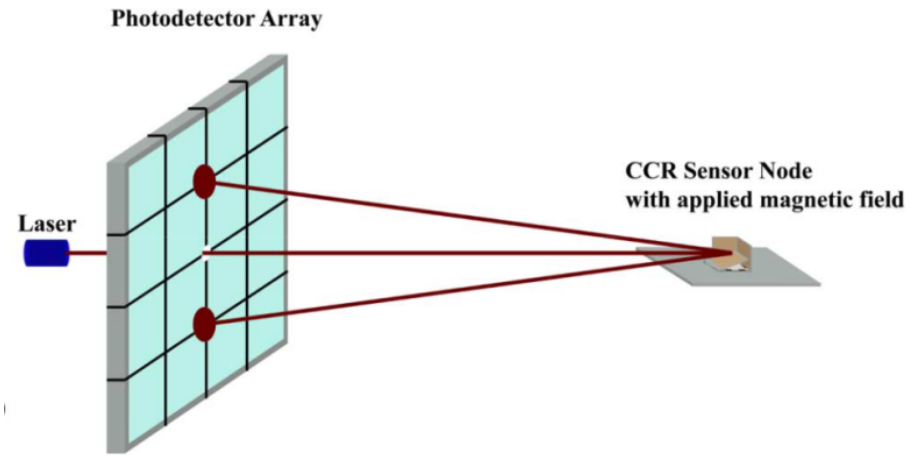

Figure 4.2-2 Interrogation system detects a separation of returns laser spots (Vasquez & Judy 2007)

The separation angle θ is given as

$$\theta = 4\phi\sqrt{\mathrm{Y}^2 + \mathrm{Z}^2} \qquad \textbf{(4.2-1)}$$

where ϕ is the mirror paddle misalignment, which is performed by the mirror in horizontal plane xy. Y and Z are defined by the incident unit vector $\vec{Vin} = \left(-\vec{X}, -\vec{Y}, -\vec{Z}\right)$. It can be seen that the separation angle is determined by not only the misalignment angle but also the incident orientation. For the application where the CCR orientation is unknown, it is suggested that locating a calibration CCR with a known misalignment angle next to the actual CCR sensor will allow the dependence of incident orientation to be compensated for.

Hence

$$\phi = \frac{x_{sensor}}{x_{calibration}} \phi_{calibration} \qquad \textbf{(4.2-2)}$$

where x_{sensor} and $x_{calibration}$ are the separation of the spots observed.

This working principle provides the possibility of detecting an analog change of the paddle misalignment. However, a relatively large photodetector array is required, which increases the system cost and size. Also, the scattering of the returned spots is largely dependent on the incident orientation and the curvature of the micro mirrors so that further processing such as image analysis is required to determine the spot position.

4.3 Design specifications and their effects on optical behaviors

4.3.1 Returned optical power

The optical power returned to the photodetector is important to an interrogation system as it decides the difficulty of signal reading and the quality of the signal to noise ratio. The loss of optical power is mainly due to the divergence during the propagation, the scattering and the absorption during the reflection at the CCR mirrors.

To reduce the divergence during the propagation, collimated laser beams are used during the interrogation. Chu (1998) proposed an interrogation system using a broad laser beam to located the direction of the CCR and once the

communication link is established, the beam is narrowed down for an increased returned power.

The absorption loss can be greatly reduced by improving the reflectivity of the CCR mirrors. Reflection rate varies with different mirror materials and different incident wavelengths. Silicon's reflection rate to visible light is 30%, which shrinks down to a total reflection rate of 2.7% ($30\%^3$) due to the three times reflection in a CCR. A 50nm gold coating will greatly improve the reflectivity of the silicon surface (Zhou et al. 2003). But for a gold surface, the reflection rate is about 33% at the incident wavelength of 406nm while it changes to 97% at a wavelength of 780nm (Bircher et al. 2013).

The surface roughness affects the scattering loss. According to Agarwal et al (2007), the RMS (Root-Mean-Square) surface roughness needs to be less than 50 nm to keep the scattering loss below 50%, as shown in Figure 4.3-1.

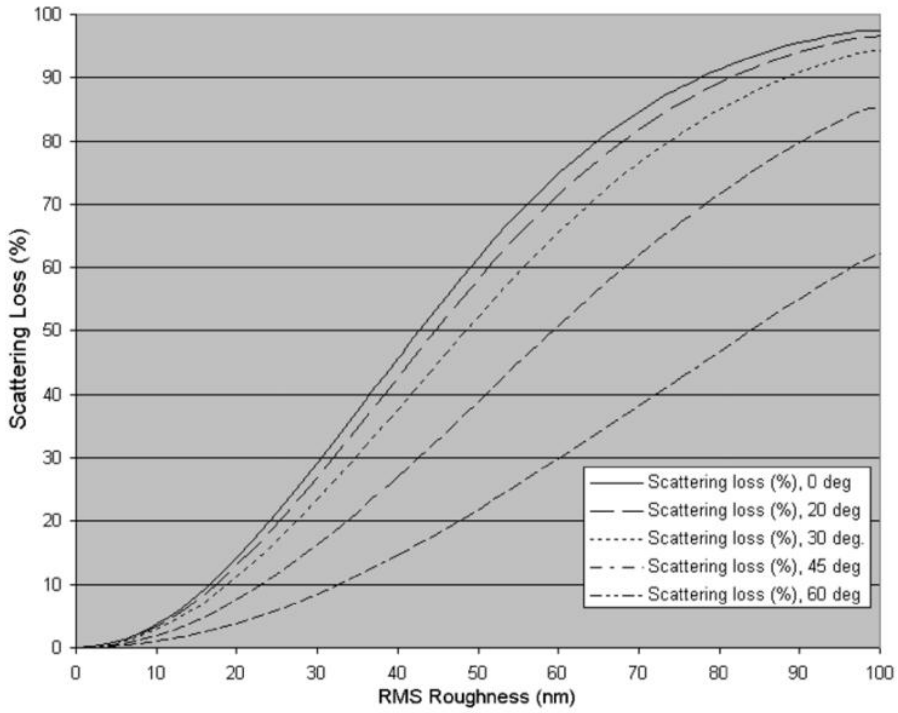

Figure 4.3-1 Scattering loss increasing with surface RMS roughness, with different incident angle (R Agarwal et al. 2007)

When an aligned CCR is remotely interrogated by a laser, the returning optical signal power received by the interrogator P_{signal} can be evaluated by (Zhou et al. 2003)

$$P_{signal} = \frac{P_i}{\pi L^2 \tan^2 \theta_i} \times \frac{A_c}{L^2} \times \frac{3a^4 r_m^3}{\lambda^2} \qquad \textbf{(4.3-1)}$$

The first term of this equation is the light intensity incident on the CCR. P_i is the interrogation laser power, L is the distance between the CCR sensor and interrogator, and θ_i is the divergence half angle of the interrogation beam. The second term is the solid angle that the interrogator subtends, observed at the CCR. A_c is the light collection area of the interrogator, which is assumed to be

very small comparing to the distance L. The last term is called the collinear differential scattering cross section, which is a parameter describing the CCR optical performance. r_m is the reflectivity of the mirror and λ is the incident light wavelength. The formula only applies when the CCR is formed by three square mirrors with the side length of a and the laser is incident along its body diagonal.

4.3.2 Mirror curvature

The curvature of the mirrors affects the returned light scattering as well as the CCR sensitivity to mirror misalignment. In Vasquez & Judy's (2007) experiment, the radius of the CCR mirror curvature is measured to be 10cm. The interrogation result from a distance of 1 m is shown in Figure 4.3-2.

Zhu et al. (2002) showed that the nonflatness of the mirrors is significantly affecting the performance of a CCR. When the curvature of the mirrors is small (i.e. mirrors are not flat), the CCR output received by the photodetector is less sensitive to mirror misalignment, because some part of the misaligned mirror remains well aligned during its tilting. The radii of mirror surface curvature are suggested to be comparable to 1m for a good CCR performance.

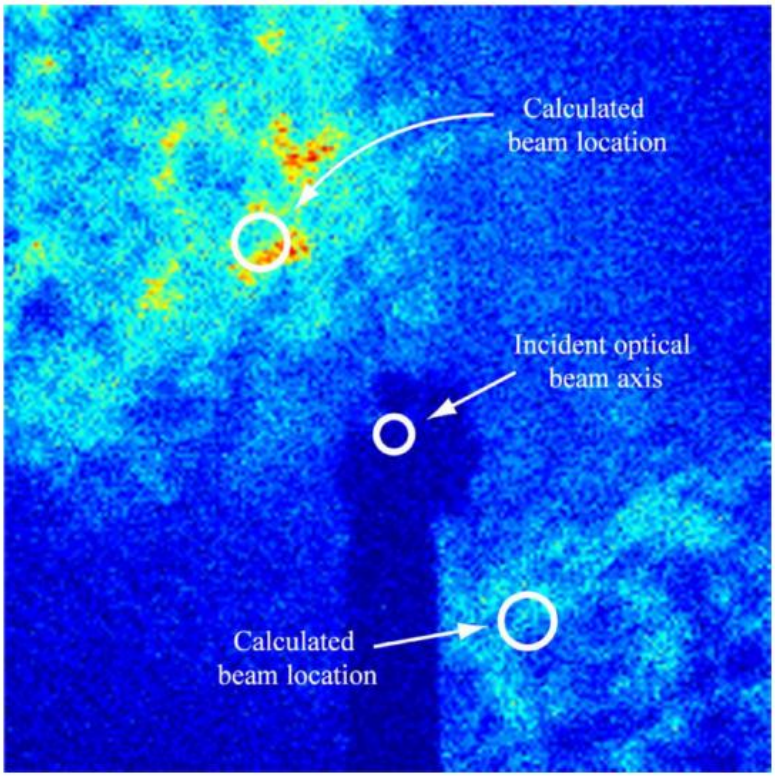

Figure 4.3-2 Wide reflected beam due to mirror curvatures on the order of 10cm(Vasquez & Judy 2007)

4.4 Design setup of the sensor system

A completed sensor node design consists of a paddle resonator and a pair of side walls to form a micro CCR. The paddle dimensions are given at the end of the previous chapter, which proves a large paddle misalignment (tilt angle) to activate the on-off key of the optical communication. A pair of vertical and mutually perpendicular sidewalls with the similar size sits next to the paddle to provide retroreflection, as shown in Figure 4.4-1.

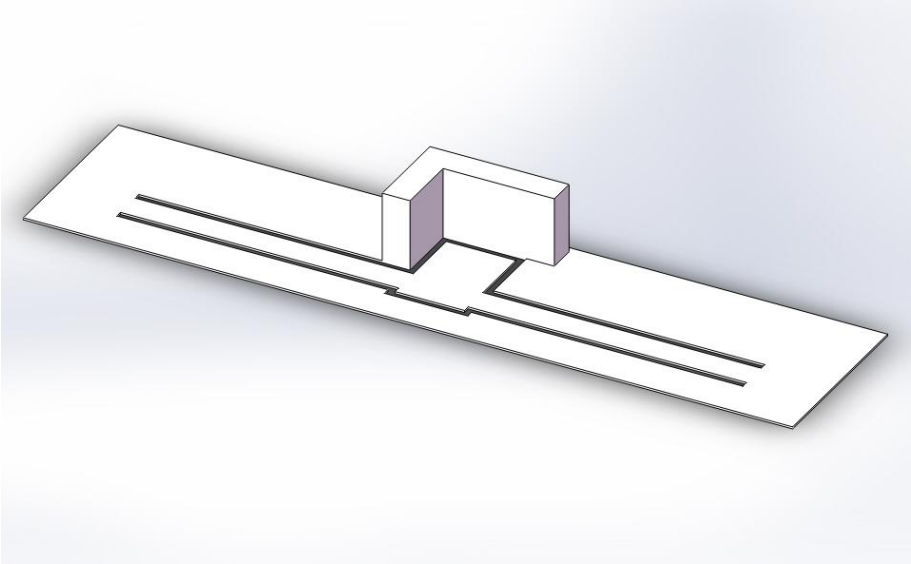

Figure 4.4-1 3D schematic of the micro CCR sensor design

A 50nm thick gold layer is coated on all the mirror surfaces to improve the reflection rate to be 97% for the 780nm wavelength laser. Surface roughness is controlled to be about 50nm for a scattering loss to be less than 50% for most of the incident angle. The curvature is allowed to be 50cm for reasonable misalignment sensitivity.

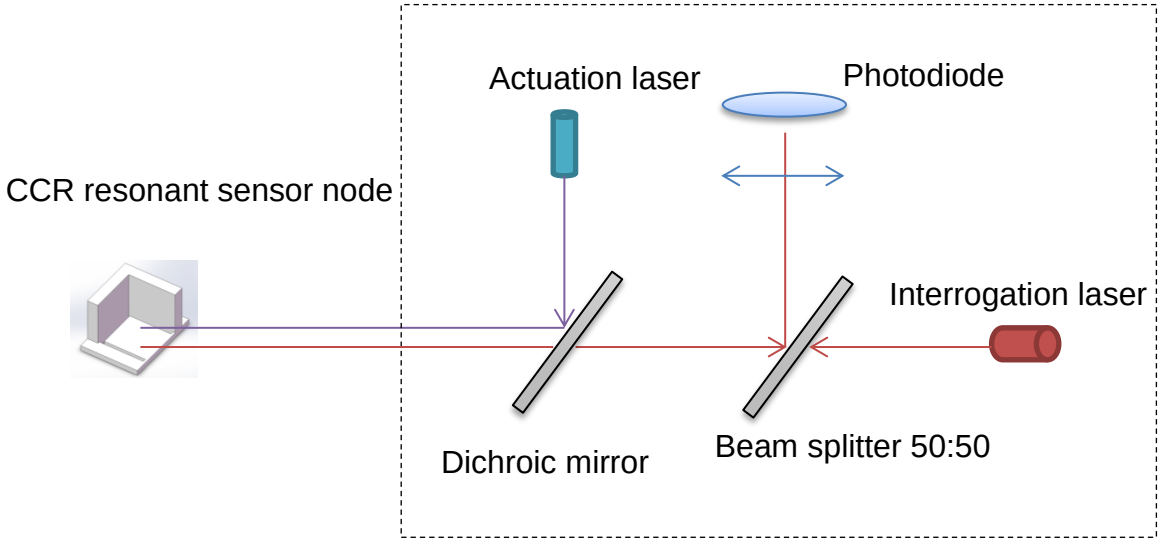

Figure 4.4-2 Schematic of the sensor system setup

A schematic diagram of the sensor system design setup is shown in Figure 4.4-2. A modulated blue laser (406nm wavelength, 50mW) is used to remotely actuate the paddle resonator in the micro CCR sensor node into the translational mode. It is reflected by the dichroic mirror and incident on the sensor while providing an absorption rate of 67% for a gold coated surface. A collimated continuous wave laser with the wavelength of 780nm is used for interrogation, which is highly reflective (97%) on a gold coated surface. It passes through the 50:50 beam splitter and the dichroic mirror then illuminates the CCR. The reflected interrogation light is partially reflected by the 50:50 beam splitter and received by the photodiode. The received signal is compared to the modulated actuation laser signal in order to get the phase angle for resonant frequency locating.

4.5 Conclusions

A micro CCR is introduced to the sensor design in this chapter. A pair of sidewalls of a CCR is combined with a paddle resonator, which provides easy control of the reflected signal. Two principles of detecting the signal are discussed and retroreflection detecting is more suitable for the application than the split beams separation detecting. Optical specifications and their effects on the sensor interrogation are analysed, which proves more constraints to the design parameters. Finally, the design of the CCR resonant sensor is presented and the system setup for the remote optical actuation and interrogation is explained.

Chapter 5: Fabrication of the Paddle Resonator and the Micro CCR

5.1 Introduction

In this chapter, the techniques used in fabricating the designed paddle resonator and the micro CCR structures are investigated separately to reduce the complexity of the total fabrication. The paddle resonator is possible to be fabricated using silicon microfabrication process or nickel electroforming process while the micro CCR is possible to be fabricated with laser machining, silicon dry etching, or SU-8 process. Different approaches of fabricating the paddle resonator and the micro CCR structure are demonstrated in order to test their feasibility and potential limitations. Also, the fabrication samples are characterized to check the mechanical and optical properties. The characterization results and potential problems of each approach are discussed. Then possible fabrication plans of the sensor device are presented. Due to the limitation of accessible fabrication facilities, however, the fabrication of the final device is not presented in this thesis.

5.2 Fabrication of the paddle

A silicon microfabrication process and a nickel electroforming process were tested for the paddle resonator fabrication.

5.2.1Silicon microfabrication process

Silicon processing is fundamental in MEMS fabrication. To make the paddle movable, the structure needs to be built on silicon-on-insulator (SOI) wafers. A SOI wafer is formed by three layers namely device layer, buried oxide layer and handle layer, as shown in Figure 5.2-1. The device layer is a thin layer of silicon on the very top of the wafer for the MEMS device to be made from. Its thickness is normally between 1μm to 30μm. Beneath it is a thinner oxide layer, normally 2 to 5μm thick, which acts as a stop layer between the device layer and the handle layer during etching as well as being a sacrificial layer that can be etched away by hydrofluoric acid (HF) to release the structure above. The handle layer is relatively thick, which is about 400-500μm, providing a supporting substrate for the suspended MEMS device to sit on. Sometimes it can also need to be processed to produce a part of the structure (Chiu et al. 2009).

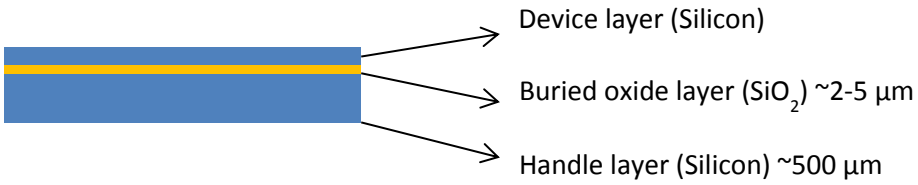

Figure 5.2-1 Schematic of SOI wafer

The silicon process on a SOI wafer includes the following steps, depicted in Figure 5.2-2. First, the photoresist is spin coated on top of the device layer and patterned using photolithography (a). Second, the wafer is etched in a deep reactive ion etching (DRIE) process to remove the exposed silicon (b). Third, the

wafer is diced into smaller chips and cleaned (c). Each of the chips carries an individual device. Then the chips are etched using HF so that the movable device is released (d).

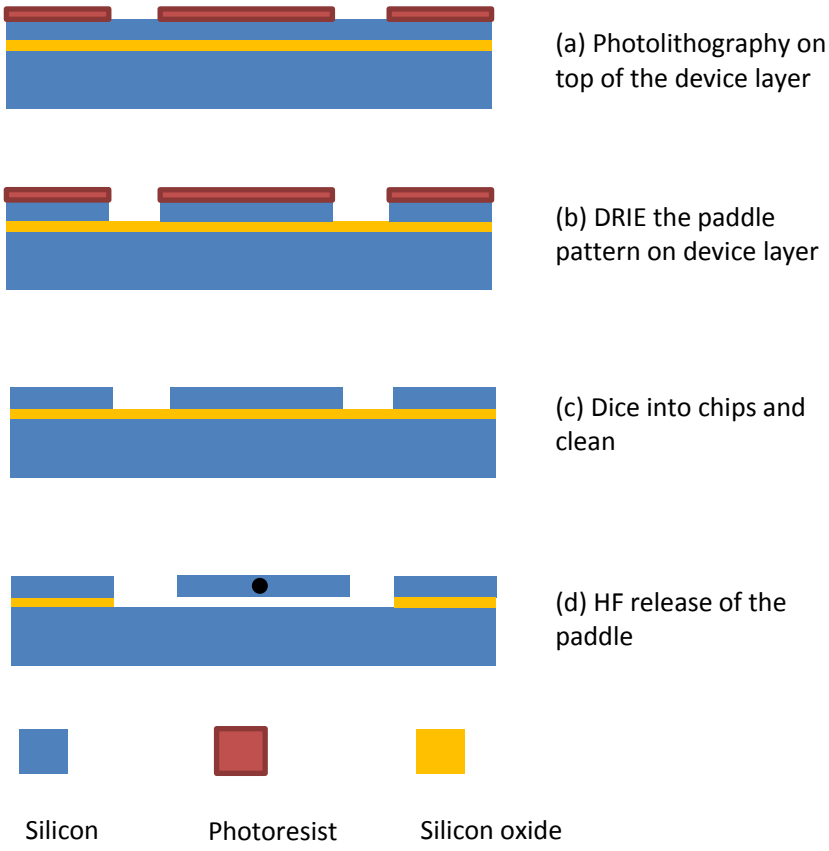

Figure 5.2-2 Process flow of a paddle fabrication on SOI wafer

An interdigital resonator structure (Carter et al. 2009) was processed in SOI in the early stage of this study in order to investigate the feasibility of paddle fabrication. The resonator design was chosen as a mask was available, and meant that the process could be assessed for suitability before purchasing a mask with the paddle design. Shipley Microposit® S1813 photoresist was spin

coated on a SOI wafer which has 20μm device layer, 2μm oxide layer and 500μm handle layer. After UV (ultraviolet) lithography, the wafer was developed in Microposit® MF-319 to expose the unwanted silicon pattern. Then the wafer was etched in a Surface Technology Systems (STS) etcher for 25min with the Bosch switched process (Franssila et al. 2000) of 5s etch and 3s passivate. Next, the wafer was diced into 5mm×5mm chips using a diamond saw and cleaned using the Microposit® 1165 remover, followed by an 8min HF etch. After that the chips were washed in isopropyl alcohol (IPA) and placed immediately on a 110˚C hot plate to vaporised the IPA and release the moving parts.

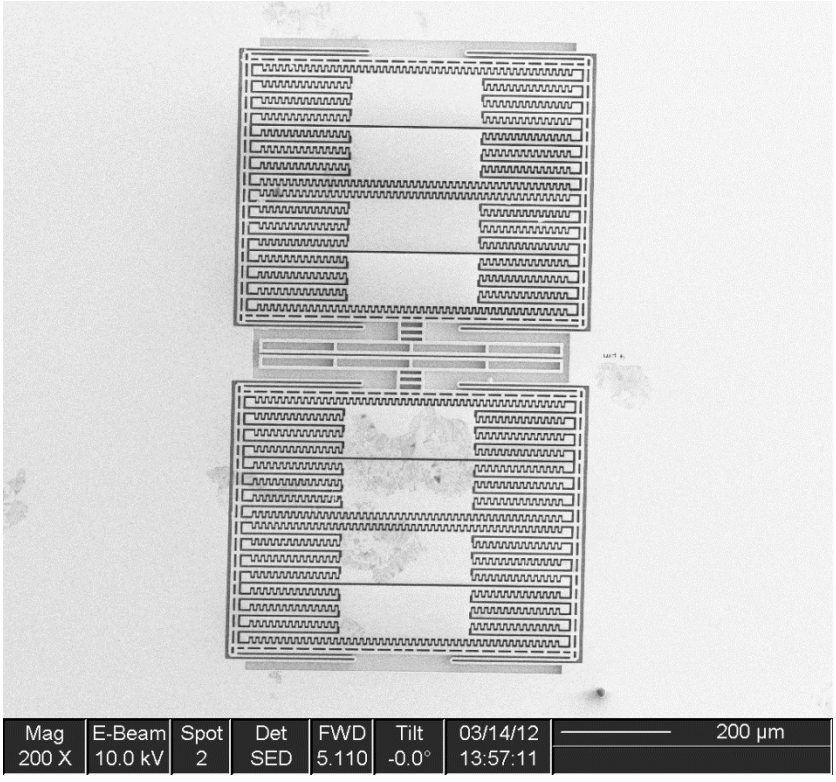

Figure 5.2-3 SOI fabricated interdigital resonator structure

One of the result samples is shown in Figure 5.2-3. It can be seen that the structure geometry has different types of features. It has small gaps and finger features which are several microns wide, as well as a large area of the structure which needs to be released so that it can be electrostatically driven into resonance. However, there are several potential problems that can affect the fabrication result.

1. The limitation of UV photolithography

When the feature size is about or under 1μm, there is a high possibility that the photolithography is not able to copy the pattern from the mask to the photoresist. As shown in Figure 5.2-4, in the center of the structure, there is a 1μm gap designed on the mask to separate the two moving parts. However, the gap is just half way produced, which leads to a half connected structure after DRIE.

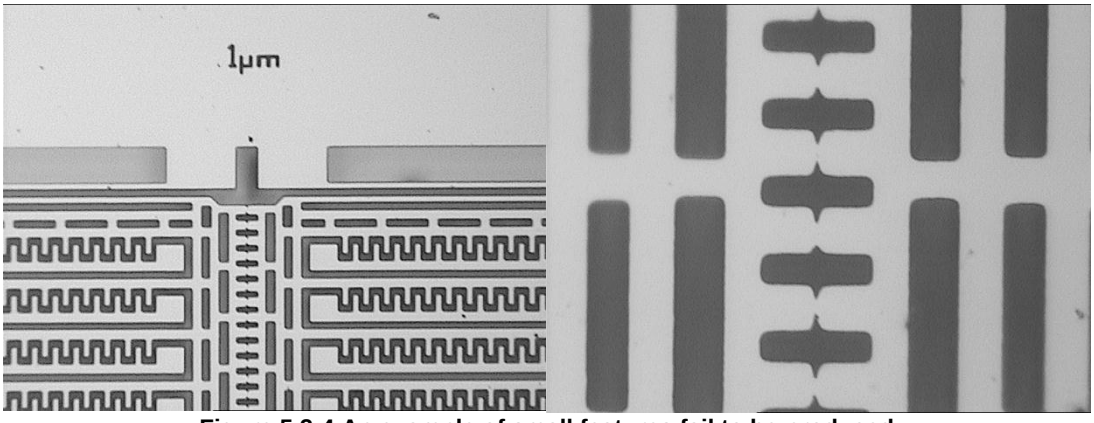

Figure 5.2-4 An example of small features fail to be produced

Mask printing resolution, UV exposure dose and development time can cause this problem. If the gap on the mask is printed smaller than the design, the actual

gap will be comparable to the wavelength of the UV light, which can cause diffraction that distorts the gap shape. Since the photoresist coat is thin (about 0.5μm in this fabrication), the resolution of the photolithography result is very sensitive to the UV exposure time. Both excess and insufficient exposure dose will affect the gap size. Also, the development time is critical to the small features as local chemical reaction rate in the small gaps are different to that in large features. If the developer does not completely dissolve the photoresist in the gap, the residual will still shade the silicon, leaving a half connected structure.

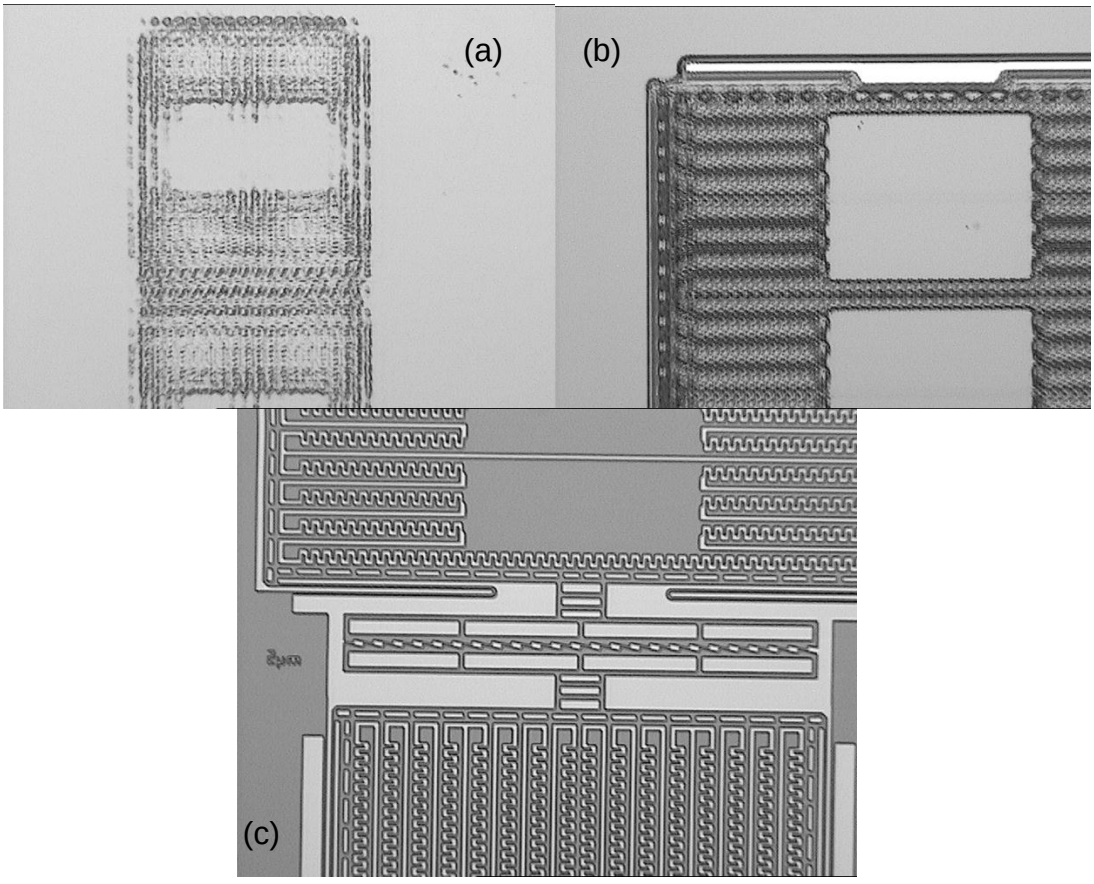

Figure 5.2-5 Resolution improving with contact pressure. (a) and (b) soft contact mode exposure with different length of time. (c) hard contact mode

Mask contact mode is another factor that can affect the photolithography quality. Mask contact mode is a parameter that can be set as soft contact or hard contact on the mask aligner (Cannon PLA-501FA is used in this fabrication). It decides the contact pressure between the bottom of the mask and top of the photoresist. It can be seen from Figure 5.2-5 that contact mode with higher pressure (hard contact) improves the resolution of the photolithography.

2. Notching effect

Notching effect, also known as footing effect, is likely to occur in high aspect ratio SOI DRIE process. It is caused by built up charge on the oxide layer and the repelling of the ions from it when the process has finished etching the device layer (Wasilik & Pisano 2001), shown in Figure 5.2-6.

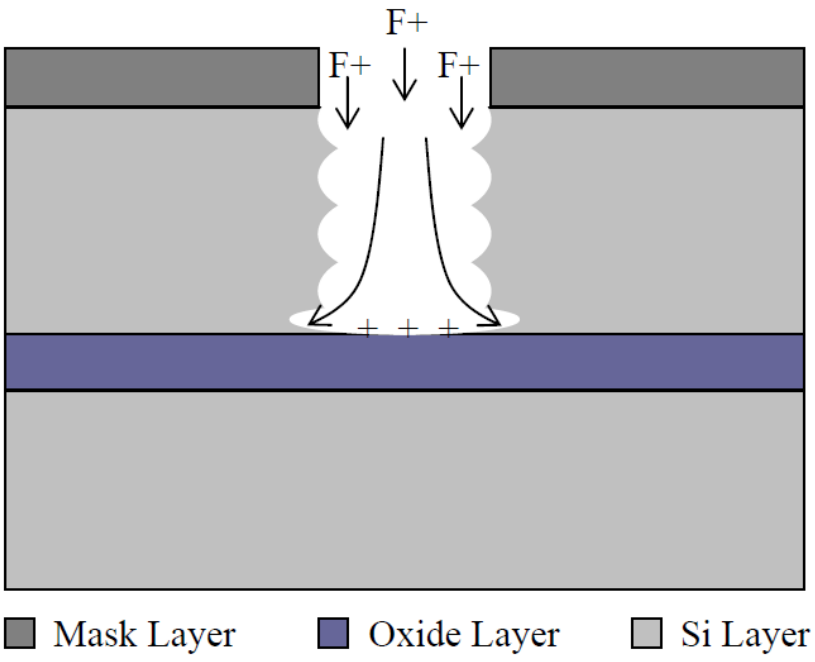

Figure 5.2-6 Schematic of notching effect in BOSCH DRIE (Munro 2009)

Notching effect occurs in the fabrication as shown in Figure 5.2-7. Since this is at the stage before HF release step, there should be no gap between the device layer and the oxide layer in theory. It can be seen that repelled ions have cut through the bottom of the device layer, which distorts the structure dimension and leaves repelled scraps under the structure which can cause obstructions for its movement.

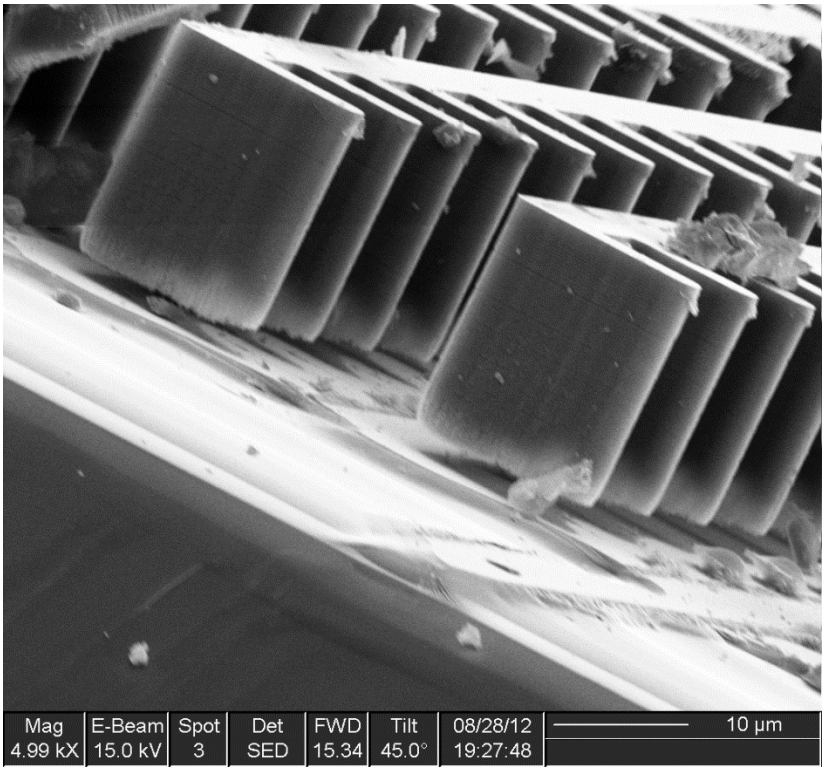

Figure 5.2-7 Notching occurs at the bottom of device layer

To minimize this undesired effect, low frequency power supply can be used. Typically the Bosch processes use a 13.56MHz power generator. By applying a lower frequency, which is 380kHz (Munro 2009), the charge build-up can be

decreased so that more ions can escape out of the surface in order to reduce the notching effect.

3. HF releasing time

HF release is another important step to complete a SOI MEMS fabrication. For the interdigital structure fabrication, a large area of the oxide layer needs to be etched away to release the device above. The HF etching time is crucial for a successful release of the MEMS structure. Shown in Figure 5.2-8, the residual oxide block prevents the structure from moving freely. Therefore, the HF releasing time needs to be sufficient whilst the structure geometry needs to be designed to enable a uniform etch depth throughout the area.

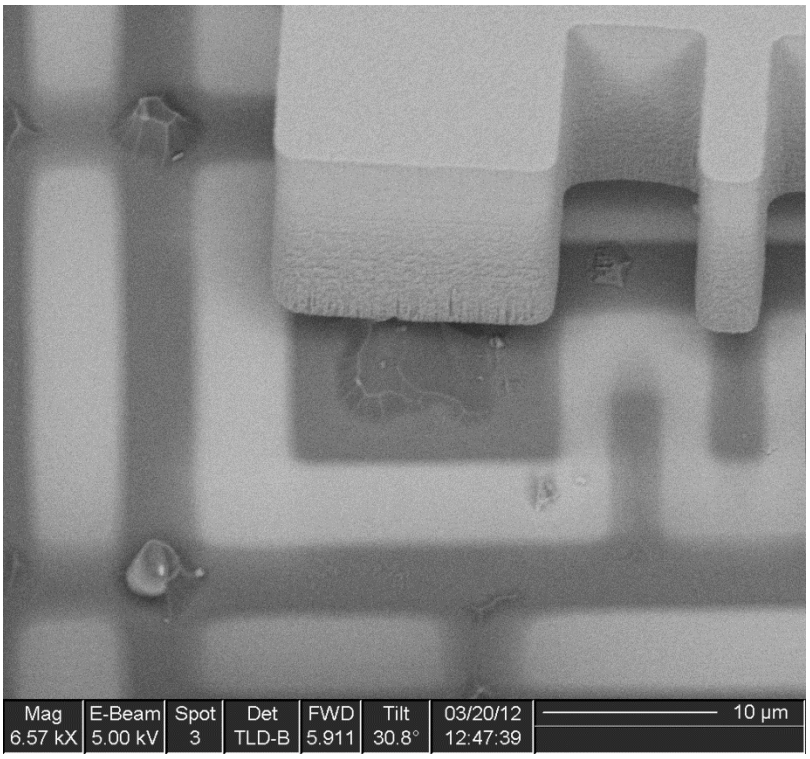

Figure 5.2-8 Residual of the oxide layer stops parts from moving

In order to release a paddle structure in the size of several hundreds of micron, the surface of the paddle needs to be modified to have an array of several microns wide holes. These holes allow the HF to etch the oxide layer under the paddle uniformly while introducing minimum effect to the paddle optical and mechanical properties.

5.2.2 Micro electroforming

Electroforming, also called electroplating, is a process of metal forming. It utilizes external voltage to dissolve the anode metal, transfer the metal ion through the electrolyte, and coat the metal onto the cathode.

The electroforming rate is given by (Bari 2010)

$$m = M/nF \times aIt \qquad \textbf{(5.2-1)}$$

where

- m, total mass deposited
- M, atomic weight
- n, the number of electrons in the reaction
- F, Faraday's constant
- a, current efficiency ratio
- I, current
- t, time

The principle of electroforming is used in LIGA (Lithography, Electroplating, and Moulding) to form micro metal structures. A process flow of UV LIGA is shown in

Figure 5.2-9: A substrate is prepared (1) and a conductive seed layer is coated on top of it (2). Then a thick layer of photoresist is coated onto the seed layer (3) and UV lithography is applied (4). After the development of the photoresist (5), electroforming is performed to fill up the mould created by the photoresist (6). Finally, the photoresist mould (7) and the seed layer (8) are etched away to release the metal components. The materials of nickel, copper and gold are commonly used in LIGA.

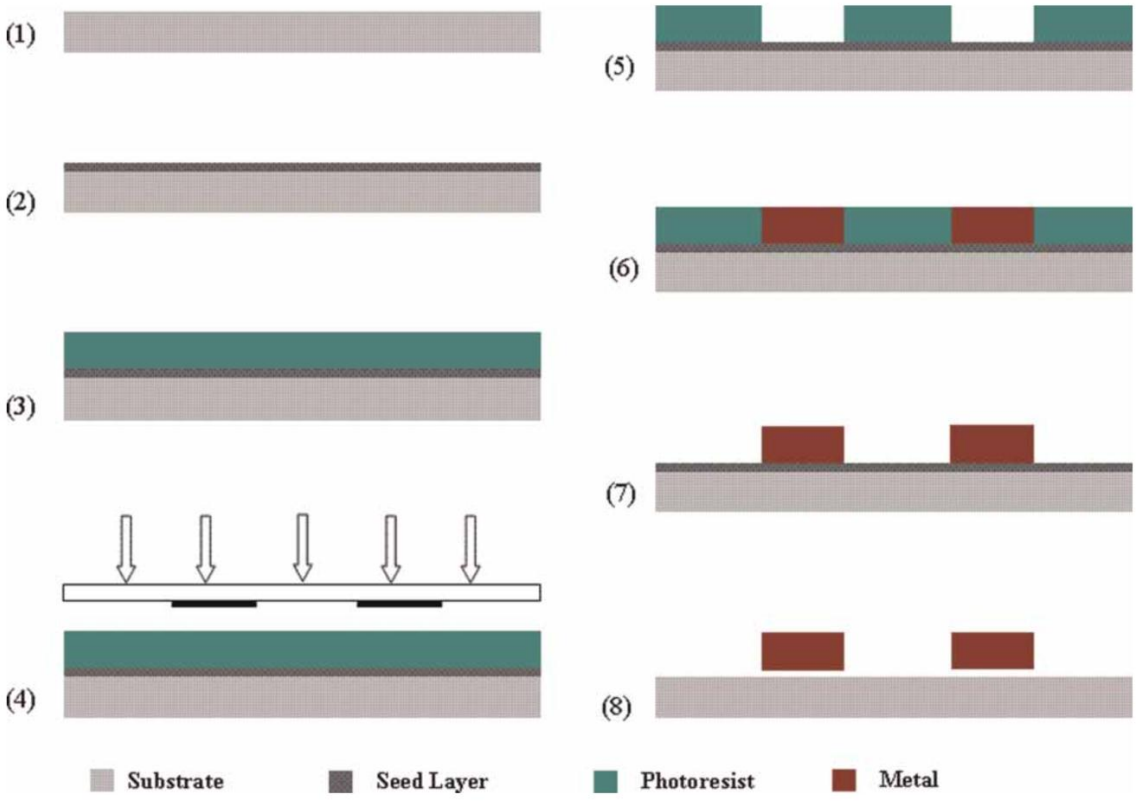

Figure 5.2-9 A flow diagram of the UV LIGA fabrication (Wei et al. 2008)

Electroforming via the LIGA process is another approach to make the micro paddle resonators. It has been proved that electroformed nickel resonator has

good performance (Shi et al. 1995). Therefore, nickel is used to prove the feasibility of the paddle fabrication.

5.2.2.1 Fabrication process

The process of making the photoresist mould for electroforming a 20μm thick paddle resonator is carried out as follows. First, a seed layer of gold is coated on a cleaned silicon wafer using gold sputtered for 60s. Second, a 20μm thick layer of Shipley BPR-100 negative photoresist, which is chosen because of its good tolerance to UV overexposure (Wei et al. 2008) and the ability to be easily stripped off with 1165 remover (Jiang 2010), is spin-coated on top of the seed layer at a spinning speed of 1450rpm. Then the edge bead is removed and the wafer is soft baked for 3min at 65°C to remove stress then 20min at 95°C on a hot plate. UV exposure is carried out for 160s with 350nm light filter under a light intensity of 12.6mW/cm^2. After that, the photoresist is developed with diluted BPR developer for 10mins.

The mask used in this process is shown in Figure 5.2-10. Since BPR-100 is a negative photoresist, the unshaded area is the area to be UV exposed and stay after development.

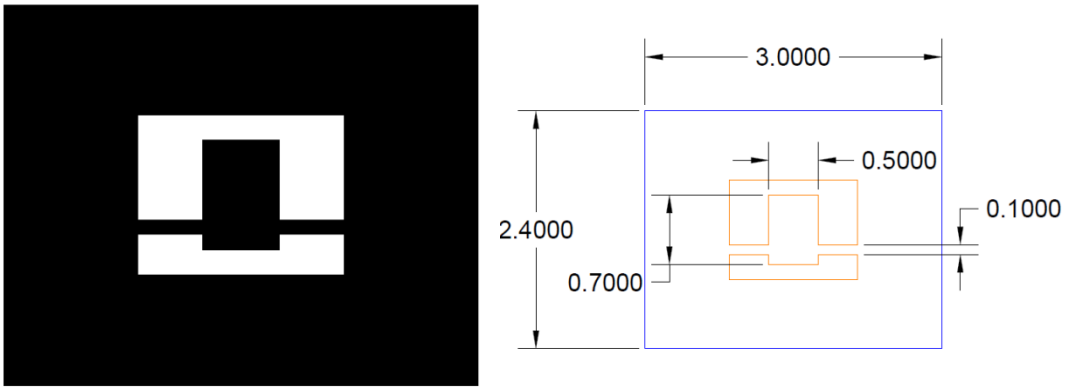

Figure 5.2-10 Mask used in mould making and its dimensions in mm

Figure 5.2-11 shows the result of the mould making. It can be seen that wafer contains a photoresist mould layer on sputtered gold. Four corners are left to be blank in order to connect with electrodes for electroforming.

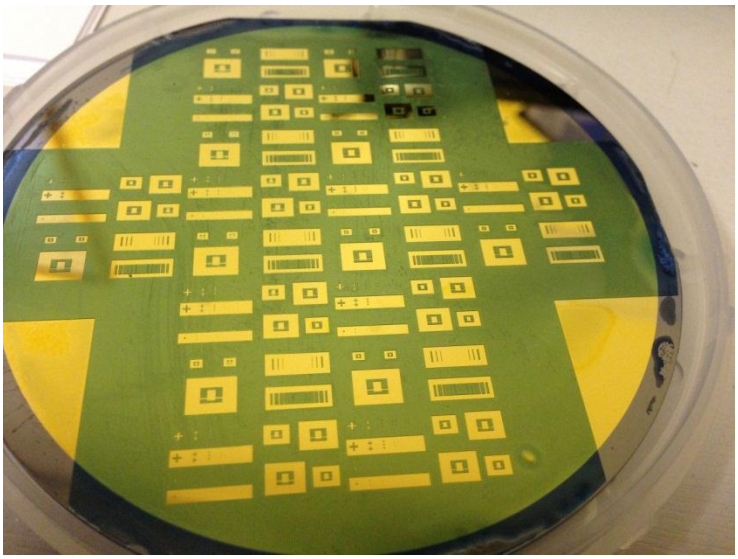

Figure 5.2-11 BPR-100 photoresist mold

An optical metrology system the Alicona infinite focus system (Alicona Imaging GmbH, Austria) is used to check the status of the photoresist mould before electroforming. The sample is scanned to form a 3D model with real dimensions

and morphology. Dips occur at the corner of the model structure due to the low reflectivity at the photoresist mould corners which cause inaccuracy of the optical system (Figure 5.2-12 a). A profile in the vertical plane along the orange segment is plotted in Figure 5.2-12 b, which gives the measurement of the thickness of the mould to be 72μm. This is much thicker than the expected thickness in the mould fabrication plan, which can be caused by the dehydrated photoresist that is stored in the lab for a long period of time.

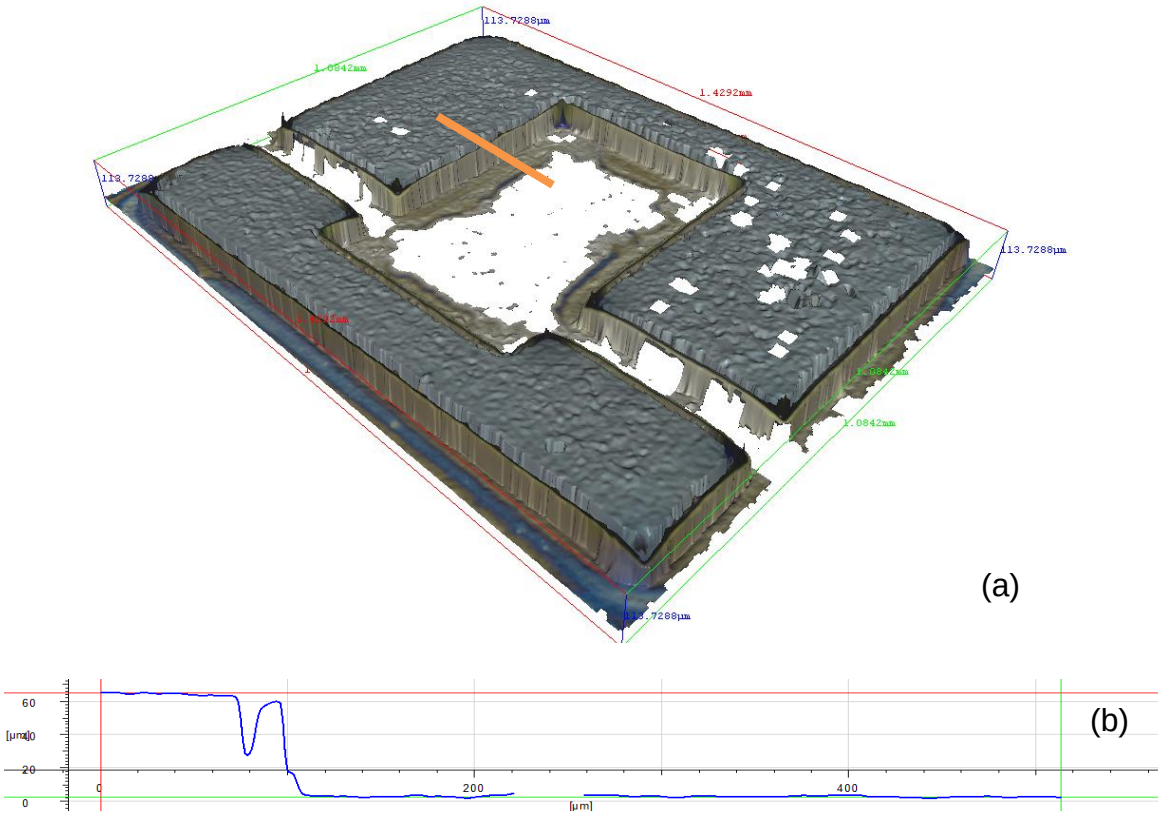

Figure 5.2-12 3D result of the Alicona scanning (a) and thickness measurement (b)

The electroforming experiment rig is shown in Figure 5.2-13. The wafer with the photoresist mould is mounted in the white square holder which is in the middle of

the blue electrolyte column, connecting to the cathode of a power generator. Meanwhile, a bulk of nickel is mounted through the back of the column, opposite to the photoresist mould and connecting to the anode of the power generator. A pump is used to circulate the electrolyte during the process.

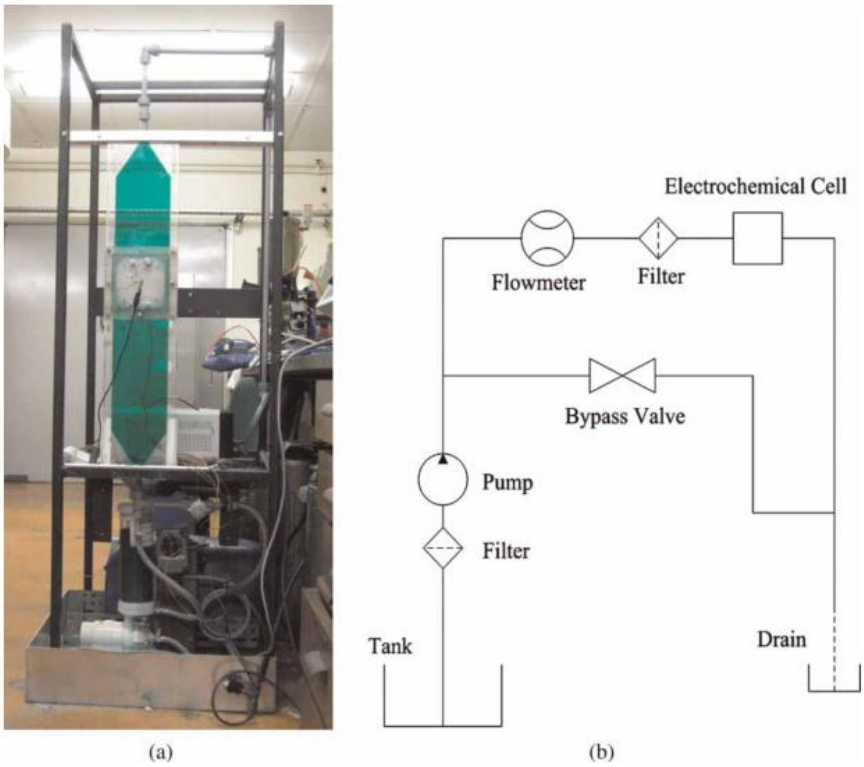

Figure 5.2-13 (a) A photo of the micro electroforming rig. (b) A schematic of its construction (Wei et al. 2008)

To ensure the photoresist mould is not peeled off due to the current generated heat, the maximum current density is limited at 20mA/cm^2 (Basak et al. 2007). Also, the solution is heated up to 50°C in order to provide an active temperature without attacking the mould. The total area of the exposed seed layer is calculated to be 25.5cm^2, hence the suitable current is 0.5A. Using equation

(5.2-1), it can be calculated that the process needs to be run for 50min in order to get a 20μm thick nickel paddle.

5.2.2.2 Morphology characterization

SEM images are taken to characterize the electroformed nickel paddle after demoulding (Figure 5.2-14). It can be seen that the geometry of the paddle is obtained except losing some of the sharp features at corners. The top surface is also relatively rough. Figure 5.2-15 provides a close section view of a paddle supporting beam. The vertical profile is shown to be not straight.

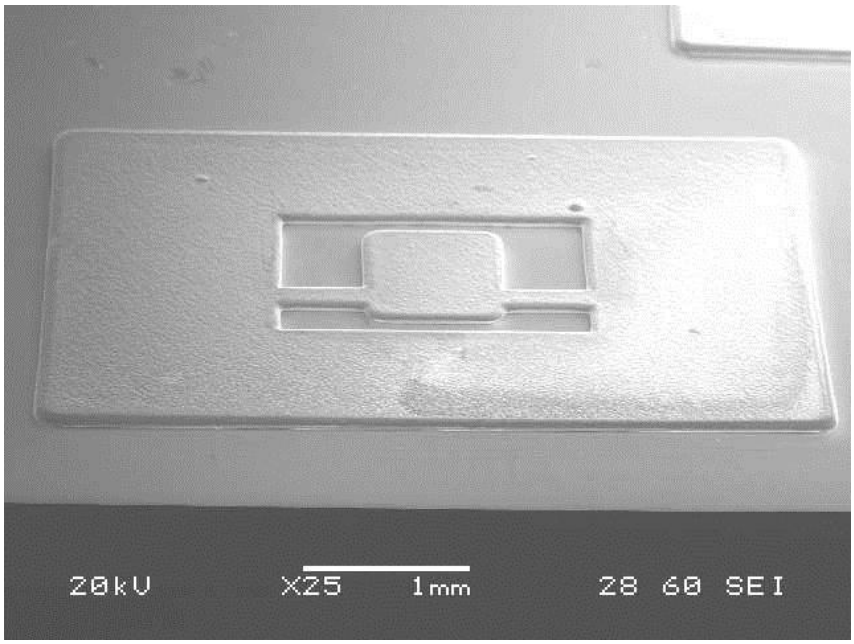

Figure 5.2-14 Nickel structure after demoulding

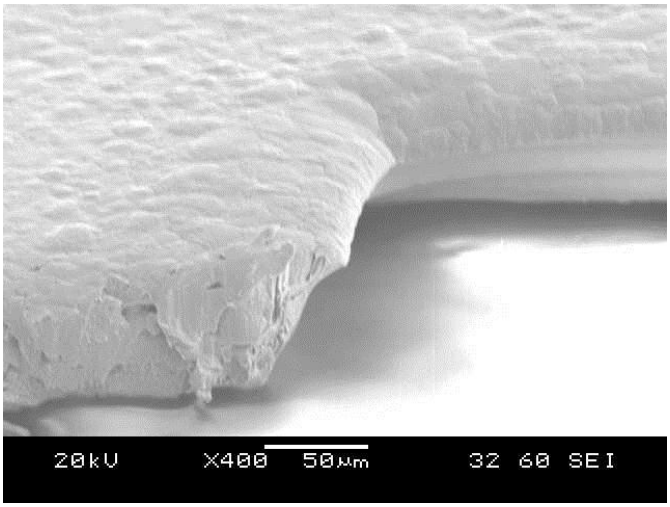

Figure 5.2-15 A section view of a paddle supporting beam

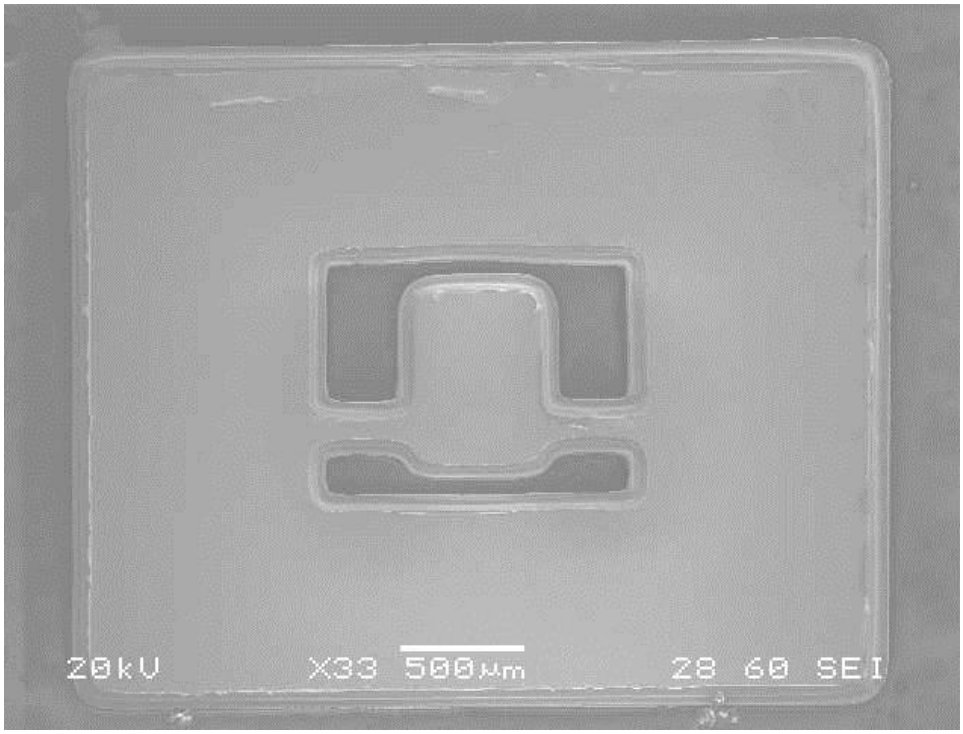

Figure 5.2-16 Gold coated surface of the nickel structure

Since the seed layer of gold is sputtered on the wafer, it adhesiveness is not as strong as that when the seed layer is produced by physical vapour deposition.

Therefore during the demoulding process, nickel paddles can be easily stripped off from the substrate without using any seed layer etchant. The gold layer remains on the back of the paddle as the gold has better adhesion with deposited nickel than with polished silicon. Shown in Figure 5.2-16, the back of the nickel paddle is coated with a very smooth gold layer, which is ideal for the paddle to be used in an optical application. Moreover, additional gold can be deposited on the top surface after the paddle is released to achieve better reflectivity if required.

Surface roughness of both side of the paddle samples are characterised in Alicona. Surface morphology under 100 times magnification is shown in Figure 5.2-17. It can be seen that the nickel top surface is full of bumps and hollows where an average RMS surface roughness of 236 nm is measured. Conversely, the back side with gold layer shows good smoothness, giving an average RMS roughness of 33.5 nm.

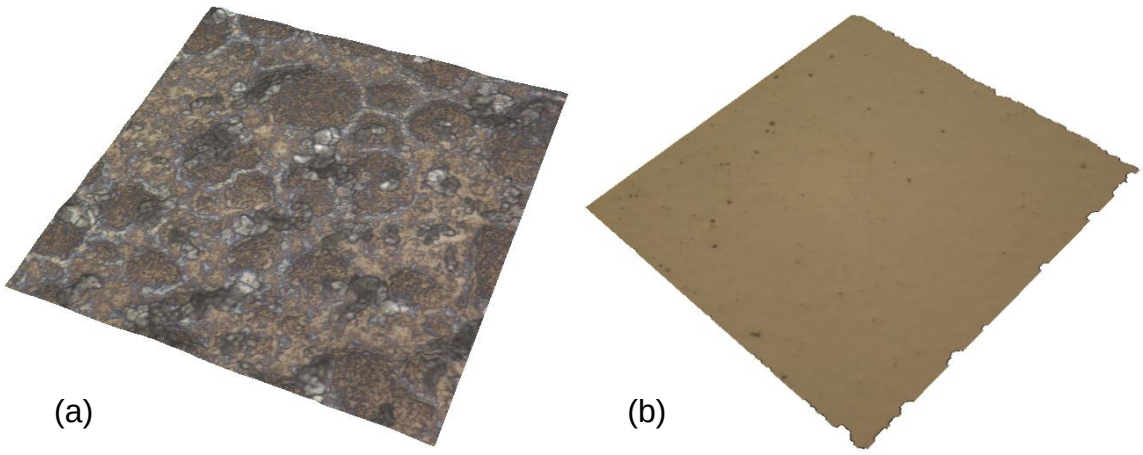

Figure 5.2-17 Surface morphology of both sides of the electroformed nickel paddle. (a) top side (b) back side

5.2.2.3 Dynamic characterization

An AFM is modified to be used as an optical vibrometer for the electroformed nickel paddle dynamic test, as shown in Figure 5.2-18. The measurement tip of the AFM is removed and a piezo disc is mounted on the sample stage. The paddle frame is adhered onto the piezo disc by thermal tape while the paddle is suspended so that it can vibrate freely.

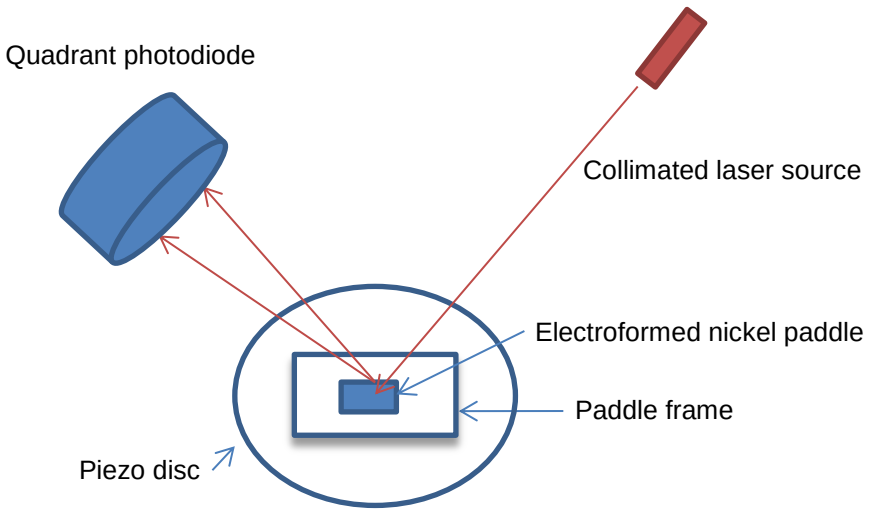

Figure 5.2-18 A schematic of the modified AFM optical detecting system

When the piezo disc is connected to a signal generator, it starts to vibrate which actuates the sample paddle. The position of the reflected laser spot is detected by the quadrant photodiode. It differentiates the light intensity collected by four quadrants to get the position of the light spot and sends a voltage signal depending on it. The output signal is collected by a National Instruments (NI) data acquisition card. LabView Express is used to process the signal.

Figure 5.2-19 and Figure 5.2-20 are the plots of two groups of amplitude data of the frequency sweep result. The difference between them is that the former has the laser spot pointed on the paddle while the latter has it on the paddle frame. The frequency of the actuation signal is controlled to sweep from 500Hz to 150kHz. The amplitude of the voltage signal detected from the reflected laser is recorded to show the amplitude of the vibration at each frequency. Due to a malfunctioning quadrant photodiode fastening mechanism, the photodiode gradually droops during the frequency sweep data collecting process. Therefore, the plots show undesired voltage increase along with the frequency.

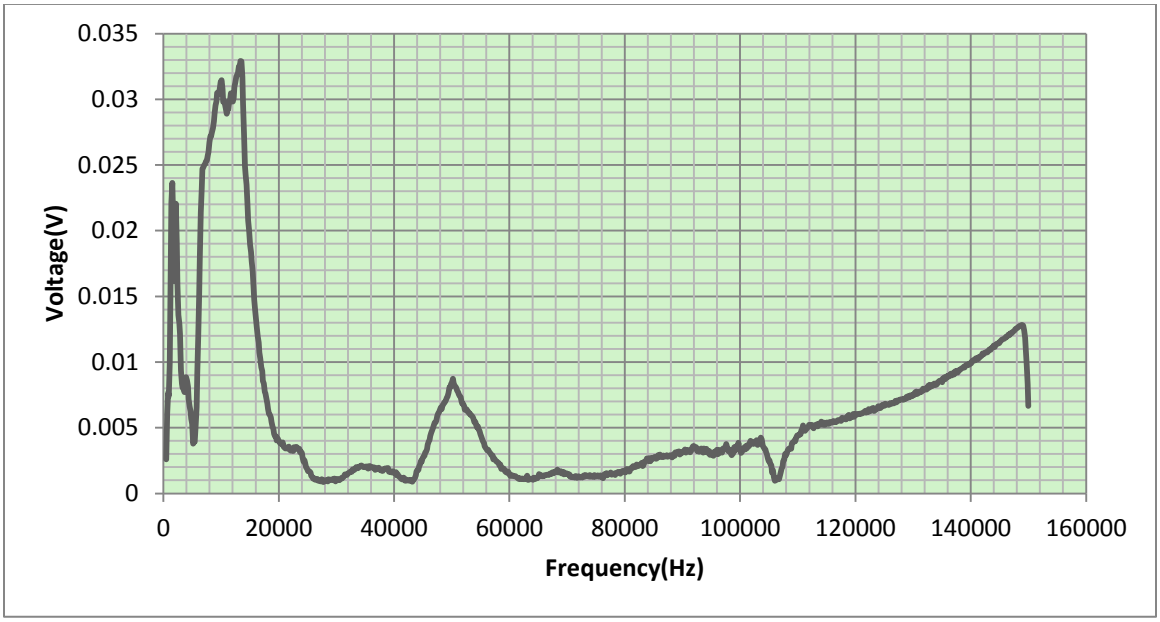

Figure 5.2-19 Result when laser is pointed on the paddle

Figure 5.2-19 shows that several resonance peaks occur when the vibration of the paddle is interrogated by the laser. To eliminate the interference of system vibration, the laser is adjusted to point to the paddle frame for another sweep,

which gives the result shown in Figure 5.2-20. The amplitude plot shows that the resonance peak at 50kHz disappears when the supporting structure rather than the paddle is being interrogated. But the rest part of the plots maintains nearly the same. Therefore, the 50kHz is deemed to be the paddle's resonance frequency. It can be seen from Figure 5.2-19 that the bandwidth of the resonance peak is about 10kHz which gives a Q factor of 5. This value is much smaller than the value of 300 assumed in the analytical discussion. The reasons for the difference are: (1) the paddle is made of nickel, which has more intrinsic energy loss in resonance; (2) the paddle is mounted using a thermal tape which could lead to energy loss during coupling with the piezo; (3) the gap between the paddle and the piezo is very close. As the measurement is performed in air, squeezing the air layer in between causes large damping to the paddle.

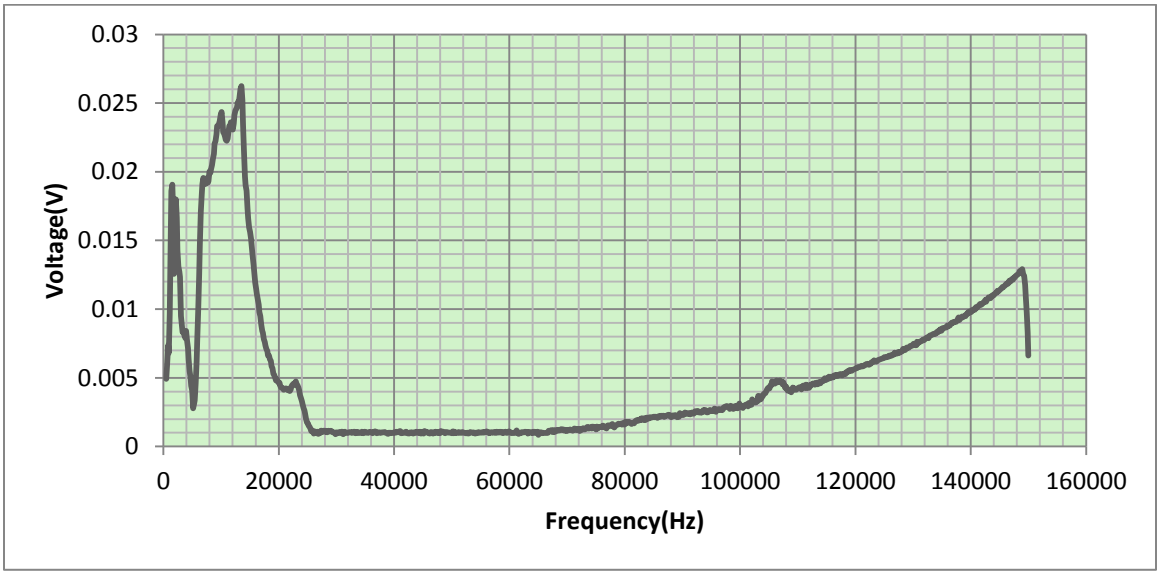

Figure 5.2-20 Result when laser is pointed on the paddle frame

5.2.3 Summary of paddle fabrication

Two fabrication techniques that can be used for the paddle resonator fabrication are presented and discussed in this section. The silicon microfabrication process with SOI has shown good feasibility of fabricating the paddle resonator, as long as the notching effect is controlled and micro holes are included in the design to facilitate HF release. It has good control of the structure geometry especially thickness and it is capable of very thin device fabrication as the device is supported by the handle layer. The downside of this fabrication method is that it is costly in both material and fabrication process. The LIGA, or micro electroforming, method has been experimentally shown to be feasible of fabricating micro paddle which can be actuated into resonance at 50kHz. Although accurate structure geometry is not easily achieved, a smooth gold layer coated surface makes this fabrication method very suitable for the optical application. High internal stress is a potential problem of electroforming that needs more post process such as anneal (Jaleel & Abdulnoor 2010).

5.3 Fabrication of the micro CCR

As introduced in Chapter 2, three mutually perpendicular mirrors are required in order to form a CCR. In this section, several fabrication methods of a micro CCR structure, especially the two side mirrors, are tested and discussed.

The main difficulty of a micro CCR fabrication is to get mutually perpendicular sidewalls while keeping them smooth and vertical. This is crucial to the quality of the return signal. For acceptable optical results, vertical mirrors should have their RMS surface roughness less than 50 nm (Agarwal et al. 2007a) and the verticality as close as 90° to communicate over free space (Park & Park 2013). Also, the radii of mirror surface curvature should be larger than 50cm (Zhu et al. 2002). Attempts are made to approach these specifications.

5.3.1 Laser machining approach

Laser machining is a relatively new fabrication technology that utilizes the high temperature generated by focused laser pulses to vaporize and remove materials. An LASEA multi-axis laser micro machining centre is employed to process the micro CCR fabrication. It has 3 optical axes for the laser head and 5 mechanical axes for the sample stage. The stage XY axes resolution is 0.25μm and that for Z axis is 0.5μm. The wavelength of the laser is 1064nm whilst the pulse duration is 4-250ns. A simple test structure which contains two pairs of vertical sidewalls is sent to the laser machining centre (Figure 5.3-1). The thickness and width of the sidewall are both 150μm.

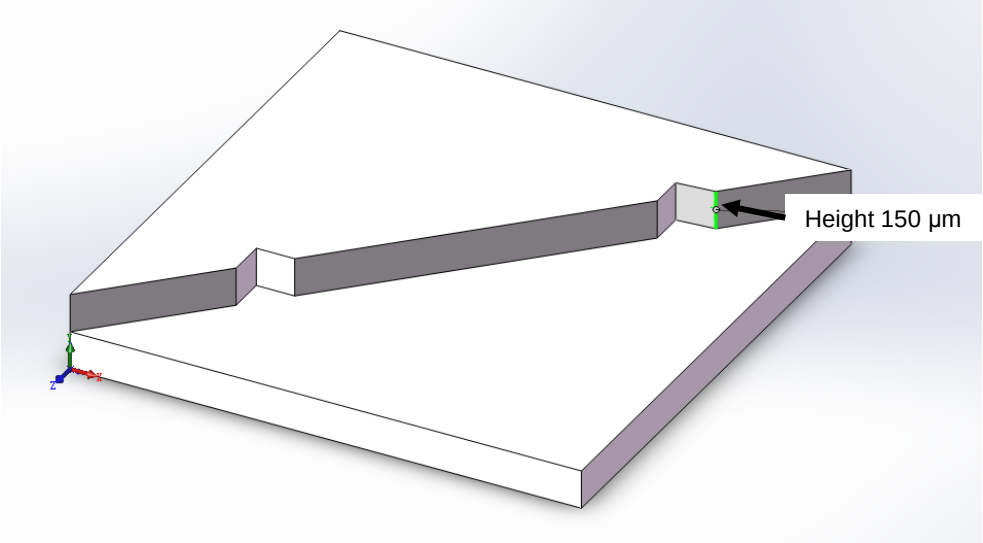

Figure 5.3-1 Structure sent to laser machining center

The laser machining is applied on a piece of stainless steel plate, as shown in Figure 5.3-2. The circled sample is taken into an optical microscope for characterization.

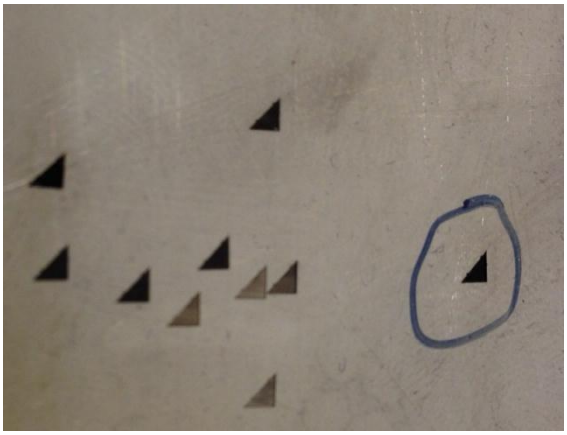

Figure 5.3-2 Structure machined on a piece of stainless steel

Figure 5.3-3 shows the optical image of the top surface and laser machining profile. It can be seen that the details of sharp corners are lost in the machining

result. This is due to the size and shape of the cutting tool which is the laser spot with a minimum spot size of 14μm.

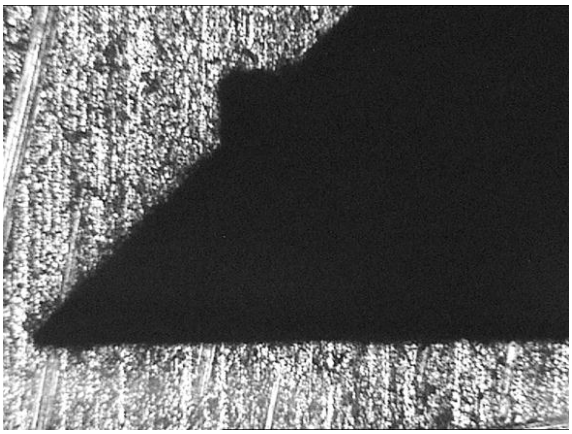

Figure 5.3-3 Top surface of the laser machined structure

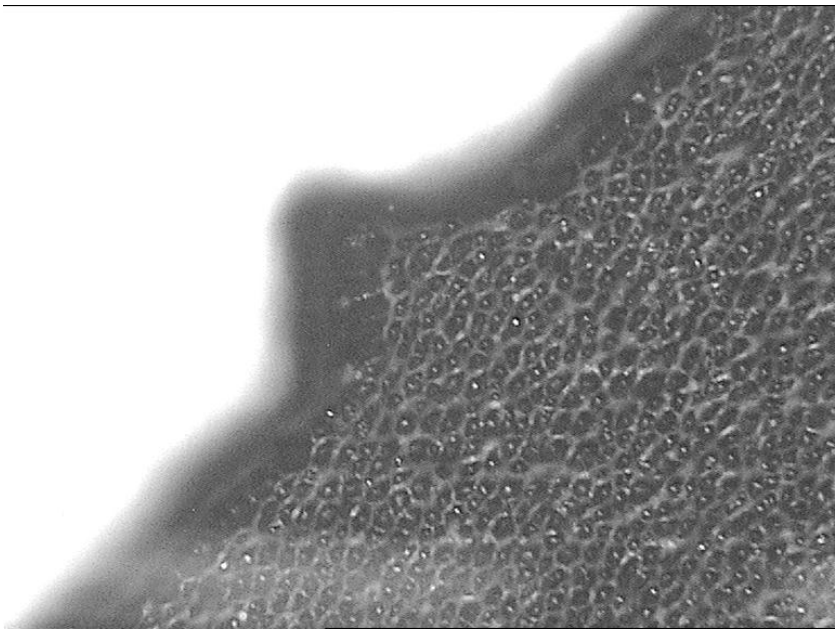

Figure 5.3-4 Bottom surface of the laser machined structure

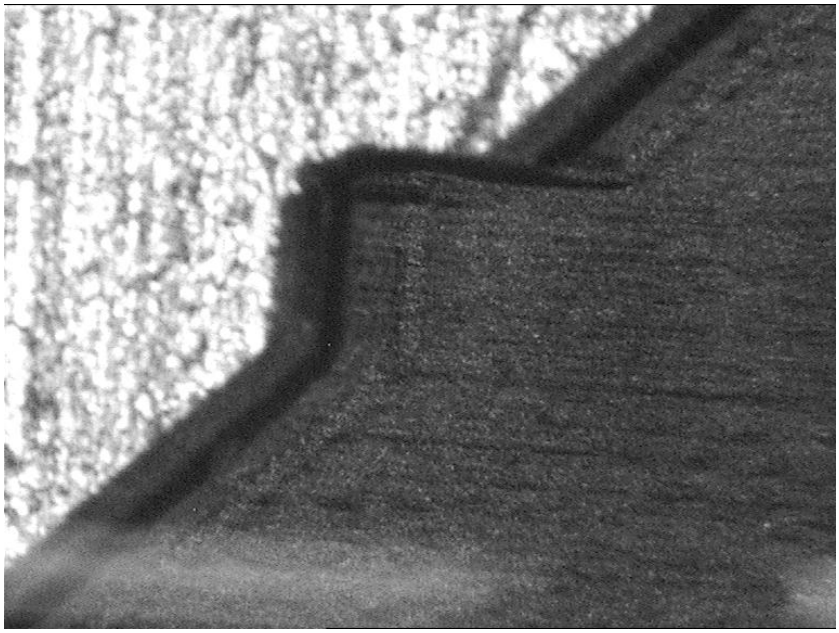

Figure 5.3-5 Draft angle affects vertical profile

The bottom of the laser machined sample structure is focused and shown in Figure 5.3-4. The bottom surface appears to be porous after the machining process. When changing the focus of the optical microscope between the top and bottom surfaces of the sample, the profile of the sidewalls varies accordingly (Figure 5.3-5). Since the direction of view of the optical microscopy is normal to the stainless steel plate which the sample is machined from, the profile change indicates that the sidewalls are not vertical. It can be explained as a draft angle produced by the laser beam. Since the laser beam is focused by a lens at the laser head, the beam actually approaching the sample is in a taper shape. When the cutting depth is deep, 150μm in this fabrication, the upper part of the sidewall will be affected and removed by laser, forming a draft angle.

Sample characterization shows unsatisfied surface roughness and vertical sidewall profile. Therefore, laser machining is tested to be not suitable for fabricating the sidewall of mirror CCR structures and it was decided not to continue further with this fabrication method.

5.3.2 Silicon DRIE approach

5.3.2.1 Review of previous research on DRIE sidewalls fabrication

DRIE is widely used for fabrication of silicon structures with deep high aspect ratio features. Research has reported the methods of improving the vertical sidewalls of deep structures in DRIE.

Normally, sidewalls produce by DRIE have a scalloped appearance due to the BOSCH process, as shown in Figure 5.2-6. One etching cycle is a passivation period that coats the entire surface with a thin layer of polymer, followed by a short isotropic etching process. The etching cycle is repeated to create the anisotropic vertical etch while leaving a scalloped profile on sidewalls, which causes a problem if smooth sidewalls are required. Pike et al. (2004) found that no scallop is left after deep through-wafer etching, it is over etched slowly during the long etching time. Also, they showed that the sidewall morphology varies with the open area Figure 5.3-6. With the same etching parameters, the sidewall in the narrow gap experiences over etching and bottom puncturing while the sidewall in wider area experiences over passivation and vertical striations. It is

concluded that the passivation effect is increased and the etching effect is reduced with lowering the aspect ratio of the gap. The key factor causing this is explained to be the redeposition of the CF2 radicals from the gap bottom to the sidewalls, at the beginning of the etching process in each cycle. In a high aspect ratio gap, less polymer is redeposited to the top part of the gap, causing the polymer thickness in each cycle to be less than the thickness being etched and eventually over etching the sidewall. Likewise, in a lower aspect ratio gap, relatively more polymer material is redeposited, which causes a build-up passivation layer. To improve the sidewall quality, Pike et al. (2004) suggested that a ramping of the etching parameters may be used.

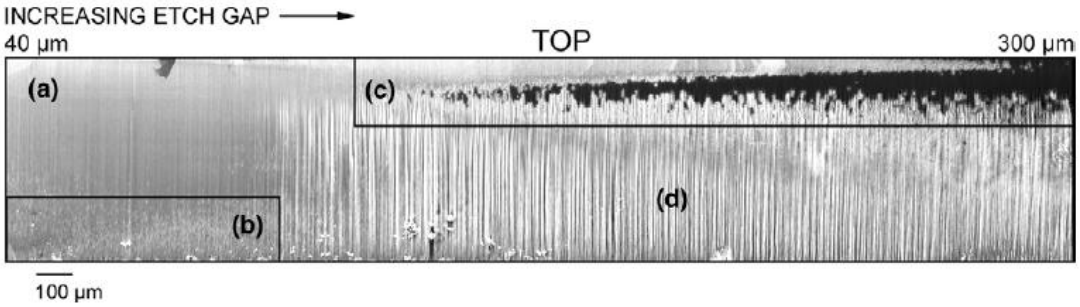

Figure 5.3-6 SEM of the sidewall along an increasing etch gap (Pike 2004)**. (a) over etched; (b) ion puncturing; (c) over passivated; (d) vertical striations.**

Agarwal et al.(2007) introduced a process of fabricating the vertical mirrors using uniform narrow trench DRIE etch to release a large block of silicon and then using KOH:IPA for anisotropic wet polishing. Good surface smoothness and angle accuracy are achieved. However, the process of lithography is very expensive as it requires multiple masks for different layer processes.

A simpler and more economic DRIE approach is looked for. Vertical striations and over passivation are the main problems to address if DRIE needs to be applied in the large open area, like a CCR fabrication. Vertical striations are due to incomplete removal of passivation (Le et al. 2009). Therefore, enlarging etching/passivation ratio is suggested to ensure the through wafer etch as well as balancing the redeposition of passivation layer.

5.3.2.2 Process Details

The process details of fabricating 400μm deep silicon sidewalls are as follow. The MicroChem SPR 220 photoresist is spin coated at 2500rpm, aiming to form a robust layer of 9μm. Relatively thick photoresist is required in this fabrication since it needs to stand against the long-time of DRIE. The photoresist is then soft baked for 90s at 105°C. After 45s UV exposure in the Cannon PLA-501FA mask aligner, the post exposure bake is carried out for 90s at 105°C. Then TMAH MF26-A developer is used to develop the pattern for 200s.

A group of DRIE parameters is experimentally obtained to get a near-vertical sidewall profile. While the pressure of 94mT, the coil power of 600W for both etching and passivation, platen power of 12W are set to be fixed, variations of etching/passivation time ratio are tested to see its effect on the sidewall morphology.

5.3.2.3 Silicon DRIE Result

Before the DRIE starts, the patterned photoresist is checked in SEM (scanning electron microscope) (Figure 5.3-7). The thickness of the photoresist layer is measured to be 17μm, which is thick enough for a through wafer DRIE.

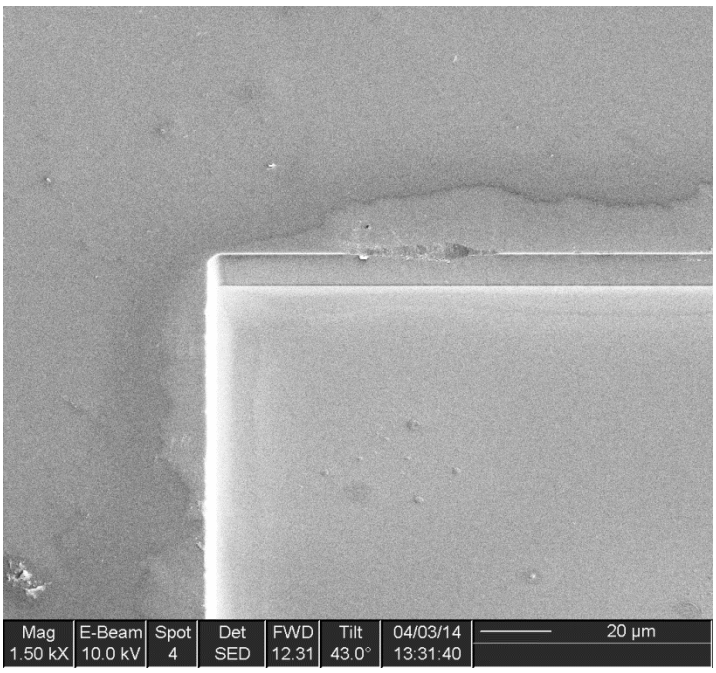

Figure 5.3-7 SPR220-7 photoresist checked in SEM. 17um thickness is measured

In the first variation of DRIE, 3s etch and 1.8s passivation was used for 80min process. The fabrication result is shown in Figure 5.3-8. The etching thickness is measured to be 152μm in SEM. The etch rate is calculated to be 1.9μm/min, which is slower than that of a regular through wafer etch, tested to be 2.7μm/min. Vertical striations are found at the lower part of the sidewalls, which is similar to the low aspect ratio situation illustrated in Figure 5.3-6 (d). Also, micro grass occurs at the bottom of the structure. The formation of micro grass is because that excessive polymer was deposited during the passivation cycle which was not

being removed during the successive etch cycle (Agarwal et al. 2007). It can slow down the etch rate and even terminate the etch process.

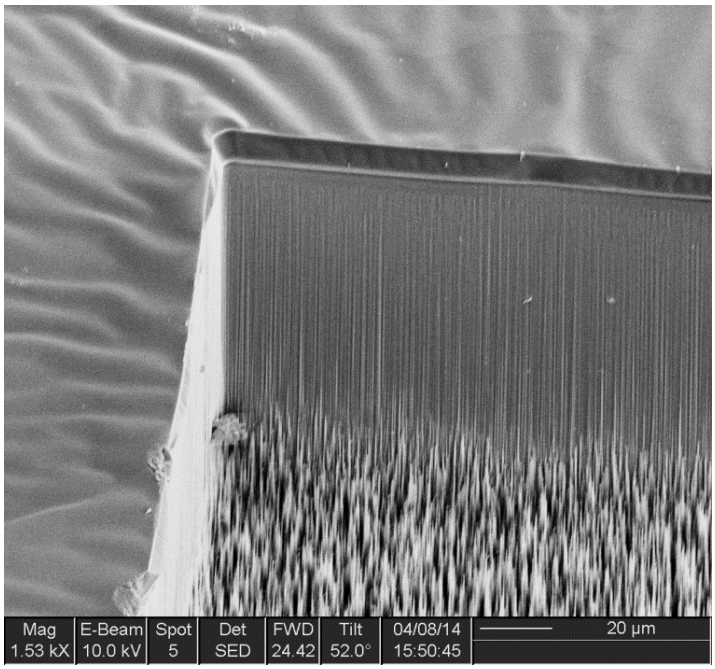

Figure 5.3-8 SEM of DRIE with etch/passivation: 3s/1.8s

Therefore, shorter passivation is required in order to prevent the present of micro grass. In the second variation of DRIE, 3s etch and 1s passivation was used for 180min process. As shown in Figure 5.3-9, the result is clear of micro grass. The etching depth is measured to be 536µm hence the etch rate is 2.98µm/min, which is much higher than that in the first variation. 6µm of photoresist remains while about 25um Si is left after the DRIE. However, the sidewall profile is not kept vertical. Undercut occurs on the top part of the sidewalls, which is caused by the excess etch/passivation ratio. More sideway etch is processed than passivation in each cycle, leading to an accumulated over etch.

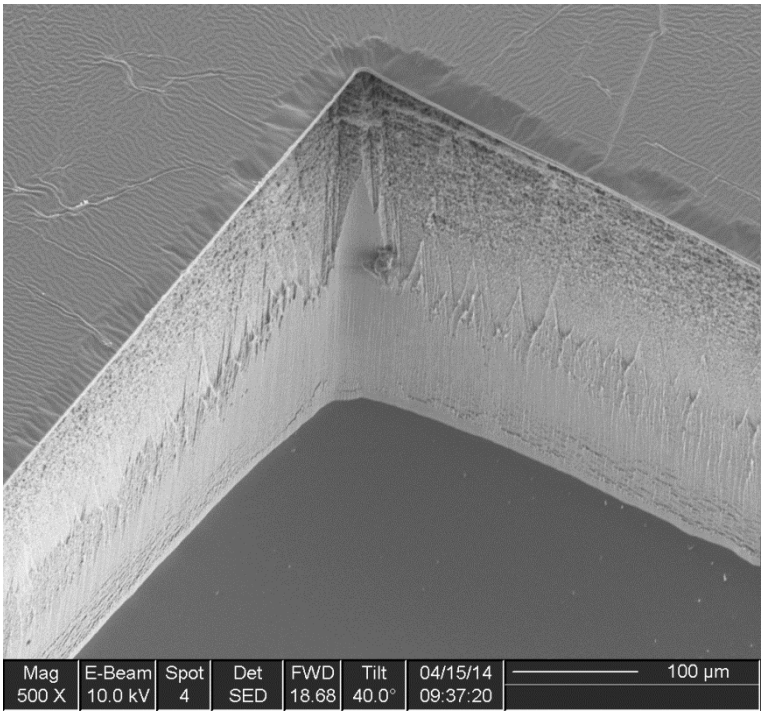

Figure 5.3-9 SEM of DRIE with etch/passivation: 3s/1s

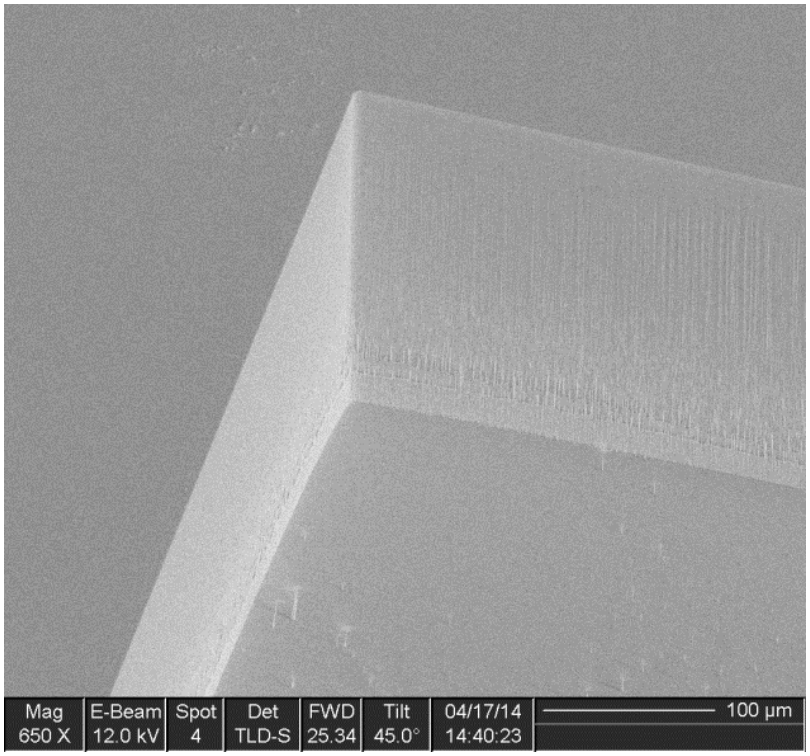

Figure 5.3-10 SEM of DRIE with etch/passivation: 3s/1.5s

A third variation is made to improve the etch/passivation ratio. A cycle of 3s etch and 1.5s passivation is repeated for 180min. It can be seen in Figure 5.3-10 that the result has similar etch depth with that of the second variation. Also, the sidewall profile is largely improved, which is due to a balanced etch/passivation ratio.

The fabrication results above show that silicon DRIE approach is capable of fabricating vertical sidewalls in a large open area by optimizing the DRIE parameters. The sidewall roughness of several optimized samples is measured in Alicona. The surface morphology under 100 times magnification is shown in Figure 5.3-11. The void on the figure is due to the strong reflection of some individual spots, causing the absence of those data in the optical metrology output. The average RMS surface roughness is measured to be 109.8 nm. Wet etch polishing can be considered to achieve a better optical surface finish as discussed previously.

Figure 5.3-11 Surface morphology of an optimized sidewall produced in DRIE

5.3.3 SU-8 photolithography approach

Most of the vertical micro mirrors are made either from silicon technology or from the SU-8 process. The silicon fabrication technology with precise profile and surface result is however considerably complex and costly (Agarwal et al. 2007b). Oppositely, SU-8 is more likely to form smooth and deep vertical surfaces due to its material nature and the principle of photolithography. Moreover, as the SU-8 photolithography is a process added onto the substrate, it is more flexible and economical. The feasibility of fabricating vertical and smooth sidewalls with SU-8 photolithography is analysed in this section.

5.3.3.1 Introduction of SU-8 sidewalls fabrication

SU-8 is a type of photoresist commonly used for producing thick photoresist layers up to 1000μm (Lee et al. 2007). It is highly sensitive to UV, e-beam or x-ray and can produce photon generated acid to form cross-linked structures. SU-8 can work in the temperature up to 250°C before it turns black. Although a CCR fabricated with SU-8 cannot withstand extremely high temperature application, it can be used in most of the radiation environments as SU-8 has shown good radiation resistance (Key et al. 2004,Shea 2011).

SU-8 components like gears (Lee et al. 2007), electroforming moulds (Wei et al. 2008) and supporting structures (Chiu et al. 2009, Lee & Park 2010) have been successfully made. Due to its versatility and the principle of the near-UV

photolithography process, thick SU-8 structures with smooth and vertical sidewall have been considered to be employed in microwave and optical applications. Jiang et al. (2005) fabricated SU-8 Ka-band filters with 700μm sidewall using quartz mask UV lithography. Sum et al. (2003) used direct proton beam writing technique to fabricate waveguides, which is mask less and rapid.

Coating with metal is typically required for optical application as cross-linked SU-8 is almost transparent. Aluminium, silver and gold are suggested to be the most suitable materials for mirror coating (Zappe 2010). Gold has a plasma frequency in the violet (496nm), which makes gold less reflective for short wavelength. However, due to its stable chemical property, gold is suggested to be unparalleled for reflection at long wavelengths.

A few advantages of the SU-8 approach can be seen. With the SU-8 approach, more flexible sidewall structures can be built out of the plane. It is less equipment dependent comparing with the silicon approach. Because of the principle of photolithography that UV light is used to define the pattern edge, it should be much easier to produce vertical and smooth sidewall theoretically.

5.3.3.2 Fabrication process details

A mask with the pattern in Figure 5.3-12 is used to test the feasibility of the photolithography process, which is carried out on a Cannon PLA-501FA mask aligner.

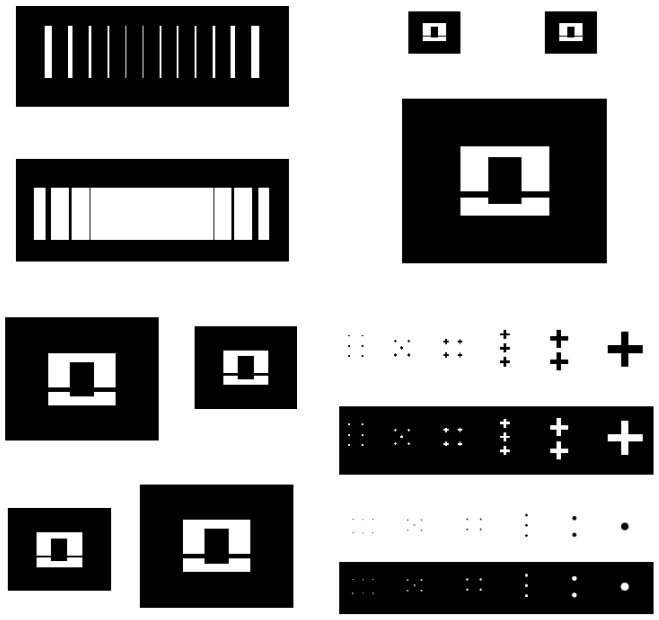

Figure 5.3-12 A mask used for SU-8 photolithography

The process details are depicted as follow. A material from MicroChem called Omnicoat is first coated on a cleaned substrate for 17nm. Its purpose is to provide a sacrificial layer for the SU-8 structure to be stripped off. Then 500μm SU-8 2150 is spin coated at 1200rpm. The softbake is carried for at 95°C for 120min on a hotplate. Gradually cooling down is ensured to reduce the risk of cracking. Then the photoresist is exposure to UV with 350nm filter, followed by straightaway post-exposure bake and development using Microposit EC solvent. Finally, MF-319 is used to lift off the SU-8 structure by etching Omincoat. Hard bake is an optional process at the very end of the photolithography which cures the material for the application involving regular thermal processing.

5.3.3.3 Sidewall Verticality Control

Although the principle of photolithography that using the straight light ray to define the edge of the pattern should, in theory, lead to a vertical sidewall, a tapered sidewall is commonly resulted, especially for thick structure. This is mainly because of the absorption of UV light by the SU-8 during its propagation. A filter is usually employed to filter out the bandwidth that is more absorbable to SU-8 (Lee 2008).

Also, the length of soft bake has an effect on the profile verticality. To produce vertical sidewalls, SU-8 is required to have high transparency to UV before the UV exposure (Jiang et al. 2005). A longer soft bake is proved to deteriorate the transparency property according to their result. However, if the soft bake is too short that excess solvent remains in the SU-8, the diffusion of photon generated acid will cross link unexposed area which subsequently reduces the profile verticality (Becnel 2004).

Therefore, in the initial recipe, soft baking time is set to be 120min at 95°C while 50s of UV exposure is carried out with a filter mask applied to filter out the wavelength below 350nm. The fabrication results of this recipe are shown in Figure 5.3-13 and Figure 5.3-14.

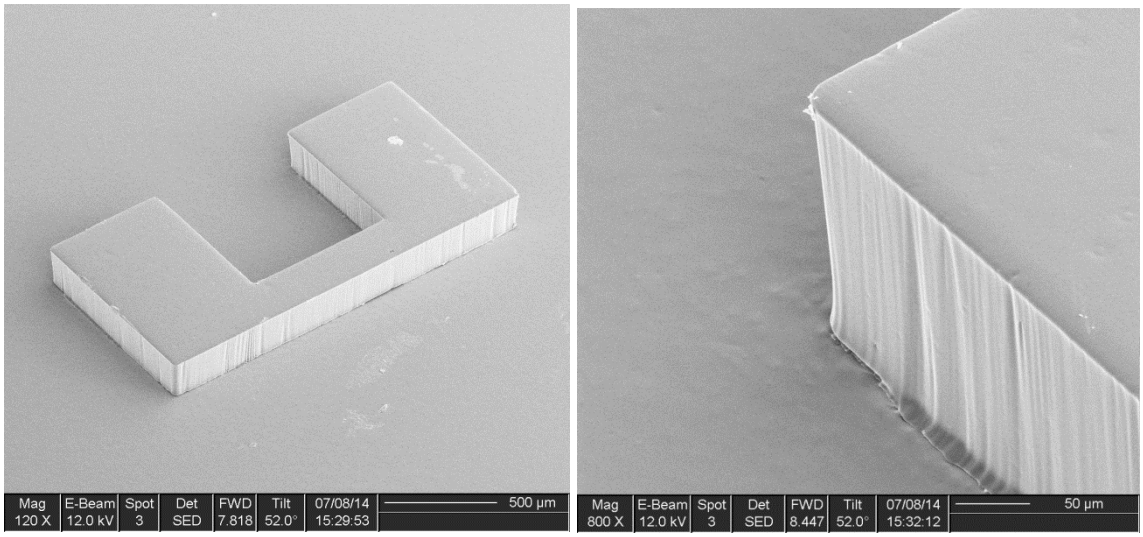

Figure 5.3-13 SEM view of the negatively tapered profile

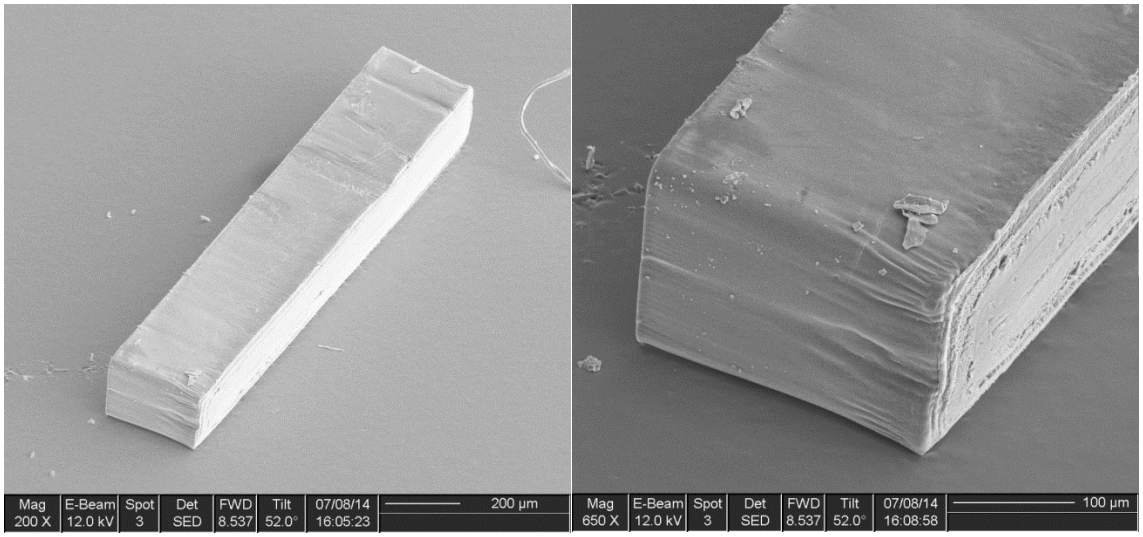

Figure 5.3-14 SEM view of a bar structure lying on its side with a tapered profile

The thick SU-8 structures are measured to have a thickness of 230µm. Negatively tapered sidewall profile is found in structures with different geometry. Since SU-8 is a negative photoresist, the reason can be explained as its insufficient UV exposure. Therefore, the exposure time is increased to get the

improved vertical sidewall profile. 100s and 200s UV exposure time are tested respectively.

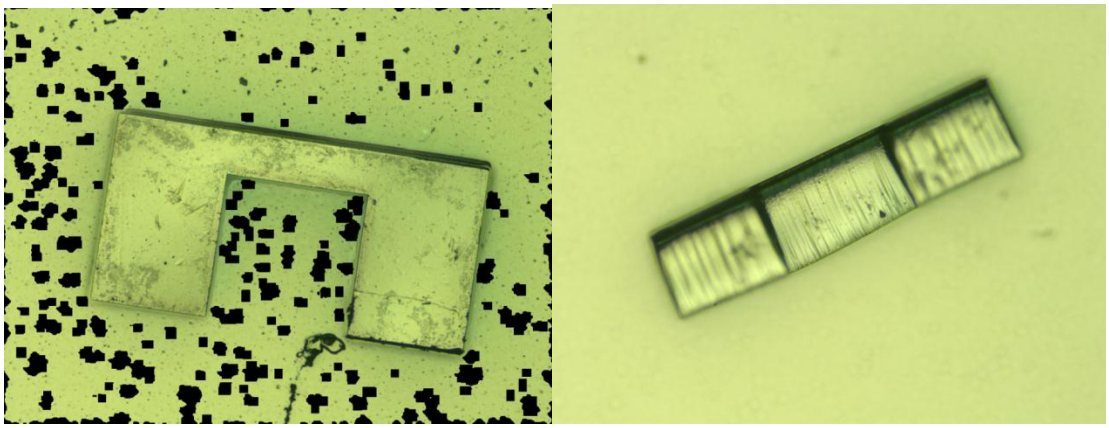

Figure 5.3-15 Alicona image of the 100s exposed structure

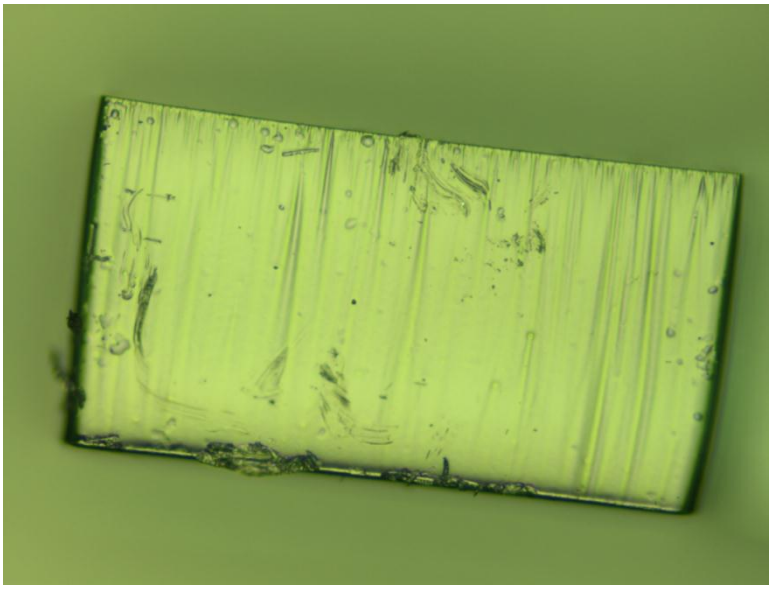

Figure 5.3-16 A close end surface view of the 100s exposed structure

Figure 5.3-15 and Figure 5.3-16 show a 100s UV exposed SU-8 structure observed in Alicona. The end surface view provides the detail of a slightly tapered sidewall profile. The result of a 200s exposed structure is shown in Figure 5.3-17. It can be seen that the sidewall verticality is highly improved.

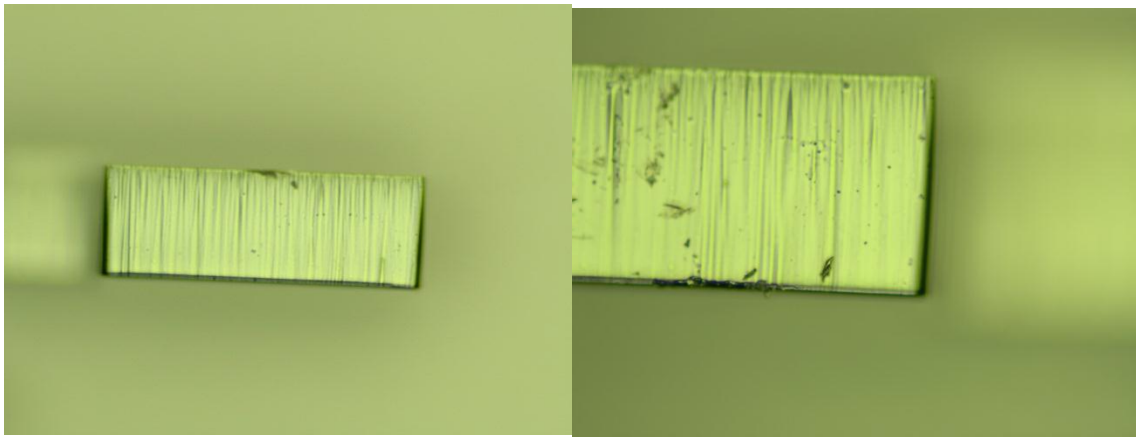

Figure 5.3-17 End surface view of the 200s exposed structure

5.3.3.4 Sidewall Smoothing

Special effort has been put into smoothing the sidewall morphology on UV-exposed SU-8 structures. Similar striated sidewall morphology has been reported previously (Zheng et al. 2010). Longer post-exposure bake (PEB) with high temperature is suggested to produce smooth sidewall. However, strong stress will be induced during PEB, which will cause deformation or even cracks. The cooling procedure after PEB affects the residual stress according to (Williams 2004). The sidewall quality can be largely improved if a cooling rate of 8.5°C/h is used after PEB due to the reduction in residual stress. So far, the smoothest UV photolithography SU-8 sidewall that has been reported has an RMS roughness of 72nm (Zheng et al. 2010)

Vertical striations can be seen on the SU-8 sidewall produced in 5.3.3.3 (Figure 5.3-18 and Figure 5.3-19). The sidewall roughness is between 1.16µm to 2.15µm

measure in Alicona. This is unacceptable for an optical reflection surface. Therefore, sidewall smoothing is processed to reduce surface roughness.

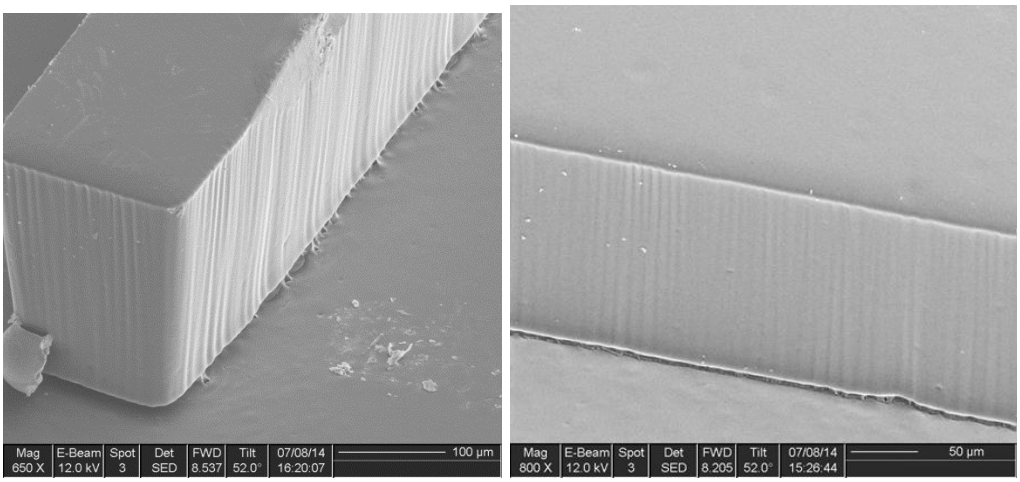

Figure 5.3-18 Sidewall vertical striations

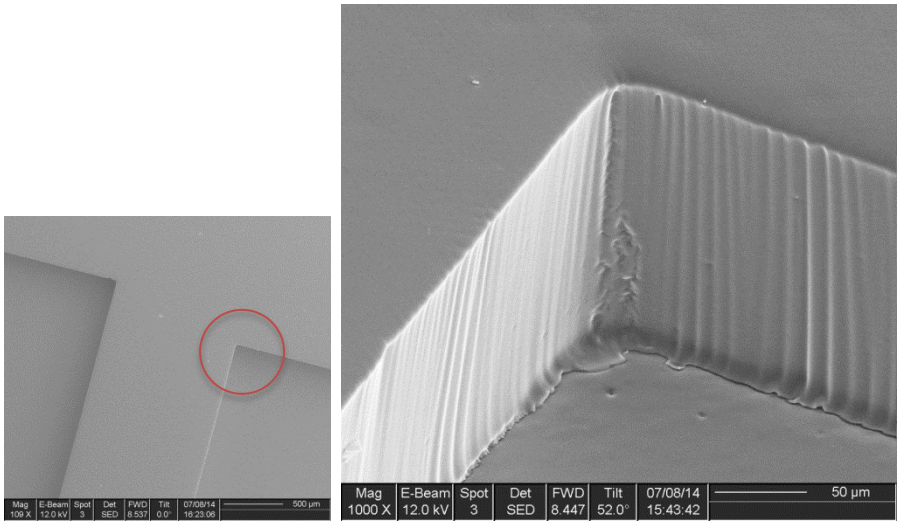

Figure 5.3-19 Vertical striations in a corner

According to the paper of Zheng et al.(2010), the appearance of those striations are mainly affected by the PEB conditions (baking temperature and time). It was stated that there is a thin layer of partially cross-linked SU-8 within the interface between exposed and unexposed region. PEB with longer time and higher

temperature can enhance the diffusion rate of photon generated acid, which help the cross-linking process to have a more evenly distribution, in return producing a smoother sidewall.

Therefore, similar PEB processes at a higher temperature for longer times are undertaken with varying recipe parameters, as listed in Table 5.3-1, to test for an optimized sidewall smoothness. Images of the results are shown in Figure 5.3-20.

Table 5.3-1 Recipes tested for sidewall smoothness

Recipe	**V1**	**V2**	**V3**
Soft bake	95°C 150min Cooled overnight	95°C 180min Quick remove	100°C 180min Cooled overnight
UV Exposure	200s	250s	250s
PEB	107°C 3h40min Natural cooling	107°C 3h40min Cooled slowly	117°C 3h40min Natural cooling
Development	45min without agitation	40min with ultrasonic cleaning	40min with ultrasonic cleaning

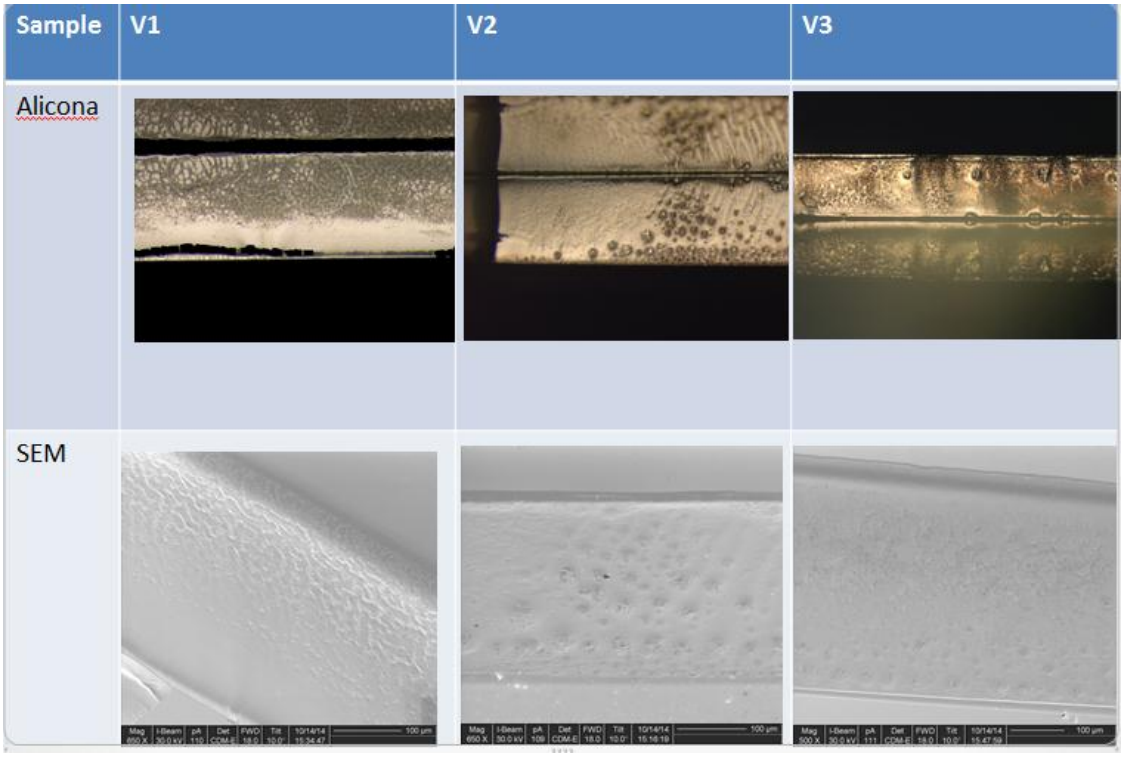

Figure 5.3-20 Alicona and SEM images of test fabrication results

It can be seen from Figure 5.3-20 that vertical striations are eliminated by adopting the increased PEB temperature and time. Sample from V1 has better surface flatness and smoothness while V2 and V3 have more lumps and wrinkles. The difference between V1 and V2 shows the importance of slowly cooling after PEM. Also, agitation during the development causes more surface roughness in V3 than V1, which can be due to the increased damage from the developer.

Adjusted to have a slower cooling procedure, recipe V4, as listed in Table 5.3-2, is processed to have an optimized result. The fabrication result is shown in Figure 5.3-21 and Figure 5.3-22. Very smooth sidewalls are achieved and the

surface RMS roughness is measured in Alicona to be 75nm, which is close to the result reported in the literature.

Table 5.3-2 Optimized SU-8 Photolithography recipe

Recipe	V4
PB	95°C 165min Cooled slowly overnight
Expose	250s
PEB	107°C 3h40min Cooled slowly overnight
Development	45min without agitation

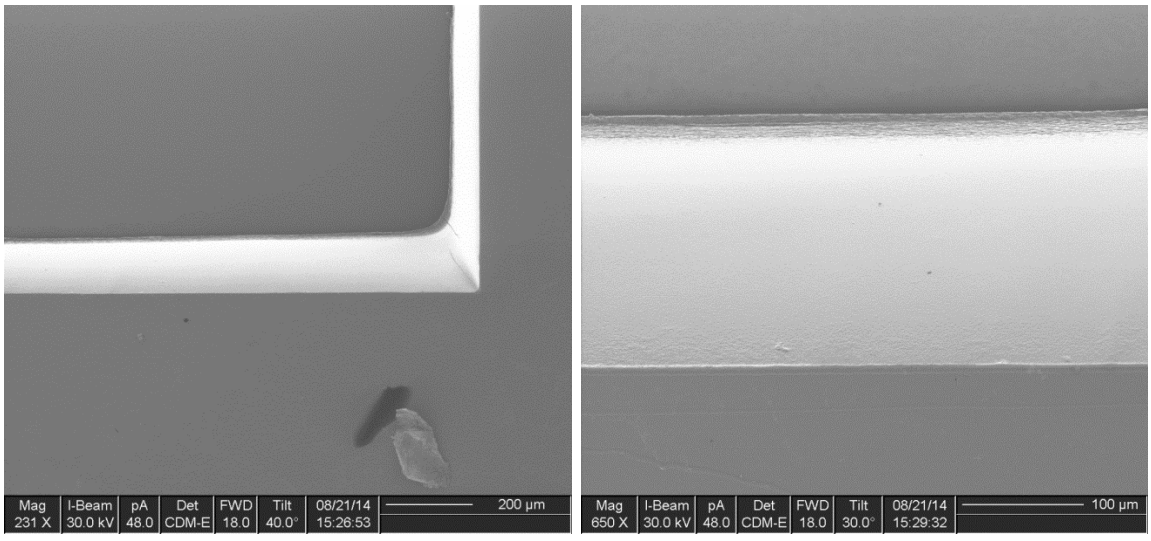

Figure 5.3-21 SEM image of optimized SU-8 sidewalls

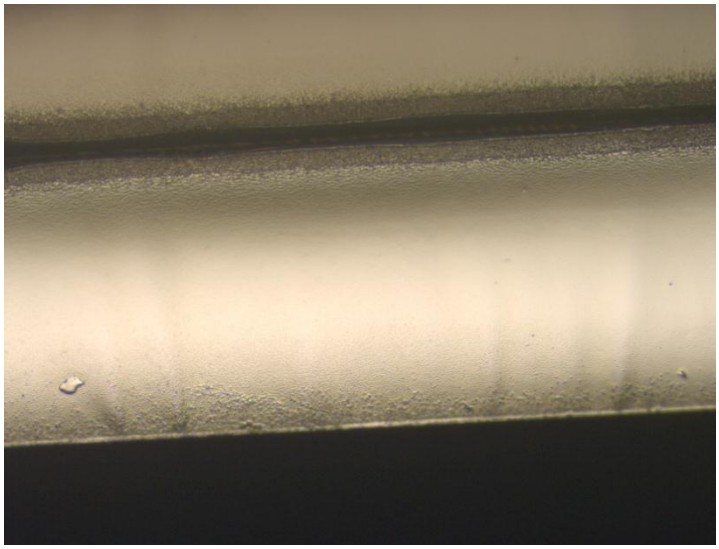

Figure 5.3-22 Alicona image of an optimized sidewall

5.3.4 SU-8 casting with PDMS mould approach

5.3.4.1 Principle of the approach

Although improvements in surface roughness can be achieved by optimizing the post exposure bake, direct moulding of the SU-8 could offer an alternative route to even smoother surfaces. Polydimethylsiloxane (PDMS) is a flexible material that turns into a stable and elastic solid state after curing. Due to its flexibility and reusability, PDMS moulding has been used in many MEMS fabrication processes (Hassanin & Jiang 2010, Le et al. 2009). Using this method, PDMS mould can transfer the sidewalls of a micro corner to an SU-8 structure without the need of carefully controlled lithography process. Diced silicon chips with good edge surface are used to be the core for mould making.

5.3.4.2 Fabrication procedure

The fabrication procedure is shown in Figure 5.3-23. To make the PDMS mould, (a) 500μm diced thick silicon chips with clean and undamaged edge surface are selected using microscopy. Two of them are placed closely but in a stagger position on a cleaned silicon wafer in order to form a pair of smooth sidewalls made of their edge surfaces. Then isopropyl alcohol (IPA) is used to gently fix the chips onto the wafer by utilizing the vacuum it forms when quickly vaporized on a hot plane. (b) Two thin sticks with flat end surface are glued to stand on each of the chips, leaving channels in the mould for SU-8 to flow. (c) After finishing assembling the core, a heavy metal mould holder is placed on the wafer to enclose the core. Then the PDMS mixture is poured in the holder and left to be cured.

Once the PDMS mould is cured, (d) it is separated from the mould holder and the core. After putting the mould on a clean wafer, (e) SU-8 can then be casted into one channel using a syringe. (f) Excess softbake, UV exposure and PEB are carried out to ensure the SU-8 is completely cross-linked. Finally, the PDMS mould is peeled off slowly, releasing the SU-8 replicate which is identical to the core structure shown in Figure 5.3-23 (a).

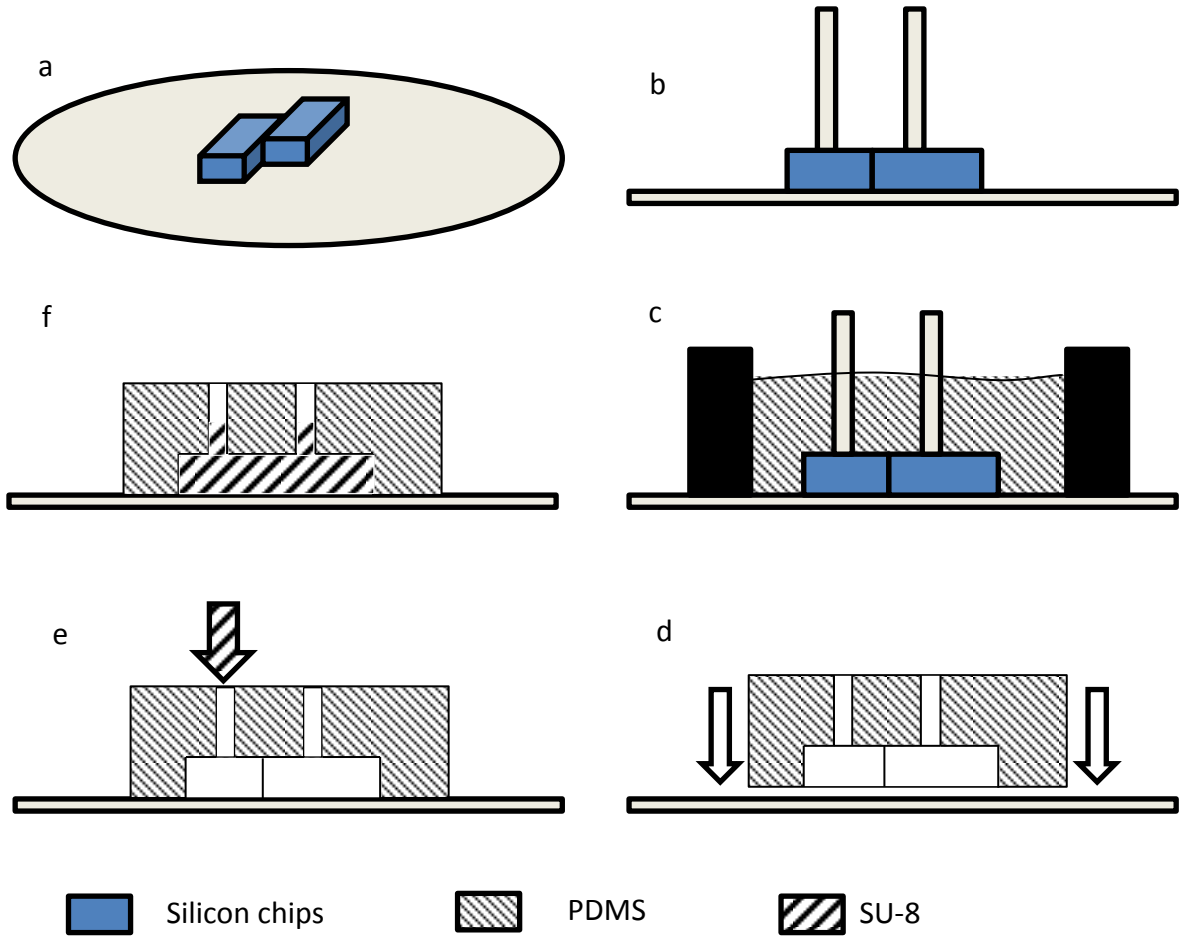

Figure 5.3-23 Schematic of fabrication procedure of PDMS moulding

5.3.4.3 Results

A diced silicon edge surface is viewed in Alicona (Figure 5.3-24). Although there are scratches in the surface, the surface area roughness is measured to be 128.5nm. Figure 5.3-25 shows the sidewall of the PDMS mould. It copies the scratches while adding some tiny bumps and hollows into the morphology.

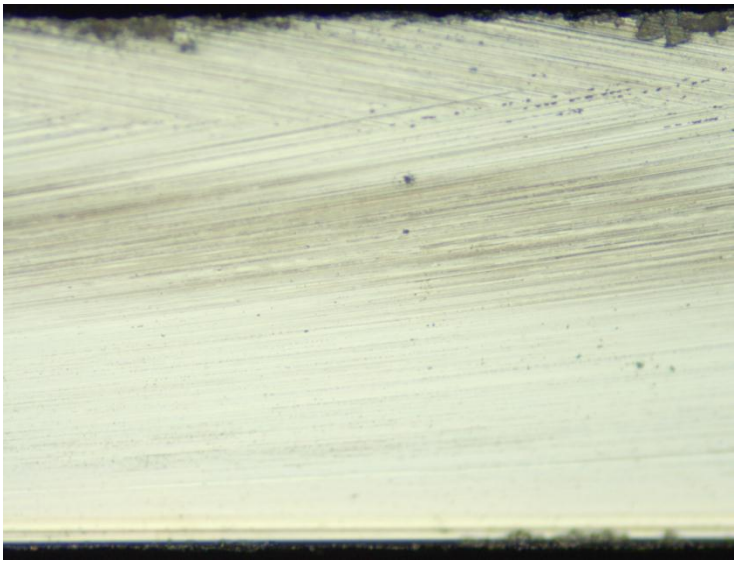

Figure 5.3-24 Edge surface of a diced silicon

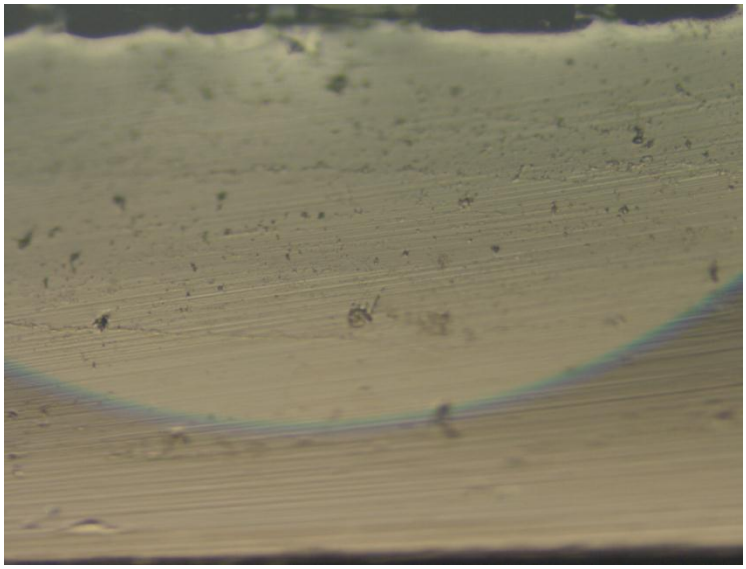

Figure 5.3-25 Surface morphology of the PDMS replication

The SU-8 sidewalls are shown in Figure 5.3-26. A generally smooth surface is achieved, whose surface area roughness is measured to be 116.5nm. This result is very close to the roughness of the silicon edge surface, which proves that the PDMS moulding successfully transfers the surface morphology from the silicon core to the SU-8 structure. If better core surfaces can be obtained, the quality of

the SU-8 sidewall can be improved equally and so this type of direct moulding of SU-8 shows promise for producing a micro CCR structure.

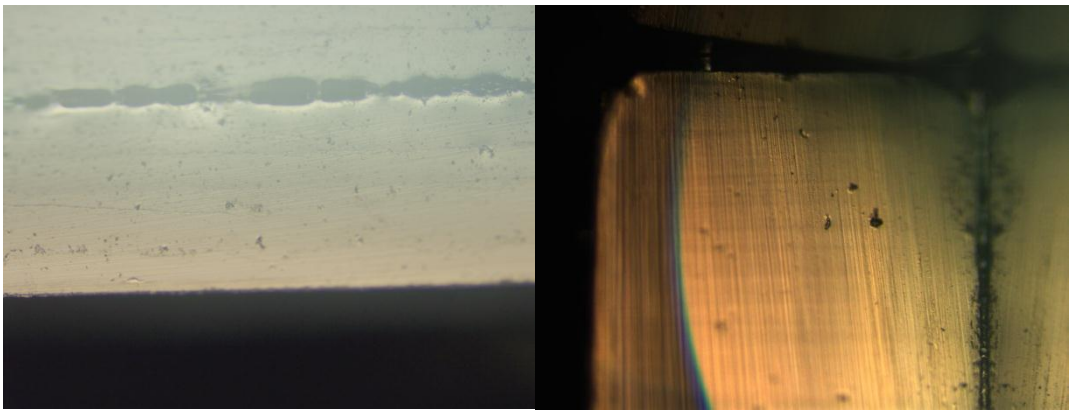

Figure 5.3-26 SU-8 sidewall surface viewed in Alicona

5.3.5 Summary of micro CCR fabrication

Four different approaches of micro CCR fabrication have been tested and analysed.

The laser machining approach provides a fast and accessible way of material removal. However, because the removal is based on the thermal effect caused by an intermittently powered and focused laser spot, the fabrication result presents a rounded contour, bumpy bottom surface, and a sidewall with a draft angle. Therefore laser machining approach is not suitable for fabricating the sidewalls.

The silicon DRIE approach is tested to solve the problem of sidewall over passivation and vertical striation in large open area. Vertical profile and surface striations are controlled by changing DRIE process parameters. Largely improvement is achieved in the optimized fabrication, which shows the capability of DRIE in micro CCR fabrication.

The SU-8 photolithography approach is limited by the result of tapered profile and sidewall striations. Taper profile is corrected by increasing the UV exposure dose with the use of a filter mask and a balanced softbake time. The improvement method for the sidewall smoothness is concluded from the literature, which is to have a PEB with higher temperature and longer time and to be slowly cooled down afterward. A fabrication result with 75nm sidewall roughness is achieved which is comparable with the best result shown in the literature.

A novel approach of employing PDMS micro moulding is demonstrated with SU-8 casting. The process can replicate the surface morphology from a core with smooth vertical sidewalls to the SU-8 structure without the need of carefully controlled photolithography process. Successful replication has been proved in the micro moulding, which produces an SU-8 structure with sidewall roughness of 116.5nm.

5.4 Discussion and plans of the sensor device fabrication

Among the feasible approaches discussed above, SU-8 photolithography provides the best surface result of sidewall fabrication, though a little rougher than the fabrication specification. Released SU-8 sidewalls can be attached to the paddle fabricated in the silicon process or micro electroforming to form a CCR sensor device. However, the attachment of released SU-8 to a paddle can be an issue due to the instability and inaccuracy that may be introduced.

In contrast, PDMS moulding is very flexible in that it can be built on top of any smooth substrate whilst providing a perfect verticality and a reasonable sidewall roughness. The moulding result can be improved by using better core structures. Therefore, different to the SU-8 photolithography approach, PDMS moulding can have the paddle and the SU-8 sidewalls tightly bounded and accurately positioned. The drawback is that the mould making process is not suitable for batch fabrication. Also, the core arrangement requires millimetre core structure to be used, which reduces the potential of scaling down the device.

Silicon DRIE approach has been proved by previous research that it can fabricate high standard micro CCR device. Since it is very expensive and complex, simplified DRIE in the large open area is shown in this study that it is also feasible in CCR sidewall fabrication. This can perfectly collaborate with the SOI paddle fabrication process to form an entire sensor device.

Therefore, a possible plan is to fabricate the micro CCR sensor using DRIE on a single SOI wafer, as depicted in Figure 5.5-1. Both sides of a SOI wafer are processed with photolithography (a) using two different masks. The mask has to be aligned to <1 1 0> orientation of the wafer to enable to following wet etch polishing. Then the DRIE is carried out for both sides until the oxide layer is reached (b and c) to define the paddle resonator and vertical sidewall with relative smoothness. The surface of the device layer is sealed with thermal tape while the handle layer is wet etched using KOH:IPA mixture (d). This process finely polishes the sidewall because the mixture etching rate in crystal plane <1 0 0> is much larger than that of <1 1 0> (Agarwal et al. 2007). Hence the wet etch can quick smooth the sidewall without affecting its verticality. Finally, the oxide layer is etched by HF to release the paddle, which is much more straightforward than the release process described in 5.2.1 owed to the large open space at the back.

5.5 Conclusions

Different approaches of fabricating the paddle resonator and CCR structures are tested and attempts are made to optimize them. The feasibility of each approach is analysed which leads to a final fabrication plan with DRIE process on a single SOI wafer with wet etch polishing. Although the final fabrication is not carried out due to the limited accessibility of DRIE facilities, the technical difficulties in solving the potential problems are addressed and optimization solutions are provided respectively.

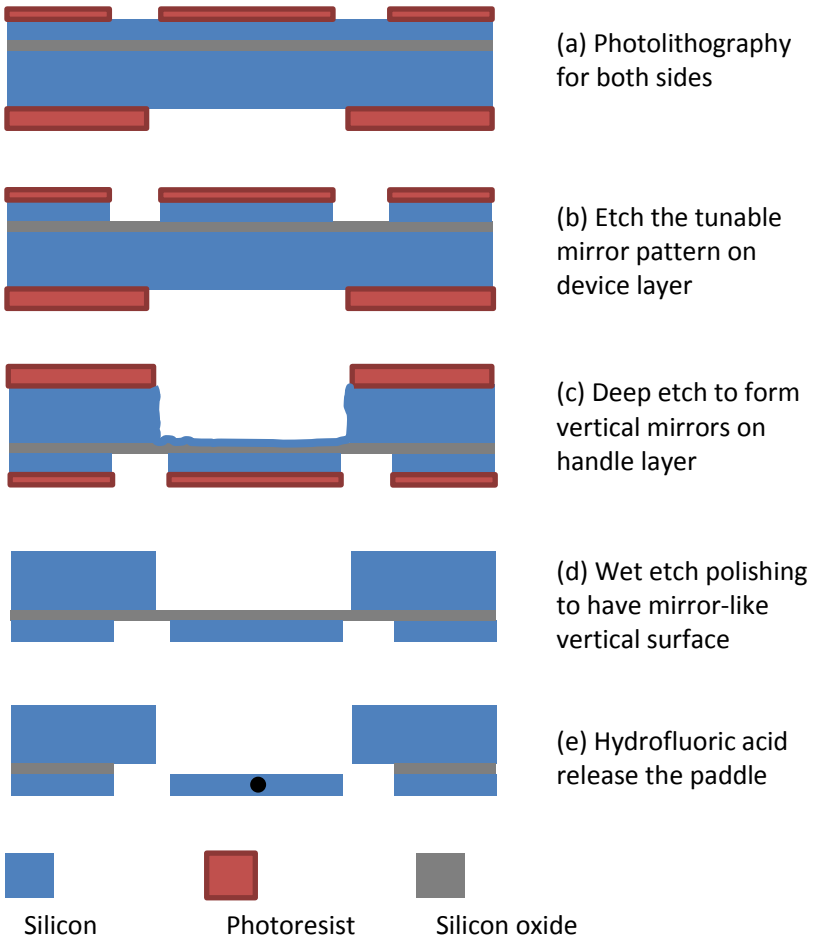

Figure 5.5-1Fabrication process of micromachining CCR sensor on SOI wafer

Chapter 6: Conclusions and Future Work

6.1 Conclusions

This thesis presents the development of a remote optically actuated and interrogated passive resonant sensor with micro CCR structure, which has the potential to be used in extreme environment applications. In the literature, several researches and techniques have been found reporting on sensing in extreme environments, but most of them are wired sensors or wireless sensing within short distance due to the limitation of their working principles. Therefore, an optically actuated and interrogated sensor was proposed by combining a paddle resonator and a CCR structure, enabling long work distance operation with zero local power requirement and low maintenance.

An optically actuated paddle resonator was introduced and designed. Silicon and nickel were selected to be the paddle materials for prototyping as their operation limits are elevated due to the independence of electric elements in this design. It has been shown that the resonant frequency of the paddle resonator shifts with the change of axial stress. The optical actuation process was mathematically analysed and verified in COMSOL. The result was then used in a dynamic model built with the Lagrangian method. The differential equations were solved in MatLab and the design parameters were optimized to get a paddle tilt angle of 1.5mrad, which is sufficient for the optical interrogation.

An optical interrogation system was designed to detect the returning signal remotely from the same location as the laser sources, utilizing the retroreflection provided by a micro CCR structure. Two principles of the CCR optical interrogation were explained and compared. Detecting the retroreflection was found to be more feasible and suitable for this resonant sensor design than detecting the split beams separation. Returned optical power and mirror curvature were shown to be the two important factors that affect the optical behaviours, which provide guidance for the design parameters selection. The design of the sensor node and the optical actuation/interrogation system were then presented.

The fabrication of the paddle resonator and the micro CCR was carried out. For the paddle resonator, silicon microfabrication on SOI wafer and nickel micro electroforming were demonstrated. Both of them have shown to be feasible for a paddle fabrication. In the SOI microfabrication process, photolithography resolution, notching effect and HF release etching time were found to be the potential problems that need to be addressed, while in the nickel electroforming process, the geometry accuracy and internal stress were the issues that need more control. For the CCR vertical sidewalls fabrication, four approaches have been tested in order to achieve a simple and economic fabrication plan without failing the optical requirements. The result of laser machining approach showed unsatisfied surface roughness and sidewall draft angle due to the large spot size and its principle of material removal. Silicon DRIE approach for fabricating

smooth vertical sidewalls in a large open area was processed and improved by adjusting etch to passivation ratio. If a wet etch polish is followed, the silicon DRIE approach was considered to be capable of providing good fabrication result. SU-8 UV lithography approach was investigated for vertical sidewalls without vertical striations. An optimized fabrication recipe was developed, which achieved a very smooth sidewall with the surface roughness of 75nm. Also, a novel approach of SU-8 casting in PDMS mould was carried out. It was shown to be able to replicate the smooth sidewall morphology from a diced silicon core to the SU-8 structure without the need of carefully controlled photolithography. This approach can produce SU-8 structures with sidewall roughness around 110nm to 120nm. Finally, a possible fabrication plan of the sensor node was designed based on the silicon microfabrication process, which can produce the paddle resonator and CCR sidewalls from the same SOI wafer.

The results of the development work above satisfied the specifications of the sensor system defined in section 1.3. First, the design of the sensor met the goal of avoiding any electronic elements in the actuation and interrogation by using an optical approach. Second, remote actuation with photothermal method was analytically demonstrated to be feasible and it is capable to produce a tilting angle of 1.5 mrad in the optimised paddle structure which is large enough for the detection. Third, the optical interrogation system was designed to achieve the goal of being simple and compact as the interrogating light source and detecting photodiode can be placed in the same place owe to utilising the retroreflection of

a micro CCR. Finally, the fabrication method of the paddle mirror and micro CCR sidewalls were demonstrated and discussed respectively using the materials of nickel, silicon and SU-8, which have shown reasonable mechanical resonance and optical behaviours as expected in the design specifications. This study mainly focused on establishing the preliminary actuation theory and fundamental of the sensor design and fabrication, however, the completed fabrication result and sensor testing was not presented due to the limited accessibility of the DRIE fabrication facility in the given time. Extremely high temperature and radiation resistant materials were also not included in the development stage. But ultimately, it can be developed into a new type of micro sensor system for extreme environments applications with better materials and fabrication techniques. If a different sensor material, for example, silicon carbide is used instead of silicon, the fabrication process such DRIE needs to be reworked to get an optimized sidewall profile and surface finish. This is because that the physical and chemical properties are very different between the two materials, which changes the processes of applying mask materials and etchants (Jiang & Cheung 2009).

Some aspects of this work are applicable to other scenarios. A similar paddle geometry can be adopted in electrothermal actuation where a tilting motion is required, because both actuation principles utilise the thermal expansion introduced force as an actuation force. Also, the method of fabricating SU-8

using PDMS moulding can be applied to replicate thick photoresist structures onto other specified locations to form 3D structures.

6.2 Future work

In this thesis, the actuation and interrogation of the sensor system have been proved to work theoretically. However, the fabrication of the final sensor node is not completed. The designed fabrication plan of the final sensor device in Chapter 5 can be carried out in the future, followed by testing with the actuation and interrogation system designed in Chapter 4.

When designing the paddle resonator, a straightforward geometry with a single material is adopted to simplify the analytical modelling and parameter optimization. To improve the design in the future, bimetallic structures can be involved to achieve a larger paddle deflection. Although this will increase the complexity of fabrication, it can reduce the power consumption in the actuation process.

Since the proposed system has the potential to be used in extreme environments, tests performed under high temperature and radiation can also be carried out. The material of silicon and nickel were used for prototyping and fabrication demonstrating in this study. However, sensor nodes made from other high temperature and radiation resistance materials, like zirconium, can also be

investigated and tested to see the effect of materials when the sensor is operating in extreme environments.

Appendix I: Excel Macro Code for FDM

```
Public dt
Public Kt
Public rho
Public Cp
Public dx
Public dz
Public Q
Public FoM
Public ht
Public alpha

Public Theexp 'thermal expansion

Public MaxRow
Public MaxCol
Public NumCalc

Public Values1() As Double
Public Values2() As Double
Public Values3() As Double

Public dx1

Sub Init()
'
' Macro1 Macro
'
    Worksheets("Sheet2").Cells.ClearContents
    Worksheets("Sheet1").Cells.ClearContents
    Worksheets("Sheet4").Cells.ClearContents

    Worksheets("Sheet5").Activate
    MaxRow = Worksheets("Sheet5").Cells(1, 1)
    MaxCol = Worksheets("Sheet5").Cells(1, 2)
    NumCalc = Worksheets("Sheet5").Cells(1, 3)

    ReDim Values1(MaxRow + 1, MaxCol + 1) As Double
    ReDim Values2(MaxRow + 1, MaxCol + 1) As Double
    ReDim Values3(MaxRow + 1, MaxCol + 1) As Double

    dt = 0.01
    Kt = 163
    rho = 2330
    Cp = 703
    dx = 0.00001
    dz = dx '0.00001
    Q = 15915500
    ht = 5
    alpha = 0.00000415

    dt = (rho * Cp * dx * dx) / (6 * Kt)
    FoM = (Kt * dt) / (rho * Cp * dx * dx)

    Worksheets("Sheet5").Cells(1, 9).Value = dt
    Worksheets("Sheet5").Cells(1, 10).Value = FoM

    Theexp = 0
```

```
'see what each cell represents
   For Row = 1 To MaxRow
      For col = 1 To MaxCol
         Values1(Row, col) = Worksheets("Sheet5").Cells(Row + 4, col)
         Values3(Row, col) = 0
      Next col
   Next Row

'set initial temperatures on sheet 2
   Worksheets("Sheet2").Activate

   For Row = 1 To MaxRow
      For col = 1 To MaxCol
         Select Case Values1(Row, col)
            Case 0
               Worksheets("Sheet2").Cells(Row, col).Value = 20
               Values2(Row, col) = 20
            Case 1 To 19
               TT = 20
               Worksheets("Sheet2").Cells(Row, col).Value = TT
               Values2(Row, col) = TT
            Case Else
         End Select
      Next col
   Next Row

End Sub

Sub Calc()
'
' Macro2 Macro
'
Init

   Worksheets("Sheet1").Activate

For i = 1 To NumCalc

   For Row = 1 To MaxRow
      For col = 1 To MaxCol
         Select Case Values1(Row, col)
            Case 0 'free space
               Tnew = Values2(Row, col)
               'Worksheets("Sheet1").Cells(Row, Col).Value = Tnew
               Values3(Row, col) = Tnew
            Case 1 'sides top
               Tnew = (1 - 4 * FoM) * Values2(Row, col) + FoM * (Values2(Row, col - 1) + Values2(Row, col +
1) + 2 * Values2(Row + 1, col)) + (4 * (ht * dt) / (rho * Cp * dz)) * (Values2(1, 1) - Values2(Row, col)) + (dt *
Q) / (rho * Cp)
               'Worksheets("Sheet1").Cells(Row, Col).Value = Tnew
               Values3(Row, col) = Tnew
            Case 2 'sides left
               Tnew = (1 - 4 * FoM) * Values2(Row, col) + FoM * (Values2(Row - 1, col) + 2 * Values2(Row,
col + 1) + Values2(Row + 1, col)) + (4 * (ht * dt) / (rho * Cp * dz)) * (Values2(1, 1) - Values2(Row, col)) + (dt *
Q) / (rho * Cp)
               'Worksheets("Sheet1").Cells(Row, Col).Value = Tnew
               Values3(Row, col) = Tnew
            Case 3 'sides right
               Tnew = (1 - 4 * FoM) * Values2(Row, col) + FoM * (2 * Values2(Row, col - 1) + Values2(Row - 1,
col) + Values2(Row + 1, col)) + (4 * (ht * dt) / (rho * Cp * dz)) * (Values2(1, 1) - Values2(Row, col)) + (dt * Q)
/ (rho * Cp)
               'Worksheets("Sheet1").Cells(Row, Col).Value = Tnew
```

```
                Values3(Row, col) = Tnew
            Case 4 'sides bottom
                Tnew = (1 - 4 * FoM) * Values2(Row, col) + FoM * (Values2(Row, col - 1) + 2 * Values2(Row - 1,
col) + Values2(Row, col + 1)) + (4 * (ht * dt) / (rho * Cp * dz)) * (Values2(1, 1) - Values2(Row, col)) + (dt * Q)
/ (rho * Cp)
                'Worksheets("Sheet1").Cells(Row, Col).Value = Tnew
                Values3(Row, col) = Tnew
            Case 5 'out corner Top Left
                Tnew = (1 - 4 * FoM) * Values2(Row, col) + FoM * (2 * Values2(Row, col + 1) + 2 *
Values2(Row + 1, col)) + (6 * (ht * dt) / (rho * Cp * dz)) * (Values2(1, 1) - Values2(Row, col)) + (dt * Q) / (rho
* Cp)
                'Worksheets("Sheet1").Cells(Row, Col).Value = Tnew
                Values3(Row, col) = Tnew
            Case 6 'out corner Top right
                Tnew = (1 - 4 * FoM) * Values2(Row, col) + FoM * (2 * Values2(Row, col - 1) + 2 * Values2(Row
+ 1, col)) + (6 * (ht * dt) / (rho * Cp * dz)) * (Values2(1, 1) - Values2(Row, col)) + (dt * Q) / (rho * Cp)
                'Worksheets("Sheet1").Cells(Row, Col).Value = Tnew
                Values3(Row, col) = Tnew
            Case 7 'out corner bottom Right
                Tnew = (1 - 4 * FoM) * Values2(Row, col) + FoM * (2 * Values2(Row, col - 1) + 2 * Values2(Row
- 1, col)) + (6 * (ht * dt) / (rho * Cp * dz)) * (Values2(1, 1) - Values2(Row, col)) + (dt * Q) / (rho * Cp)
                'Worksheets("Sheet1").Cells(Row, Col).Value = Tnew
                Values3(Row, col) = Tnew
            Case 8 'out corner bottom Left
                Tnew = (1 - 4 * FoM) * Values2(Row, col) + FoM * (2 * Values2(Row - 1, col) + 2 * Values2(Row,
col + 1)) + (6 * (ht * dt) / (rho * Cp * dz)) * (Values2(1, 1) - Values2(Row, col)) + (dt * Q) / (rho * Cp)
                'Worksheets("Sheet1").Cells(Row, Col).Value = Tnew
                Values3(Row, col) = Tnew
            Case 9 'in corner top left
                Tnew = (1 - 4 * FoM) * Values2(Row, col) + FoM * ((2 / 3) * Values2(Row, col - 1) + (2 / 3) *
Values2(Row - 1, col) + (4 / 3) * Values2(Row, col + 1) + (4 / 3) * Values2(Row + 1, col)) + ((10 / 3) * (ht * dt)
/ (rho * Cp * dz)) * (Values2(1, 1) - Values2(Row, col)) + (dt * Q) / (rho * Cp)
                'Worksheets("Sheet1").Cells(Row, Col).Value = Tnew
                Values3(Row, col) = Tnew
            Case 10 'in corner top right
                Tnew = (1 - 4 * FoM) * Values2(Row, col) + FoM * ((4 / 3) * Values2(Row, col - 1) + (2 / 3) *
Values2(Row - 1, col) + (2 / 3) * Values2(Row, col + 1) + (4 / 3) * Values2(Row + 1, col)) + ((10 / 3) * (ht * dt)
/ (rho * Cp * dz)) * (Values2(1, 1) - Values2(Row, col)) + (dt * Q) / (rho * Cp)
                'Worksheets("Sheet1").Cells(Row, Col).Value = Tnew
                Values3(Row, col) = Tnew
            Case 11 'in corner bottom right
                Tnew = (1 - 4 * FoM) * Values2(Row, col) + FoM * ((4 / 3) * Values2(Row, col - 1) + (4 / 3) *
Values2(Row - 1, col) + (2 / 3) * Values2(Row, col + 1) + (2 / 3) * Values2(Row + 1, col)) + ((10 / 3) * (ht * dt)
/ (rho * Cp * dz)) * (Values2(1, 1) - Values2(Row, col)) + (dt * Q) / (rho * Cp)
                'Worksheets("Sheet1").Cells(Row, Col).Value = Tnew
                Values3(Row, col) = Tnew
            Case 12 'in corner bottom left
                Tnew = (1 - 4 * FoM) * Values2(Row, col) + FoM * ((2 / 3) * Values2(Row, col - 1) + (4 / 3) *
Values2(Row - 1, col) + (4 / 3) * Values2(Row, col + 1) + (2 / 3) * Values2(Row + 1, col)) + ((10 / 3) * (ht * dt)
/ (rho * Cp * dz)) * (Values2(1, 1) - Values2(Row, col)) + (dt * Q) / (rho * Cp)
                'Worksheets("Sheet1").Cells(Row, Col).Value = Tnew
                Values3(Row, col) = Tnew
            Case 13 'main parts
                Tnew = (1 - 4 * FoM) * Values2(Row, col) + FoM * (Values2(Row, col - 1) + Values2(Row - 1,
col) + Values2(Row, col + 1) + Values2(Row + 1, col)) + 2 * ((ht * dt) / (rho * Cp * dz)) * (Values2(1, 1) -
Values2(Row, col)) + (dt * Q) / (rho * Cp)
                'Worksheets("Sheet1").Cells(Row, Col).Value = Tnew
                Values3(Row, col) = Tnew
            Case 14 'left anchor
                Tnew = (1 - 6 * FoM) * Values2(Row, col) + FoM * (2 * Values2(Row, col - 1) + Values2(Row - 1,
col) + 2 * Values2(Row, col + 1) + Values2(Row + 1, col)) + 2 * ((ht * dt) / (rho * Cp * dz)) * (Values2(1, 1) -
Values2(Row, col)) + (dt * Q) / (rho * Cp)
```

```
                'Worksheets("Sheet1").Cells(Row, Col).Value = Tnew
                Values3(Row, col) = Tnew
            Case 15 'right anchor
                Tnew = (1 - 6 * FoM) * Values2(Row, col) + FoM * (2 * Values2(Row, col - 1) + Values2(Row - 1,
col) + 2 * Values2(Row, col + 1) + Values2(Row + 1, col)) + 2 * ((ht * dt) / (rho * Cp * dz)) * (Values2(1, 1) -
Values2(Row, col)) + (dt * Q) / (rho * Cp)
                'Worksheets("Sheet1").Cells(Row, Col).Value = Tnew
                Values3(Row, col) = Tnew
            Case 16 'left anchor top corner (top side)
                Tnew = (1 - 6 * FoM) * Values2(Row, col) + FoM * (2 * Values2(Row, col - 1) + 2 * Values2(Row,
col + 1) + 2 * Values2(Row + 1, col)) + 4 * ((ht * dt) / (rho * Cp * dz)) * (Values2(1, 1) - Values2(Row, col)) +
(dt * Q) / (rho * Cp)
                'Worksheets("Sheet1").Cells(Row, Col).Value = Tnew
                Values3(Row, col) = Tnew
            Case 17 'right anchor top corner (top side)
                Tnew = (1 - 6 * FoM) * Values2(Row, col) + FoM * (2 * Values2(Row, col - 1) + 2 * Values2(Row,
col + 1) + 2 * Values2(Row + 1, col)) + 4 * ((ht * dt) / (rho * Cp * dz)) * (Values2(1, 1) - Values2(Row, col)) +
(dt * Q) / (rho * Cp)
                'Worksheets("Sheet1").Cells(Row, Col).Value = Tnew
                Values3(Row, col) = Tnew
            Case 18 'right anchor bottom corner (bot side)
                Tnew = (1 - 6 * FoM) * Values2(Row, col) + FoM * (2 * Values2(Row, col - 1) + 2 * Values2(Row
- 1, col) + 2 * Values2(Row, col + 1)) + 4 * ((ht * dt) / (rho * Cp * dz)) * (Values2(1, 1) - Values2(Row, col)) +
(dt * Q) / (rho * Cp)
                'Worksheets("Sheet1").Cells(Row, Col).Value = Tnew
                Values3(Row, col) = Tnew
            Case 19 'left anchor bottom corner (bot side)
                Tnew = (1 - 6 * FoM) * Values2(Row, col) + FoM * (2 * Values2(Row, col - 1) + 2 * Values2(Row
- 1, col) + 2 * Values2(Row, col + 1)) + 4 * ((ht * dt) / (rho * Cp * dz)) * (Values2(1, 1) - Values2(Row, col)) +
(dt * Q) / (rho * Cp)
                'Worksheets("Sheet1").Cells(Row, Col).Value = Tnew
                Values3(Row, col) = Tnew
            Case Else
        End Select
    Next col
Next Row

'For Row = 1 To MaxRow
    'For Col = 1 To MaxCol
        'Values2(Row, Col) = Values3(Row, Col)
    'Next Col
'Next Row

If (i / 100) = Int(i / 100) Then

    Worksheets("Sheet4").Cells(i / 100 + 1, 1).Value = i
    Worksheets("Sheet4").Cells(i / 100 + 1, 2).Value = i * dt

    For j = 1 To 10
        Worksheets("Sheet4").Cells(i / 100 + 1, 2 + j).Value = Values3(13, 1 + j)
    Next j
End If

Values2 = Values3

Next i

For Row = 1 To MaxRow
        For col = 1 To MaxCol
            Worksheets("Sheet2").Cells(Row, col).Value = Values2(Row, col)
            Worksheets("Sheet1").Cells(Row, col).Value = Values3(Row, col)
        Next col
```

```
        Next Row
For col = 2 To MaxCol - 1
Theexp = Theexp + (Values3(13, col) - Values3(1, 1)) * dx * alpha

Next col
Worksheets("Sheet1").Cells(30, 1).Value = Theexp
End Sub
```

Appendix II: MatLab Code for System Dynamic Modelling

```
clear
clc
clf

t0=[0 0.008];  % time range

theta0=0e-8;   % initial angular position
omega0=0e-8;   % initial angular velocity
x0=0e-8;       % initial M position
v0=0e-8;       % initial M velocity

[t,x]=ode45('damp',t0,[theta0,omega0,x0,v0]);

subplot(2,1,1)
plot(t,x(:,1),'r'); %rad, paddle angular displacement
xlabel('time/s')
ylabel('Tilt angle/rad', 'fontsize', 12)

subplot(2,1,2)
plot(t,x(:,3),'b'); %m, M displacement
xlabel('time/s')
ylabel('Paddle deflection/m', 'fontsize', 12)



function xdot=damp(t,x)
%damp is the differential equations for x and theta in the condition of
doubly fixed beam driven by photothermally induced equivalent force.

%Dimension parameters of optimised paddle structure
lp=140e-6; %m, full length of paddle
bp=100e-6; %m, width of paddle
hp=0.3*10e-6; %m, thickness of paddle
ls=4*100e-6; %m, length of supporting beam: one side of the f-f beam
as=40e-6; %m, larger dimension of supporting beam section
bs=0.3*10e-6; %m, smaller dimension of supporting beam section

%Material parameters (Nickel),activate this section for nickel
structure
%rho=8900;    %kg/m^3, density of nickel
%E=219e9;     %Pa, Young's modulus
%vpo=0.31;     %1, Poisson's ratio
%k=90.7;      % thermal conductivity
%c=445;       % specific heat capacity
%alpha=13.4e-6;  %coefficient of thermal expansion
```

```
%Material parameters (Silicon), activate this section for silicon
structure
rho=2330;   %kg/m^3, density of silicon
E=131e9;    %Pa, Young's modulus
vpo=0.27;    %1, Poisson's ratio
alpha=4.15e-6;  %coefficient of thermal expansion
k=163;      %thermal conductivity
c=703;      %specific heat capacity

%Optical parameters
Pl=10*0.005;   %W, laser input power
abr=0.4;    %1, absoption rate
rsp=1/4*0.002;  %m, laser spot radius

%damping
Q=300;   %quality factor

%calculation of parameters
L=2*ls+bp;  % full length of the doubly-clamped beam
M=rho*bp*hp*as/2;    %kg     for as is the width of supporting beam;
mass of the part suspended rather than the cantilever
m=rho*lp*bp*hp-M;   %kg, paddle mass
l=lp/2-lp/14*3; %distance between center of M and center of m
g=9.8;    %m/s^2, gravity acceleration
beta=1/3-0.21*bs/as*(1-bs^4/as^4/12); %for as>=bs;
G=E/(2*(vpo+1));    %Pa, Shear modulus
kt=2*beta*as*bs^3/ls*G;     %for as>=bs;torsional spring constant for 2
supporting beams together
kb=2*E*as*hp^3/ls^3;    %for as is the width of supporting beam;
bending spring constant for 2 supporting beams together
I=as*bs^3/12;       %area moment of inertia of the supporting beam
At=lp*bp+ls*2*as;   %m^2, area of top surface
Ip=1/12*m*lp^2+m*l^2; %moment of inertia of paddle
cb=(M*kb)^0.5/Q;    %coefficient of damping for beam pistion motion
ct=(Ip*kt)^0.5/Q;    %coefficient of damping for torsional motion

%Just for frequency proof
Jp=m*(hp^2/12+0.165*lp^2);    %Moment of inertia 550/150=11/3, same
with Ip
f1=1/(2*pi)*(kt/Jp)^0.5;    %Natural frequency of torsional mode
f2=1/(2*pi)*(kb/(m+M))^0.5;  %Natural frequency of the
piston/translation mode

fdrive=f2; %Hz, set resonance driving frequency to translational mode

omega=fdrive*2*pi;   %Hz
miu=(2*k/(rho*omega*c))^0.5;    %thermal diffusion length

Iin_0=Pl*abr/(pi*rsp^2);    %Intensity unfocused at input power of Pl

%   time constants
mechtimeconstant=1/f2;
Gth=as*bs*k*2/ls;
Cth=(M+m)*c;
timeconstant=(M+m)*c/2*ls/(k*as*bs);
```

```
%   calculate equivalent force
Tlumped=Iin_0*At/(Gth*(1+omega^2*timeconstant^2)^0.5);
Tlumpedsteady=Iin_0*At/Gth;
Tlumpedhighfrequency=Iin_0*At/Cth/omega;

Tthin=1.414*miu*Iin_0/4/k;

expansionlumped=alpha*Iin_0*At*(bp+ls)/(2*(k*as*bs)/ls*((1+omega^2*time
constant^2))^0.5);
expansionlumped2=alpha*Tlumped*(bp+ls);
expansionthin=Tthin*alpha*L;
bendingmoment=2*E*expansionthin*I/bs/L;
expansionFDM=2.3e-12;

amplitudelumped=(expansionlumped*3*L/8)^0.5;
amplitudethin=(expansionthin*3*L/8)^0.5;
amplitudethick=bendingmoment*L^2/(16*E*I);
amplitudeFDM=(expansionFDM*3*L/8)^0.5;
amplitudeFDM2=2*L/pi*(expansionFDM/L+(expansionFDM/L)^2/2)^0.5;

Flumped=192*amplitudelumped*(E*I)/L^3;
Fthin=192*amplitudethin*(E*I)/L^3;
Fthick=192*amplitudethick*(E*I)/L^3;
FFDM=192*amplitudeFDM*(E*I)/L^3;


Fdrive=1/2*(Flumped+Flumped*sin(omega*t));


%   The equations were
%   m*l*x''*cos(theta)-
(m*l^2+4/3m*l^2)*theta''+m*g*l*cos(theta)+kt*theta=-ct*theta'
%   (M+m)*x''+m*l*theta''*cos(theta)-m*l*(theta')^2*sin(theta)+k*x=-
cs*x'+F0*sin(omega*t)

%   use x(1) for theta, x(2) for theta', x(3) for x, x(4) for x' in
here
% xdot(1) theta', xdot(2) theta'', xdot(3) x', xdot(4) x''

A=-ct*x(2)-kt*x(1)-m*g*l*cos(x(1));
B=Fdrive-cb*x(4)+m*l*x(2)^2*sin(x(1))-kb*x(3)-(M+m)*g;
C=(M+m)*(m*l^2+Ip)-(m*l*cos(x(1)))^2;

xdot=zeros(4,1);

xdot(1)=x(2); % angular velocity of paddle
xdot(2)=((M+m)*A-m*l*cos(x(1))*B)/C; %angular acceleration of paddle
xdot(3)=x(4);   %velocity of M
xdot(4)=((m*l^2+Ip)*B-m*l*cos(x(1))*A)/C; %acceleration of M

end
```

References

Adams, T.M. & Layton, R.A., 2010. *Introductory MEMS: Fabrication and Applications*, Springer.

Agarwal, R., Samson, S., Kedia, S. & Bhansali, S., 2007. Fabrication of Integrated Vertical Mirror Surfaces and Transparent Window for Packaging MEMS Devices. *Journal of Microelectromechanical Systems*, 16(1), pp.122–129.

Agarwal, R., Samson, S. & Bhansali, S., 2007. Fabrication of vertical mirrors using plasma etch and KOH:IPA polishing. *Journal of Micromechanics and Microengineering*, 17(1), pp.26–35.

Andres, M. V, Foulds, K.W.H. & Tudor, M.J., 1986. Optical activation of a silicon vibrating sensor. *Electronics Letters*, 22(21), pp.1097–1099.

Bao, M., 2005. *Analysis and Design Principles of MEMS Devices*, Elsevier.

Bari, G., 2010. Electrodeposition of Nickel. *Modern Electroplating*, pp.79–114.

Barrett, K., Bragg-Sitton, S. & Galicki, D., 2012. Advanced LWR Nuclear Fuel Cladding System Development Trade-off Study.

Basak, N., Harris, G.L., Griffin, J. & Wise, K.D., 2007. Characterisation and application of BPR-100 thick photoresist. *Micro & Nano Letters*, 2(4), pp.115–117.

Becnel, C., 2004. *Ultra Deep SU-8 Manufacturing and Characterization for MEMS Applications*. Louisiana State University.

Bircher, B.A., Duempelmann, L., Renggli, K., Lang, H.P., Gerber, C., Bruns, N. & Braun, T., 2013. Real-time viscosity and mass density sensors requiring

microliter sample volume based on nanomechanical resonators. *Analytical Chemistry*, 85(18), pp.8676–83.

Bogue, R., 2012. Sensors for extreme environments. *Sensor Review*, 32(4), pp.267–272.

Borgermans, P., Labat, S., Brichard, B & Vlockaert, G., 2007. Safety and Operational Monitoring of Nuclear Waste Repositories with Fibre-optic Sensing Systems (SOMOS).

Brand, O., Dufour, I., Heinrich, S. & Josse, F., 2015. *Resonant MEMS: Fundamentals, Implementation, and Application*, John Wiley & Sons.

Carstens, T.A., Corradini, M.L., Blanchard, J.P. & Ma, M., 2012. Thermoelectric Powered Wireless Sensors for Spent Fuel Monitoring. *IEEE Transactions on Nuclear Science*, 59(4), pp.1408–1413.

Carter, E.L., Ward, M. & Anthony, C., 2009. Design and fabrication of novel devices using the Casimir force for non-contact actuation. *IEEE SENSORS 2009 Conference*, pp. 229–233.

Cheung, R., 2006. *Silicon Carbide Microelectromechanical Systems for Harsh Environments*. Imperial College Press.

Chiu, Y., Wu, C., Huang, W. & Wu, J., 2009. Assembly of micro-3-D components on SOI wafers using novel SU-8 locking mechanisms and vertical one-push operation. *IEEE Journal on Selected Topics in Quantum Electronics*, 15(5), pp.1338–1343.

Chu, P.B., Lo, N.R., Berg, E.C. & Pister, K.S.J., 1997. Optical communication link using micromachined corner cube reflector. pp.1–12.

Chu, P.B., 1998. *Optical Communication With Micromachined Corner Cube Reflectors*. UNIVERSITY OF CALIFORNIA Los Angeles.

Cunha, M.P & Lad, R., 2011. Wireless acoustic wave sensors and systems for harsh environment applications. *Wireless Sensors and Sensor Networks*, pp.41–44.

Davies, E., George, D.S. & Holmes, A.S., 2014. Remote photothermal actuation for calibration of in-phase and quadrature readout in a mechanically amplified Fabry-Perot accelerometer. *IEEE Photonics Journal*, 6(3).

Dawit, E., 2010. *Electro-Thermal Mechanical Modeling of Microbolometer for Reliability Analysis*. Canada: University of Waterloo.

Eicke, J., 1999. Distributed microsensing: devices, networks and information processing. *Strategic Assessment Report*.

Elbuken, C., Gui, L., Ren, C.L., Yavuz, M. & Khamesee, M.B., 2008. Design and analysis of a polymeric photo-thermal microactuator. *Sensors and Actuators, A: Physical*, 147(1), pp.292–299.

Elwenspoek, M. & Wiegerink, R., 2001. *Mechanical microsensors*. Springer.

Fatah, R.M.A., 1992. Mechanisms of optical activation of micromechanical resonators. *Sensors and Actuators A: Physical*, 33(3), pp.229–236.

Franssila, S., Kiihamaki, J. & Karttunen, J., 2000. Etching through silicon wafer in inductively coupled plasma. *Microsystem Technologies*, 6(4), pp.141–144.

Gad-el-Hak, M., 2006. *MEMS: Design and fabrication*. Taylor & Francis.

Greenwood, J.C., 1984. Etched silicon vibrating sensor. *Journal of Physics E (Scientific Instruments)*, 17(8), pp.650–652.

Guan, K., 2005. Relationship between photocatalytic activity, hydrophilicity and self-cleaning effect of TiO2/SiO2 films. *Surface and Coatings Technology*, 191(2–3), pp.155–160.

Hahtela, O. & Tittonen, I., 2005. Optical actuation of a macroscopic mechanical oscillator. *Applied Physics B (Lasers and Optics)*, B81(5), pp.589–596.

Hassanin, H. & Jiang, K., 2010. Optimized process for the fabrication of zirconia micro parts. *Microelectronic Engineering*, 87(5–8), pp.1617–1619.

He, G., Zhou, C. & Li, Z., 2011. Review of self-cleaning method for solar cell array. In *Procedia Engineering*. pp. 640–645.

Hedley, J., Burdess, J.S., Harris, A.J. & Gallacher, B.J., 2004. Device characterization at the wafer level via optical actuation and detection. *Technical Proceedings of the 2004 NSTI Nanotechnology Conference and Trade Show*, 1, pp.394–397.

Hong, Y., Liang, T., Jia, P., Liu, W., Tan, Q., Li, C., Zheng, T., Ge, B. & Xiong, J., 2015. Wireless measurement for passive pressure sensors in high temperature environment. *Sensor Review*, 35(2), pp.146–156.

Hong, Y.K., Syms, R., Pister, K.S.J & Zhou, L.X., 2005. Design, fabrication and test of self-assembled optical corner cube reflectors. *Journal of Micromechanics and Microengineering*, 15(3), pp.663–672.

Jaleel, M.A.L. & Abdulnoor, S.S., 2010. Microstructural Characterization of Electroformed Nickel and Its Composites. *Journal of Engineering & Technology*, 28(5), pp.908–917.

Jansen, H., Boer, M.D., Legtenberg, R. & Elwenspoek, M., 1995. The black

silicon method: a universal method for determining the parameter setting of a fluorine-based reactive ion etcher in deep silicon trench etching with profile control. *Journal of Micromechanics and Microengineering*, 5(2), pp.115–120.

Jiang, K., 2010. *Electrochemical Co-deposition of Metal-Nanoparticle Composites for Microsystem Applications*. pp.391–413.

Jiang, K., Lancaster, M.J., Llamas-Garro, I. and Jin, P., 2005. SU-8 Ka-band filter and its microfabrication. *Journal of Micromechanics and Microengineering*, 15(8), pp.1522–1526.

Jiang, L. & Cheung, R., 2009. A review of silicon carbide development in MEMS applications. *International Journal of Computational Materials Science and Surface Engineering*, 2(3/4), p.227.

Jolic, K.I., Ghantasala, M.K. & Harvey, E.C., 2004. Excimer laser machining of corner cube structures. *Journal of Micromechanics and Microengineering*, 14(3), pp.388–397.

Kahn, J.M., Katz, R.H. & Pister, K.S.J., 1999. Next Century Challenges : Mobile Networking for " Smart Dust. *Proceedings of the 5th Annual ACM/IEEE International Conference on Mobile Computing and Networking*, pp.271–278.

Key, M.J., Cindro, V. & Lozano, M., 2004. On the radiation tolerance of SU-8, a new material for gaseous microstructure radiation detector fabrication. *Radiation Physics and Chemistry*, 71(5), pp.1003–1007.

Kiracofe, D., Kobayashi, K., Labuda, Al., Raman, A. & Yamada, H., 2011. High efficiency laser photothermal excitation of microcantilever vibrations in air and liquids. *Review of Scientific Instruments*, 82(1).

Klimchitskaya, G.L., Mohideen, U. & Mostepanenko, V.M., 2009. The Casimir force between real materials: Experiment and theory. *Reviews of Modern Physics*, 81(Compendex), pp.1827–1885.

Klinke, A., Balthazar, J., Felix, J. & Chavarette, F., 2010. the Nonlinear Dynamics of a Vibrating System Modelled By a Inverted Pendulum, With an Electrodynamic Shaker. *Proceedings of the 9th Brazilian Conference on Dynamics Control and their Applications*, pp.1179–1186.

Knobloch, A.J., Ahmad, F.R., Sexton, D.W. & Vernooy, D.W., 2013. Remote Driven and Read MEMS Sensors for Harsh Environments. *Sensors (Basel, Switzerland)*, 13(10), pp.14175–88.

Knudson, A.R., Buchner, S., McDonald, P., Stapor, W.J., Campbell, A.B., Grabowski, K.S., Knies, D.L., Lewis, S. & Zhao, Y 1996. The effects of radiation on MEMS accelerometers. In *1996 IEEE Nuclear and Space Radiation Effects Conference (NSREC 1996), 15-19 July 1996*. USA: IEEE, pp. 3122–3126.

Kroetz, G.H., Eickhoff, M.H. & Moeller, H., 1999. Silicon compatible materials for harsh environment sensors. *Sensors and Actuators A: Physical*, 74(1–3), pp.182–189.

Kruse, P.W. & Skatrud, D.D., 1997. Uncooled Infrared Imaging Arrays and Systems. *Semiconductors and Semimetals, 47.*

Kunimori, H., Otsubo, T., Ishii, T., Suzaki, Y. and Shozu, T., 2012. Design of Engineering Model of Corner Cube Retro-reflector by Evaluating Far Field Diffraction Pattern. *International Conference on Space Optical Systems and*

Applications, 12.

Labuda, A., Cleveland, J. & Geisse, N.A., 2014. Photothermal excitation for improved cantilever drive performance in tapping mode atomic force microscopy. *Microscopy And Analysis*.

Langdon, R., 1985. Resonator sensors-a review. *Journal of Physics E: Scientific Instruments*, 103.

Le, N.C.H., Dao, D.V., Yokokawa, R,. Wells, J.C. & Sugiyama, S., 2009. Fabrication of optically smooth, through-wafer silicon molds for PDMS total internal reflection-based devices. *Microsystem Technologies*, 15(12), pp.1845–1853.

Lee, C.-H., 2008. *Micro Wankel Engine and its Metallic Components Fabrication*. The University of Birmingham.

Lee, C., Jiang, K. & Davies, G., 2007. Sidewall roughness characterization and comparison between silicon and SU-8 microcomponents. *Materials characterization*, 58, pp.603–609.

Lee, D. & Park, J., 2010. Piezo-electrically actuated micro corner cube retroreflector (CCR) for free-space optical communication applications. *Journal of Electrical Engineering & Technology*, 5(2), pp.337–341.

Lee, F.-Y., Zhou, X., Yang, X., Fang, W. & Chen, S., 2015. Design of a tunable resonant micromirror. *Sensors and Actuators A: Physical*, 234, pp.72–81.

Liu, H., Miller, D.W. & Talnagi, J., 2002. Gamma radiation resistant Fabry–Perot fiber optic sensors. *Review of Scientific Instruments*, 73(8), p.3112.

Lobaugh, M., 2014. Using Excel to Implement the Finite Difference Method for 2-

D Heat Trans- fer in a Mechanical Engineering Technology Course Using Excel to Implement the Finite Difference Method for 2-D Heat Transfer in a Mechanical Engineering Technology Course.

MacGeough, J.A., Leu, M.C., Rajurkar, K.P., De Silva, A.K.M. & Liu, Q., 2001. Electroforming process and application to micro/macro manufacturing. *CIRP Annals - Manufacturing Technology*, 50(2), pp.499–514.

Madou, M.J., 1997. *Fundamentals of microfabrication*, Boca Raton: CRC Press.

Mahmoodi, N. & Anthony, C.J., 2014. Air Damping Simulation of MEMS Torsional Paddle. *Proceedings of the 2014 COMSOL Conference*, pp.15–18.

Makowski, D., 2006. *the Impact of Radiation on Electronic Devices With the Special Consideration of Neutron and Gamma Radiation Monitoring*. Technical University of Lodz.

Malik, A. & Singh, P., 2015. Free Space Optics : Current Applications and Future. , 2015(c), p.7.

Marín, E., 2010. Characteristic dimensions for heat transfer. *Latin-American Journal of Physics Education*, 4, pp.56–60.

Miyahira, T.F., Becker, H.N., McClure, S.S., Edmonds, L.D., Johnston, A.H. & Hishinuma, Y., 2003. Total dose degradation of MEMS optical mirrors. *Nuclear Science, IEEE Transactions on*, 50(6), pp.1860–1866.

Munro, S., 2009. *SOI Wafer Notch Reduction using the Low Frequency Pulsing Optionon the STS ICP-RIE*, NanoFab, University of Alberta.

Nieva, P., Kuo, J., Chiang, S. & Syed, A., 2009. A novel MOEMS pressure sensor: Modelling and experimental evaluation. *Sadhana*, 34(August),

pp.615–623.

Perez, M. & Shkel, A., 2005. Conceptual design and preliminary characterization of serial array system of high-resolution MEMS accelerometers with embedded optical detection. *Smart Structures and Systems*, 1(1), pp.63–82.

Petersen, K.E., 1982. Silicon as a mechanical material. *Proceedings of the IEEE*, 70(5), pp.420–457.

Pike, W., 2004. Analysis of sidewall quality in through-wafer deep reactive-ion etching. *Microelectronic Engineering*, 73–74, pp.340–345.

Poeggel, S., Tosi, D., Duraibabu, D., Leen, G., McGrath, D. & Lewis, E., 2015. Optical Fibre Pressure Sensors in Medical Applications. *Sensors*, 15(7), pp.17115–17148.

Powell, A., 2002. Finite Difference Solution of the Heat Equation. 3, pp.1–6.

Qin, L., Shen, D., Wei, T., Tan, Q., Luo, T., Zhou, Z. & Xiong, J., 2015. A Wireless Passive LC Resonant Sensor Based on LTCC under High-Temperature/Pressure Environments. *Sensors*, 15(7), pp.16729–16739.

Rahafrooz, A., Hajjam, A., Tousifar, B. & Pourkamali, S., 2010. Thermal actuation, a suitable mechanism for high frequency electromechanical resonators. *23rd IEEE International Conference on Micro Electro Mechanical Systems,* pp. 200–203.

Salazar, A., 2006. Energy propagation of thermal waves. *European Journal of Physics*, 27(6), pp.1349–1355.

Sampathkumar, A., Murray, T.W. & Ekinci, K.L., 2006. Photothermal operation of high frequency nanoelectromechanical systems. *Applied Physics Letters*,

88(22), pp.2005–2007.

Sehr, H., Tomlin, I.S., Huang, B., Beeby, S.P., Evans, A.G.R., Brunnschweiler, A., Ensell, G.J., Schabmueller, C.G.J. & Niblock, T.E., G2002. Time constant and lateral resonances of thermal vertical bimorph actuators. *Journal of Micromechanics and Microengineering*, 12(4), pp.410–413.

Shea, H.R., 2011. Effects of radiation on MEMS. *Reliability, Packaging, Testing, and Characterization of MEMS/MOEMS and Nanodevices X*.

Shi, Q., Chang, S.C., Putty, M.W. & Hicks, D.B., 1995. Characterization of electroformed nickel microstructures. *Micromachining and Microfabrication Process Technology,* pp. 191–199.

Sum, T.C., Bettiol, A.A., Van Kan, J.A., Watt, F., Pun, E.Y.B. & Tung, K.K., 2003. Proton beam writing of low-loss polymer optical waveguides. *Applied Physics Letters*, 83(9), p.1707.

Thornton, K.E.B., Uttamchandani, D. & Culshaw, B., 1986. Temperature dependence of resonant frequency in optically excited diaphragms. *Electronics Letters*, 22(23), pp.1232–1234.

Usmani, A.S., Rotter, J.M., Lamont, S., Sanad, A.M. & Gillie, M., 2001. Fundamental principles of structural behaviour under thermal effects. *Fire Safety Journal*, 36(8), pp.721–744.

Uttamchandani, D., Thornton, K.E.B., Nixon, J. & Culshaw, B., 1987. Optically excited resonant diaphragm pressure sensor. *Electronics Letters*, 23(4), pp.152–153.

Vasquez, D. & Judy, J., 2007. Optically-interrogated zero-power MEMS

magnetometer. *Journal of Microelectromechanical Systems*, 16(2), pp.336–343.

Venkatesh, S., 1988. Optical microresonator sensor systems. *Journal of the Institution of Electronic and Radio Engineers*, 58(5S), p.S79.

Venkatesh, S. & Novak, S., 1987. Micromechanical resonators in fiber-optic systems. *Optics letters*, 12(2), pp.129–31.

Wang, L., Huang, Q.A., Tang, J. & Luo, J., 2009. Radiation effects on mechanical characteristics of MEMS. In *2009 16th IEEE International Symposium on the Physical and Failure Analysis of Integrated Circuits (IPFA),* pp.764–767.

Wang, W., Xue, X., Huang, Y. & Liu, X., 2014. A Novel Wireless and Temperature-Compensated SAW Vibration Sensor. *Sensors (Basel, Switzerland)*, 14(11), pp.20702–12.

Wang, Y., Jia, Y., Chen, Q. & Wang, Y., 2008. A passive wireless temperature sensor for harsh environment applications. *Sensors*, 8(12), pp.7982–7995.

Warneke, B., Last, M., Liebowitz, B. & Pister, K.S.J., 2001. Smart dust: Communicating with a cubic-millimeter computer. *Computer,* pp. 44-51.

Wasilik, M. & Pisano, A.P., 2001. Low frequency process for silicon on insulator deep reactive ion etching. In *Device and Process Technologies for MEMS and Microelectronics II,* pp.462–472.

Wei, X., Lee, C.H., Jiang, Z. & Jiang, K., 2008. Thick photoresists for electroforming metallic microcomponents. *Proceedings of the Institution of Mechanical Engineers, Part C: Journal of Mechanical Engineering Science*, 222(1), pp.37–42.

Werner, M.R. & Fahrner, W.R., 2001. Review on materials, microsensors, systems and devices for high-temperature and harsh-environment applications. *IEEE Transactions on Industrial Electronics*, 48(2), pp.249–257.

Wijesundara, M.B.J., 2011. *Silicon Carbide Microsystems for Harsh Environments*. Springer.

Williams, J.D., 2004. Study on the postbaking process and the effects on UV lithography of high aspect ratio SU-8 microstructures. *Journal of Micro/Nanolithography, MEMS, and MOEMS*, 3(4), p.563.

Williams, K.R., Gupta, K. & Wasilik, M., 2003. Etch rates for micromachining processing-Part II. *Journal of Microelectromechanical Systems*, 12(6), pp.761–778.

Yang, J., 2013. A harsh environment wireless pressure sensing solution utilizing high temperature electronics. *Sensors (Basel, Switzerland)*, 13(3), pp.2719–2734.

Young-Min, S., Gamzina, D., Barnett, L.R., Yaghmaie, F., Baig, A. & Luhmann, N.C., 2010. UV Lithography and Molding Fabrication of Ultrathick Micrometallic Structures Using a KMPR Photoresist. *Journal of Microelectromechanical Systems*, 19(3), pp.683–689.

Zappe, H., 2010. *Fundamentals of Micro-optics*. Cambridge University Press.

Zheng, R., Sun, W. & Chen, X., 2010. Characterizing and smoothing of striated sidewall morphology on UV-exposed thick SU-8 structures for micromachining millimeter wave circuits. *Journal of Micromechanics and Microengineering*, 20(3).

Zhou, L., Kahn, J. & Pister, K., 2003. Corner-cube retroreflectors based on structure-assisted assembly for free-space optical communication. *Journal of Microelectromechanical Systems*, 12(3), pp.233–242.

Zhou, L.Z.L., Pister, K.S.J. & Kahn, J.M., 2002. Assembled corner-cube retroreflector quadruplet. *Micro Electro Mechanical Systems*, pp.556-559.

Zhu, X., Hsu, V.S. & Kahn, J.M., 2002. Optical modeling of MEMS corner cube retroreflectors with misalignment and nonflatness. *IEEE Journal on Selected Topics in Quantum Electronics*, 8(1), pp.26–32.